PHOTOCATALYTIC REMOVAL OF POLLUTANTS FROM WATER USING GRAPHITIC CARBON NITRIDE-BASED PHOTOCATALYSTS

by

Noman Ahmad

A thesis submitted to the School of Graduate Studies

in partial fulfillment of the requirements for the degree of

Master of Engineering

Faculty of Engineering and Applied Science

Memorial University of Newfoundland

May 2025

St. John's Newfoundland and Labrador Canada

Abstract

This thesis comprises of two main sections. The first part discusses the degradation of nitenpyram using g-C_3N_4 nanosheets and the second part converse the dual functional photocatalysis which involves the simultaneous reduction of Chromium (VI) and oxidation of nitenpyram from water using g-C_3N_4/WO_3 heterojunction. Firstly, the g-C_3N_4 nanosheets were prepared by two step calcination process of melamine in muffled furnace. The characterization results of the prepared nanosheets showed enhanced visible light harvesting ability, narrow band gap and increased surface area compared with the bulk g-C_3N_4 increasing the overall efficiency of the photocatalyst. The nanosheets were utilized as a photocatalyst under visible light to degrade nitenpyram from water. All these experiments were carried out in a batch reactor with a light source for visible light photocatalytic reactions. The results show that it can degrade 99% of the nitenpyram with an initial concentration of 10 ppm at pH 9.0 and catalyst dosage of 1.0 g/L. Further analysis indicates the successful degradation of nitenpyram into its metabolites CPMF, and CPF.

Secondly the nanosheets were combined with metal oxide WO_3 to form a heterojunction which can be used as a dual process for reduction of chromium (VI) and degradation of nitenpyram (NTP). Characterization results show that it has narrower band gap, suitable valance and conduction bands positions, reduced recombination rate of electron-hole pairs which increases its photocatalytic ability for the redox reaction. The experimental outcomes display that it can efficiently reduce chromium (VI) and degrade nitenpyram under visible light. For the dual process at pH 3.0, catalyst dosage of 1.0g/L and initial concentration of 20 ppm the chromium (VI) reduced 88.75% and nitenpyram (NTP) degraded 91.6%. The performance of the heterojunction is compared with the nanosheets and WO_3 which shows a considerable increase in removal of pollutants from environment. The band positions of g-C_3N_4 and WO_3, as determined from UV-

DRS, indicate the formation of a Type II heterojunction between the two semiconductors. This configuration significantly enhances the separation of photogenerated electrons and holes, thereby improving the reduction efficiency of chromium (VI) and the degradation efficiency of nitenpyram (NTP).

Acknowledgements

First and foremost, I would like to show my gratitude to my supervisor Dr. Yan Zhang for her unceasing, support and untiring efforts during my master's degree. Dr. Yan Zhang affectionately ensuing her skills and knowledge to me so that I can progress in my research work and in my future goals.

I would like to express thanks to Memorial University and National Sciences and Engineering Research Council (NSERC) for their financial support towards my research work. I am thankful to CCART and the nanoFAB for their expertise in completing my experimental work.

I am grateful to my parents, wife (Adeera Sajid) and colleagues (Masoumeh Rostami, Yuna Zhang, Abubaker Rutub, Jinesh Machale, and David Hopkins) for their contributions, and academic support towards the completion of my degree.

Finally, my appreciations to all the people who helped me in completing my degree.

Co-authorship statement

A part of the work presented in Chapter 4 of this thesis is derived from a research study which resulted in publication in the Journal of Environmental and Chemical Engineering.

I, Noman Ahmad, co-authored that paper, I was responsible for conducting the investigation of the specific tests needed for the research study.

The article cited in this thesis is titled "N, S co-doped carbon quantum dots/TiO_2 composite for visible-light-driven photocatalytic reduction of Cr (VI)," published in the Journal of Environmental and Chemical Engineering. The original draft and the investigation were conducted by Lantian Chang. The investigation was also conducted by Noman Ahmad. The manuscript was reviewed, edited and supervised by Yan Zhang.

Table of Contents

List of Tables

List of Figures

List of Symbols, and Abbreviations

A	The absorbance measured at excited wavelength
Abs	The absorption spectra
CB	Conduction band
DPC	Diphenyl carbazide
FTIR	Fourier-transform infrared spectroscopy
NTP	Nitenpyram
TEM	Transmission electron microscopy
UV-Vis	Ultraviolet visible spectroscopy
VB	Valance band
XPS	X-ray photoelectron spectroscopy
XRD	X-ray diffraction

Chapter 1. Introduction

1.1 Background

Industrialization and anthropogenic activities have accelerated water pollution by various organic and inorganic contaminants (e.g., dyes, phenolic compounds, pesticides, pharmaceutically active compounds, heavy metal ions, etc.). These pollutants are recalcitrant to degradation and exhibit high toxicity and carcinogenicity, posing a significant threat to the biosystem and human health [1]. Although several techniques including adsorption, electrodialysis, membrane filtration, and electrochemical reduction have been used to remove water pollutants, the re-release of water pollutants (the pollutants removed initially are unintentionally released in the environment) and high energy consumption limit their practical applications. Over the past decades, solar-driven photocatalysis has been intensively applied to convert/decompose toxic water pollutants into less-toxic or non-toxic compounds [2, 3]. Significant progress has been made in developing various solar- or visible-light-active photocatalysts, most of the previous studies have been devoted to either the reductive pathway of heavy metal ions or the oxidative degradation of organic pollutants [4, 5]. The development of an efficient dual-functional photocatalytic reaction system for simultaneous detoxification of a mixture of organic pollutants and heavy metals deserves more research. Compared with single-reaction (either reduction or oxidation) systems that require separate infrastructure for reduction or oxidation, a solar-driven dual-functional photocatalytic process is more efficient and cost-effective in terms of process economics.

Graphitic carbon nitride (g-C_3N_4) is a metal-free conjugated polymer semiconductor constituted mainly by carbon and nitrogen. It is considered a good photocatalyst because of its non-toxicity, high stability, moderate bandgap energy (~2.7 eV), and good visible light harvesting efficiency [6]. Although g-C_3N_4 has been utilized for H_2 production, CO_2 reduction and degradation of

organic pollutants, the obstacles to its commercialization and wider applications are limited by the fast recombination of charge carriers (reduced reaction rate and low efficiency), low surface area, and moderate oxidation ability [6–8]. Photocatalytic performance enhancement of g-C_3N_4 can be accomplished through modifications to its morphology, structure, and surface functionalization. Five commonly used strategies for engineering g-C_3N_4 are elemental doping, copolymerization, morphological control, heterojunction construction, and defect engineering [9,10]. Thermal oxidation etching is a facile morphology control strategy that reduces the number of layering layers, thereby increasing the specific surface area and density of reaction sites in g-C_3N_4 [10]. Nevertheless, additional research is needed to investigate the effects of thermal oxidation etching on the molecular structural change of g-C_3N_4 and the separation of photogenerated charge carriers.

Another strategy for improving the photocatalytic activity of g-C_3N_4 is to integrate with other facile semiconductor photocatalysts to form a heterojunction, which can suppress the recombination of photogenerated charge carriers owing to the opposite migration directions of these carriers within the two semiconductors [11]. So far, various single metal oxides (metal sulfides) have been coupled with g-C_3N_4 for enhanced visible light photocatalysis [12]. Among metal oxide semiconductors (such as TiO_2, ZnO, WO_3, $AgPO_4$, Fe_2O_3, Bi_2O_3, etc.), WO_3 is considered a proper oxidizing semiconductor for heterojunctions because of its visible light response, strong oxidation ability, high photostability and excellent photo-corrosion resistance [13]. Zang et al. synthesized an environmentally benign g-C_3N_4/WO_3 heterojunction via a facile mixing-heating procedure, which showed superb performance in methyl orange degradation [14]. A 2D/2D WO_3/g-C_3N_4 heterojunction was constructed by Pan et al., with anionic polyacrylamide assisted template method [15]. The obtained composite demonstrated marvelous visible-light-activity by degradation of tetracycline [14]. In a most recent study, a direct Z-scheme g-C_3N_4/WO_3

heterojunction fabricated by acid-induced molecule self-assembly method displayed excellent visible-light-responsive activity in degrading several phenolic pollutants [16]. The remarkably enhanced performance of WO_3/g-C_3N_4 heterojunctions was mainly ascribed to the synergistic effects of the enhanced visible light absorption, enlarged specific surface areas and efficient separation of photogenerated charge carriers [17].

Despite the quite significant research studies in using WO_3/g-C_3N_4 heterojunctions for photocatalytic degradation of organic pollutants, not much work has been done on the dual-functional photocatalytic process. Systematic research investigation on the synergetic effect of WO_3/g-C_3N_4 heterojunction for the dual-functional photocatalysis should be carried out. Furthermore, rational design of g-C_3N_4/WO_3 heterojunction to maximize synergistic effects without hindering the desirable intrinsic properties of both materials is challenging because it demands strong interfacial interaction and unique band alignment between the two semiconductors. It is even more difficult to identify and verify the exact charge transfer pathway between them. More research efforts should be devoted to understanding the structure-function relationship of the g-C_3N_4/metal oxide heterojunctions for the enhanced photocatalytic activity and stability of the binary photocatalyst.

1.2 Research Objective

This study examines the performance improvement of g-C_3N_4 as a visible-light responsive photocatalyst via thermal oxidation etching and heterojunction formation for the degradation of nitenpyram, a worldwide utilized pesticide. Utilizing facile thermal oxidation etching, we aim to enhance the surface area and porosity of g-C_3N_4, hence increasing the accessibility of active adsorption and reaction sites for the reactants. We intend to examine the simultaneous photocatalytic reduction of chromium (VI) (Cr (VI)) and oxidation of nitenpyram over the g-

C_3N_4/WO_3 heterojunction under visible light irradiation. This research represents a novel endeavor in the realm of dual-functional photocatalysis for the simultaneous elimination of two hazardous water contaminants.

The research encompasses the subsequent phases: 1) Synthesis of g-C_3N_4 nanosheets through thermal exfoliation of bulk g-C_3N_4; 2) Photocatalytic degradation of NTP from aqueous solutions using g-C_3N_4 nanosheets 3) Construction of g-C_3N_4/WO_3 heterojunction and examination of band alignment between g-C_3N_4 and WO_3; and 4) Simultaneous photocatalytic degradation of NTP and reduction of Cr (VI) utilizing g-C_3N_4/WO_3 heterojunction under visible light irradiation.

1.3 Structure of Thesis

This thesis includes five chapters; Chapter 1 provides an overview of the research topic and research objectives. Chapter 2 comprises a literature review of the related topics. Chapter 3 contains the visible-driven photocatalytic removal of nitenpyram from water using g-C_3N_4 nanosheets. Chapter 4 presents the simultaneous photocatalytic degradation of nitenpyram and reduction of chromium (VI) using g-C_3N_4/WO_3 under visible light irradiation, and Chapter 5 includes major conclusions drawn from the study and recommendations for future work.

References

[1] A. Boretti, L. Rosa, Reassessing the projections of the World Water Development Report, Npj Clean Water 2 (2019) 15. https://doi.org/10.1038/s41545-019-0039-9.

[2] O. Sacco, V. Vaiano, L. Rizzo, D. Sannino, Photocatalytic activity of a visible light active structured photocatalyst developed for municipal wastewater treatment, J. Clean. Prod. 175 (2018) 38–49. https://doi.org/10.1016/j.jclepro.2017.11.088.

[3] Y. Lu, H. Zhang, D. Fan, Z. Chen, X. Yang, Coupling solar-driven photothermal effect into photocatalysis for sustainable water treatment, J. Hazard. Mater. 423 (2022) 127128. https://doi.org/10.1016/j.jhazmat.2021.127128.

[4] L. Chang, N. Ahmad, G. Zeng, A. Ray, Y. Zhang, N, S co-doped carbon quantum dots/TiO_2 composite for visible-light-driven photocatalytic reduction of Cr (VI), J. Environ. Chem. Eng. 10 (2022) 108742. https://doi.org/10.1016/j.jece.2022.108742.

[5] J. Zhu, Z. Liu, H. Wang, Y. Jian, D. Long, S. Pu, Preparation of a Z-Type g-C_3N_4/(A-R)TiO_2 Composite Catalyst and Its Mechanism for Degradation of Gaseous and Liquid Ammonia, Int. J. Mol. Sci. 23 (2022) 13131. https://doi.org/10.3390/ijms232113131.

[6] J. Wang, S. Wang, A critical review on graphitic carbon nitride (g-C_3N_4)-based materials: Preparation, modification and environmental application, Coord. Chem. Rev. 453 (2022) 214338. https://doi.org/10.1016/j.ccr.2021.214338.

[7] A. Naseri, M. Samadi, A. Pourjavadi, A.Z. Moshfegh, S. Ramakrishna, Graphitic carbon nitride (g-C_3N_4)-based photocatalysts for solar hydrogen generation: recent advances and future development directions, J. Mater. Chem. A 5 (2017) 23406–23433. https://doi.org/10.1039/C7TA05131J.

[8] L. Cheng, H. Zhang, X. Li, J. Fan, Q. Xiang, Carbon–Graphitic Carbon Nitride Hybrids for Heterogeneous Photocatalysis, Small 17 (2021) 2005231. https://doi.org/10.1002/smll.202005231.

[9] N. Rono, J.K. Kibet, B.S. Martincigh, V.O. Nyamori, A review of the current status of graphitic carbon nitride, Crit. Rev. Solid State Mater. Sci. 46 (2021) 189–217. https://doi.org/10.1080/10408436.2019.1709414.

[10] D. Li, C. Wen, J. Huang, J. Zhong, P. Chen, H. Liu, Z. Wang, Y. Liu, W. Lv, G. Liu, High-efficiency ultrathin porous phosphorus-doped graphitic carbon nitride nanosheet photocatalyst for energy production and environmental remediation, Appl. Catal. B Environ. 307 (2022) 121099. https://doi.org/10.1016/j.apcatb.2022.121099.

[11] C. Deng, W. Ding, Research progress of toluene oxidation to benzaldehyde and related mesocatalytic systems, Sci. Sin. Chim. 54 (2024) 35–49. https://doi.org/10.1360/SSC-2023-0196.

[12] I.F. Teixeira, E.C.M. Barbosa, S.C.E. Tsang, P.H.C. Camargo, Carbon nitrides and metal nanoparticles: from controlled synthesis to design principles for improved photocatalysis, Chem. Soc. Rev. 47 (2018) 7783–7817. https://doi.org/10.1039/C8CS00479J.

[13] P. Shandilya, S. Sambyal, R. Sharma, P. Mandyal, B. Fang, Properties, optimized morphologies, and advanced strategies for photocatalytic applications of WO_3 based photocatalysts, J. Hazard. Mater. 428 (2022) 128218. https://doi.org/10.1016/j.jhazmat.2022.128218.

[14] Y. Zang, L. Li, Y. Zuo, H. Lin, G. Li, X. Guan, Facile synthesis of composite g-C_3N_4/WO_3: a nontoxic photocatalyst with excellent catalytic activity under visible light, RSC Adv. 3 (2013) 13646. https://doi.org/10.1039/c3ra41982g.

[15] T. Pan, D. Chen, W. Xu, J. Fang, S. Wu, Z. Liu, K. Wu, Z. Fang, Anionic polyacrylamide-assisted construction of thin 2D-2D WO_3/g-C_3N_4 Step-scheme heterojunction for enhanced tetracycline degradation under visible light irradiation, J. Hazard. Mater. 393 (2020) 122366. https://doi.org/10.1016/j.jhazmat.2020.122366.

[16] J. Meng, X. Wang, Y. Liu, M. Ren, X. Zhang, X. Ding, Y. Guo, Y. Yang, Acid-induced molecule self-assembly synthesis of Z-scheme WO_3/g-C_3N_4 heterojunctions for robust photocatalysis against phenolic pollutants, Chem. Eng. J. 403 (2021) 126354. https://doi.org/10.1016/j.cej.2020.126354.

[17] L. Jiang, X. Yuan, G. Zeng, J. Liang, X. Chen, H. Yu, H. Wang, Z. Wu, J. Zhang, T. Xiong, In-situ synthesis of direct solid-state dual Z-scheme WO_3/g-C_3N_4/Bi_2O_3 photocatalyst for the degradation of refractory pollutant, Appl. Catal. B Environ. 227 (2018) 376–385. https://doi.org/10.1016/j.apcatb.2018.01.042.

Chapter 2. Literature Review

Two-dimensional (2D) graphitic carbon nitride (g-C_3N_4) is a unique layered material, characterized as N-substituted graphite composed of π-conjugated graphitic planes formed by sp^2-hybridized carbon (C) and nitrogen (N) atoms [1]. The unique physical structure of 2D g-C_3N_4 nanosheets provides additional possibilities for applications in energy conversion and storage. The following sections will present a concise review of the synthesis of 2D g-C_3N_4 nanosheets and their application as a visible-light-absorbing photocatalyst in wastewater treatment.

2.1 2D g-C_3N_4 Nanosheets

Graphitic carbon nitride (g-C_3N_4) is a novel polymer semiconductor consisting of two primary units, namely, tri-s-triazine (C_6N_7) and s-triazine (C_3N_3) rings, as presented in Figure 2.1 [1, 2]. Tri-s-triazine or triazine rings are connected by C−N bonds, resulting in a layered structure characterized by uniformly distributed triangular nanopores. Typically, g-C_3N_4 prepared through high-temperature solid-state reactions is a bulk phase (3D) material with a low specific surface area (< 10 $m^2\ g^{-1}$) [3]. The exfoliation of bulk g-C_3N_4 can significantly enhance its photocatalytic activity by augmenting the surface area, increasing the number of active reaction sites, and promoting effective charge separation. Therefore, the construction of 2D g-C_3N_4 nanosheets is crucial for heterogeneous photocatalysis.

g-C_3N_4 exhibits electron-rich characteristics, basic moieties, and hydrogen-bonding groups owing to the presence of hydrogen and nitrogen atoms. 2D g-C_3N_4 nanosheets have a band gap of 2.7 eV and can absorb visible light up to 460 nm [4, 5] it is therefore mostly used as heterogeneous photocatalyst in multiple fields such as pollutant degradation [6], hydrogen evolution [7, 8], CO_2 reduction [9,10] and organic transformations.

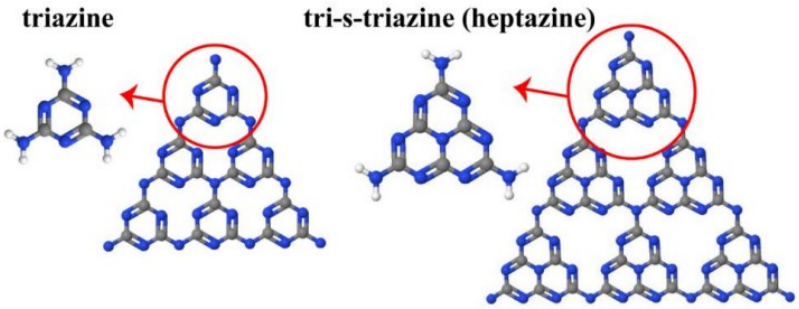

Figure 2.1 Structure of g-C_3N_4 (gray , blue and white atoms balls are carbon, nitrogen and hydrogen respectively) [11]

2.1.1 Synthesis of g-C_3N_4 nanosheets

g-C_3N_4 is commonly synthesized by calcining nitrogen-rich precursors such as urea, thiourea, melamine, cyanamide, and dicyandiamide at temperatures between 450 and 650 °C for 2–4 h. During this process, precursors undergo polyaddition and/or polycondensation to form tri-s-triazine units, which can then be converted into g-C_3N_4 through polycondensation. It has been confirmed that the choice of precursors significantly influences the electronic band structures and textual properties of obtained g-C_3N_4. For example, g-C_3N_4 prepared from thiourea exhibits a slightly narrower bandgap compared with that prepared from urea [12]. On the other hand, g-C_3N_4 prepared from urea presents much higher specific surface area than that prepared from thiourea and melamine. Another parameter that determines the properties of g-C_3N_4 is the reaction temperature. Usually, the polymerization is incomplete at temperature below 450 °C, whereas g-C_3N_4 starts to decompose at temperature above 650 °C. Furthermore, the atmosphere composition (e.g. inert atmosphere, oxidizing atmosphere) used during the thermal polycondensation process can influence the nature of the obtained g-C_3N_4, producing nitrogen vacancies and consequently altering the band gap of g-C_3N_4.

Based on open literature, different morphologies of g-C_3N_4, including nanodots (0D), nanorod (1D), nanotubes (1D), nanosheets (2D), and prisms (3D) can be fabricated through manipulating

synthetic routes. Among them, the 2D g-C_3N_4 nanosheet, made of few atomic layers, exhibits exceptional physical and optical properties, such as high specific surface area, improved photo-response and photo-absorption, thus enhanced photocatalytic activity [13]. This is because the reduced thickness in g-C_3N_4 nanosheets shortens the migration distance of charge carriers from the bulk to the surface-active sites, therefore speeding up the transmission of electrons in the plane. Secondly, the increased specific surface area is advantageous for light harvesting and mass transport, enhances the accessibility of the surface to reactant substrates and electrolytes, and offers a significant number of active sites for ion adsorption and redox reactions. Additionally, due to the quantum confinement effect, the conduction band (CB) position of g-C_3N_4 nanosheets can be shifted to more negative values than that of their bulk compartment, which provides a larger driving force for photocatalytic reaction [14].

2D g-C_3N_4 nanosheets can be produced from bulk (3D) g-C_3N_4 by chemical exfoliation, thermal oxidation etching, and ultrasonication-assisted liquid phase exfoliation [15–17]. In general, exfoliating g-C_3N_4 bulks require overcoming the interlayer van der Waals forces and hydrogen bonding between layers. Chemical exfoliation method typically delaminates bulk g-C_3N_4 through chemical reactions (such as such as redox reactions, intercalation, and ion-exchange) using concentrated acids (e.g., H_2SO_4, HNO_3, or HCL). In this method, concentrated acids molecules penetrated between the layers of g-C_3N_4, and then water molecules and sonication help to weaken the van der Waals interaction and obtain the monolayered nanosheets [18]. A study by Zhang et al. compared the effectiveness of nitric acid and hydrochloric acid for exfoliating g-C_3N_4 [19]. It was observed that both acids are quite efficient and the maximum yield of the nanosheets is up to 40 %. Ma et al. processed the bulk g-C_3N_4 using used HNO_3 to obtain proton-functionalized g-C_3N_4, which was followed by ultrasonication in de-ionized water to produce g-C_3N_4 nanosheets

[19]. The final nanosheets had a much larger surface area of 179 m^2g^{-1} than that of the g-C_3N_4 bulk of 17.4m^2g^{-1}. The increased surface area extended to a marked improvement in photocatalyst activity in hydrogen production and the decolorization of methylene blue. Nonetheless, chemical exfoliation has some drawbacks, such as poor control mechanism, low yield, and involvement of toxic compounds.

Thermal oxidation etching is a facile method which exfoliates bulk-g-C_3N_4 by breaking the interlayer hydrogen bonds through the oxidation reactions with air (O_2) at high temperature [20,21]. Liu et al., first proposed this method in 2012 and they eventually achieved a 2D g- C_3N_4 nanostructure with a thickness of 2 nm [15]. Furthermore, thermal oxidation etching also leads to the attainment of porous structure within bulk g-C_3N_4 due to the release of gaseous products from the oxidative degradation of hydrogen atoms attached to tri-s-triazine or s-triazine moieties. This will greatly increase the internal surface area and pore volume of the obtained nanosheets and hence significantly improve photocatalytic performance. Challagulla et al. [20] utilize the thermal etching to prepare g-C_3N_4 nanosheets for photocatalytic nitrobenzene reduction. The resulting 2D g-C_3N_4 nanosheets had a BET surface area of 216.3 m^2/g, much higher than that of bulk material [20]. Although thermal oxidation etching method is considered the most cost-effective approach as it is easy to scale up and realize the production of g-C_3N_4 nanosheets with the desired properties for photocatalytic applications, the yield of nanosheets of this method is usually quite low [12].

The ultrasonication-assisted liquid exfoliation uses the acoustic energy of the ultrasonic wave to delaminate bulk g-C_3N_4 due to the weak van der Waals forces or hydrogen bonding of g-C_3N_4 layers in solvent [22–24]. During this process, the surface energy of the solvent under the action of the ultrasonic mechanical energy is the crucial factor affecting the exfoliation efficiency. The commonly used solvents with proper surface energy for ultrasonication treatment include water,

acetone, ethanol, 1-isopropanol (IPA), N-methyl-pyrrolidone (NMP), 1,3-butanediol, and dimethyl formamide (DMF). Huang et al. used ultrasonication in a water to exfoliate g-C_3N_4 nanosheets from thermally etched melamine [25]. The BET surface area of g-C_3N_4 nanosheets raised to 26.0 m^2/g from 8.0 m^2/g of bulk g-C_3N_4. In another study, ultrathin g-C_3N_4 nanosheets were prepared from bulk g-C_3N_4 through ultrasonication-assisted exfoliation in mixed solvents of water, ethanol and DMF [26]. The resultant ultrathin g-C_3N_4 had a uniform thickness of 0.38 nm, which was well matched with the theoretical thickness of monolayer g-C_3N_4 (0.33 nm).

Although 2D g-C_3N_4 is a promising metal-free photocatalyst, it suffers from intrinsic limitations and drawbacks related to its structural disorder, such as rapid charge recombination, limited light absorption range, and poor dispersibility in both aqueous and organic mediums. To overcome these shortcomings, various modification approaches have been employed to boost the properties of g-C_3N_4 and expand the range of its application.

2.1.2 Modification to g-C_3N_4 nanosheets

Modification is an effective way to improve the physiochemical properties of 2D g-C_3N_4. Modification of 2D g-C_3N_4 can be implemented through elemental doping, molecular copolymerization and defect engineering, which will be discussed in this section. Whereas the performance enhancement by the formation of heterojunctions with other semiconductors will be introduced in Section 2.2.

2.1.2.1 Elemental doping

Introducing dopants is a standard method to enhance the photoelectronic characteristics of g-C_3N_4, which can enhance the band gap, decrease the interlayer resistance of semiconductors, boost the adsorption of active sites, and increase surface area [27]. Depending on the van der Pauw method,

its layered structure with cavities allows the incorporation of dopants without affecting the compound's ability to absorb visible light.

Carbon-doped g-C_3N_4 has been widely reported for increasing photocatalytic activity by enhancing visible light absorption and lowering the recombination rate of electron/hole pairs. Li et al. [28]prepared the C-g-C_3N_4 by hydrothermal method using glucose and observed that the photocatalytic degradation of methylene blue by C-g-C_3N_4 increased compared to the pure g-C_3N_4. Bao et al. [29]synthesized carbon-doped g-C_3N_4 nanosheets by anionic polyacrylamide as the intercalator via thermal reaction. The prepared catalyst showed a narrower band gap and increased surface area, leading toward 95% degradation of X-3B in 30 minutes under visible light.

In addition, boron-doped g-C_3N_4 can also be prepared using different methods to increase photocatalytic activity. Thaweesak et al. [30]prepared B-doped g-C_3N_4 by calcinating the ammoniotrihydroborate, dicyanamide and NH_4Cl, which indicates an increase in surface area and higher production of H_2. Sulphur doping is another approach to tuning the properties of g-C_3N_4; the sulphur-doped g-C_3N_4 is prepared by pyrolysis of S and N-rich precursors [27]. The prepared photocatalyst shows excellent absorption ability of Pb (II), indicating that S doping can increase the adsorption sites of g-C_3N_4 resulting in increased photocatalytic ability of the S-g-C_3N_4.

Zhu et al. [31] have also used P doping through the thermolysis method to prepare flower-like g-C_3N_4 photocatalysts. It enhances the photocatalytic properties of the substance in the water-splitting process by refining the morphology related to the electronic structure, optoelectronic characteristics and surface area. Phosphorus doping of g-C_3N_4 can yield flower-shaped morphologies (as described in Zhu et al.), which are favourable for enhanced surface area and quantum effects. The production of this morphology gives more reaction sites and minimizes charge recombination, making photocatalytic more active.

The heteroatom doping not only increase the adsorption sites of the reaction substrate but also act as active site to promote the transfer of photogenerated electron/hole pairs and enhance the light absorption of g-C_3N_4. In g-C_3N_4 structure the bridging of N1 cannot transfer the photogenerated carriers, [27] but when doped with heteroatoms it can find a way to transfer the photogenerated carried within the six-fold cavity of g-C_3N_4.

2.1.2.2 Molecular copolymerization

Molecular copolymerization, a strategy of grafting structure-matching small molecules into the tri-*s*-triazine network of g-C_3N_4 during the copolymerization process, is considered a promising pathway to modulate the conventional π frameworks, optical absorption, electronic band structures and photocatalytic performance [32]. This method provides more opportunities for g-C_3N_4 to effectively fill the organic skeleton polymerization loss and extend the π-delocalized system. In the process of high-temperature copolymerization, precursors with similar structures perform molecular self-assembly to constitute a new supramolecular polymer by breaking and reassembling the original hydrogen bonds of g-C_3N_4 [33,34]. Combining melamine and cyanuric acid, Jun et al. constructed 3D macroscopic assemblies of g-C_3N_4 by organic cooperative synthesis [35]. The resulting self-supporting 3D material demonstrated high thermal stability, redshift of absorption edge (up to 700nm), and efficient separation and migration of photogenerated carriers [35]. Wang et al., synthesized a series of 2-aminobenzonitrile-functionalized g-C_3N_4 by copolymerization of different amounts of 2-aminobenzonitrile (ABN) with dicyandiamide. The remarkably improved optical absorption was observed on ABN-functionalized g-C_3N_4, extending the absorption edge from 460 nm to 700 nm [36]. However, the introduction of comonomers sometimes narrows the bandgap and reduces the VB position, bringing unfavorable effects for the

photocatalysts [37]. Further research on the copolymerization modified g-C_3N_4 is anticipated to offer new perspectives on performance enhancement.

2.1.2.3 Introduction of defects

Defect engineering is considered as an effective way to tune the electrical structure and surface morphology of g-C_3N_4 for obtaining the desired physiochemical properties [38,39]. Used as a post-treatment method, vacancies can be introduced in either a reducing or oxidizing atmosphere during the thermal treatment of g-C_3N_4, which lead to the generation of several kinds of defects, including point defects (e.g., vacancies and interstitial defects), line defects (such as dislocations), and bulk defects (e.g. voids). Particularly, vacancy-rich g-C_3N_4 photocatalyst exhibit increased visible light absorption, accelerated reactants adsorption, and enhanced charge separation because of the position, structure, and concentration of vacancy defects [40].

Defect engineering approaches are useful for controlling the band structure of g-C_3N_4. Extremely poor bonding at defect sites reduces the differences between the bonded and anti-bonded orbitals connected by conduction band (CB) and valence band (VB) states, providing extra electronic states in the bandgaps. A decrease of the bandgap was observed from a carbon-vacancy modified g-C_3N_4 due to the optimistically shifted CB position, leading to a formation of a mid-gap below the CB of pristine g-C_3N_4 [41]. Moreover, the introduction of defects into g-C_3N_4 may also accelerate visible light absorption. Yu et al., synthesized nitrogen deficient g-C_3N_4 using alkali-assisted technique [42]. The obtained g-C_3N_4 product with a UV-vis absorption edge of 510 nm demonstrated strong redshift in harnessing visible light compared to original g-C_3N_4 (UV-vis absorption edge of 460 nm). In addition, vacancy defects can considerably prevent the recombination of the photogenerated electron-hole pairs and enhance their utilization efficiency in the surface redox reactions. Research study carried out by Dong et al., revealed that carbon vacancies were able to

capture electrons and suppress the radiative recombination of the photogenerated charges, resulting in much-enhanced separation efficiency of photogenerated electrons and holes, as well as the photocatalytic performance [43]. However, introduction of comonomers sometimes shrink the bandgap and reduce the VB position, bringing unfavorable effects for the photocatalysts.

2.1.3 Applications of g-C_3N_4 nanosheets

Graphitic carbon nitride nanosheets have gained significant consideration because of its distinctive properties, adjustable band gap, environmental sustainability, stability and easy synthetic process. These properties make them a suitable catalyst for a wide range of applications. In environmental remediation it can be used as a visible light active photocatalyst for removal of organic pollutants from the environment, producing H_2, and CO_2 reduction [44]. Additionally, g-C_3N_4 is promising in energy storage and conversion application, such as lithium-ion batteries, fuel cells and supercapacitors, where its surface area and conductivity boost its performance.

2.1.3.1 Photocatalysis

Heterogeneous photocatalysis, a process of accelerating a light-induced reaction in the presence of heterogeneous catalysts (semiconductors), has been considered as one of the most cost-effective methods to produce renewable energy and degradation of various water pollutants. The mechanism of photocatalysis for the removal of pollutants is shown in figure 2.2 where the photocatalyst absorb visible light and generate electron and hole pairs which undergo photocatalytic reaction[45].

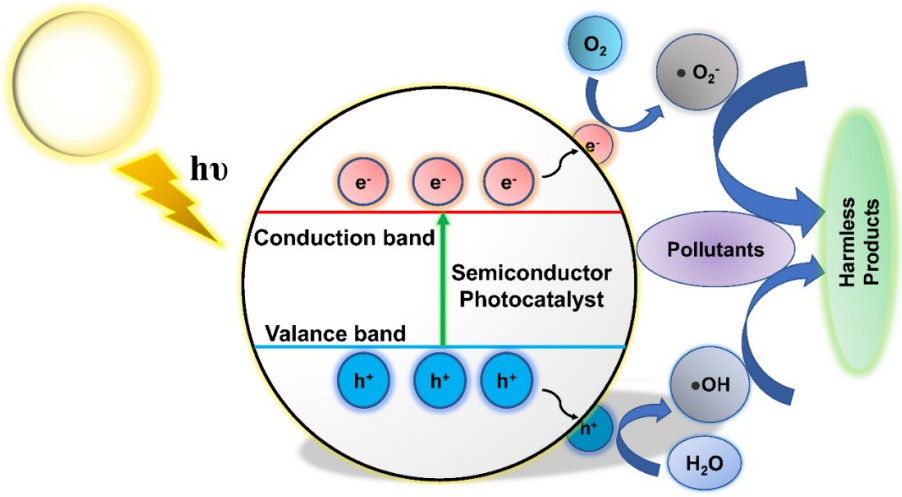

Figure 2.2 Mechanism of Photocatalysis[46]

The properties of the g-C_3N_4 photocatalysts make many environmental applications possible such as photocatalytic removal of pollutants, H_2 production and CO_2 reduction. To illustrate this effectively, Jiang et al. [47] used N-doped g-C_3N_4 nanosheets for tetracycline degradation. The synthesized nanosheets demonstrated enhanced photocatalytic performance and stability compared to the bulk g-C_3N_4, confirming that g-C_3N_4-based materials have a broad application prospect in environmental treatment.

Photocatalytic water splitting is a process that converts solar energy into carbon-neutral green H_2 by splitting H_2O into H_2 and O_2 on a semiconductor photocatalyst. The bandgap of the photocatalyst should exceed the water splitting energy which is 1.23 eV. The CB minimum should be more negative than the reduction potential H^+/H_2 and VB should be more positive than the oxidation potential O_2/H_2O. The bandgap of g-C_3N_4 is 2.7 eV which not only meet the energy requirement but also can absorb visible light, g-C_3N_4 nanosheets shows steady H_2 production under visible light when kept in Pt deposition[48]. Qu et al. [49]compared the performance of bulk and

monolayered g-C_3N_4, and found out that monolayered has more negative CB position which results in more H_2 production.

Photocatalytic CO_2 reduction is the process of converting CO_2 into other fuel utilizing solar energy, CO_2 activation is the rate determining step due to its higher potential. Initially TiO_2 was used as a photocatalyst for CO_2 reduction but due to its limitations in visible region, g-C_3N_4 is more suitable in this case. Niu et al. [50] effectively fabricated two different g-C_3N_4 photocatalysts, bulk g-C_3N_4 and g-C_3N_4 nanosheets, with bandgaps of 2.77 eV and of 2.97 eV, respectively. Under UV–vis light, the g-C_3N_4 nanosheets displayed a high selectivity to the generation of CH_4 whereas the bulk g-C_3N_4 favoured to yield CH_3CHO.

In conclusion, the g-C_3N_4 nanosheets have bright photocatalytic potential due to their large surface area. However, researchers are still studying other safer and more effective photocatalytic materials for environmental purification.

2.1.3.2 Energy Storage

g-C_3N_4's favourable structure has sparked interest in its application within energy storage systems, because of the macrospores which serves as adsorption sites for alkali metals. g-C_3N_4 shows great potential in the electrochemical storage i.e. lithium-ion batteries (LIBs), sodium ion batteries (SIBs), lithium sulfur batteries (LSBs) and supercapacitors[51].

In 2013 Wu and Coworkers [52] proved that g-C_3N_4 has a great potential for LIBs through the DFT calculation. Jorge et al. showed the electrochemical performance of g-C_3N_4 on LIBs [53] and it can be observed by the cyclic volumetric that it shows oxidation and reduction peaks between 0.5-1.5 V, but its capacity decreases from 14 to 6-8 mA h g^{-1} after one cycle. This indicates that g-C_3N_4 can be used for electrochemistry, but its performance depends on conductivity, surface area, N content crystallinity and other factors.

The impact of more than two Li^+ adsorbed in bulk and monolayered g-C_3N_4 was thoroughly studied by Hankel and colleagues [54] in 2015. According to the DFT calculations, Li^+ primarily interacts with the pyridinic-N and adsorbs preferentially over the triangular pores with a high adsorption energy. The graphitic-N (C_3N) bonds are weakened and break first as a result of Li's$^+$ preference for the pyridinic-N. The primary cause of g-C_3N_4's high irreversible capacity is the structural instability caused by the bonds breaking in graphitic-N. Consequently, one efficient method of enhancing lithium storage performance is to decrease the amount of graphite-N to increase the structural stability of g-C_3N_4. Motivated by this, Chen and colleagues [55] used pristine g-C_3N_4 as the precursor to create N-deficient g-C_3N_4 (ND-g-C_3N_4) via a magnesiothermic denitriding technique. The quantitative examination of XPS spectra following the magnesiothermic denitriding reaction revealed that, particularly for graphite-N, the N content of ND-g-C_3N_4 decreased significantly to 8.84 at% from the original N content of g-C_3N_4 (51.4 at%). Furthermore, the conductivity of ND-g-C_3N_4 was enhanced by the transformation of graphitized carbon and the decrease of N content. ND-g-C_3N_4 demonstrated good lithium storage performance, including low irreversible capacity and steady cycle stability, thanks to a drop-in graphite-N concentration and an increase in conductivity. When used as an anode material in LIB, the ND-g-C_3N_4 delivered a high reversible lithium storage capacity of 2753 mA h g^{-1} after 300th cycle, which was 200 times than the pristine g-C_3N_4.

There have been several attempts to use g-C_3N_4 to sodium-ion batteries (SIBs) due to its exceptional performance in LIBs. Although SIBs and LIBs operate on the same principle, the bigger size of the sodium ions in SIBs causes a longer electrochemical response process.

Liu et al. [56]obtained the g-C_3N_4 precursor with zinc catalysis at various temperatures to produce g-C_3N_4 with varying layer spacing to increase the reactive power in SIBs. The g-C_3N_4 produced at

800°C is made up of three layers spaced 0.51 nm apart, the g-C_3N_4 produced at 800 °C has the best sodium storage performance and the widest layer gap when compared to the g-C_3N_4 annealed at 700 and 900°C. It demonstrated exceptional long-term stability, ultra-high-rate capability (56.6 mA h g^{-1} at 40 A g^{-1}), and Na^+ storage performance when utilized as a SIB anode. This is due to the fact that the p-orbital lone pair pyrrolic-N is highly active in absorbing Na^+, and that varying annealing temperatures alter the amount of pyrrole-N in CN. Unlike pyridinic-N, which possesses a single pair of electrons, Pyrrolic-N with lone electron pairs perpendicular to the graphene plane can increase the interlayer parallel to the graphene layer. The cycling life of MIBs can be prolonged by employing 2D materials with fewer layers and larger interlayer spacing, which can effectively counteract the structural stability damage brought on by the insertion/extraction of metal ions between the layers[51-56]. Although 2D g-C_3N_4 nanosheets are easy and affordable to create, they are far less conductive than graphene. Most significantly, the g-C_3N_4 with lower N content has better electrical conductivity, which surely opens up more possibilities for g-C_3N_4's use in electrochemistry.

2.2 g-C_3N_4/metal oxide heterojunctions

The construction of heterojunctions is another feasible approach to improve properties of g-C_3N_4 nanosheets [57]. Especially, the charge separation efficiencies can be greatly improved owing to the tunable band structure at the interface. Combination of g-C_3N_4 (a reductive semiconductor) with widely abundant metal oxides (MO) with strong oxidative potential facilitates the resulting heterojunctions with both high oxidative and reductive potentials. Most commonly, either a Type II or a direct Z-scheme heterojunction can be formed based on the band positions of g-C_3N_4 and the selected metal oxide. As illustrated in Fig. 2.3a, a Type II heterojunction requires two coupled semiconductors with staggered energy-band configurations. Once exposed to visible light,

photogenerated electrons move from CB of semiconductor I (g-C_3N_4) to CB of semiconductor II (metal oxide) and holes transfer in the opposite direction. The migration of charge carriers in the opposite direction significantly enhances the electron−hole spatial separation and retards the charge recombination to prolong the lifetime of free electrons and holes [58]. Nonetheless, the migration of the photogenerated electrons to the less negative CB and holes to the less positive VB reduces the redox abilities of electrons and holes in type II heterojunction [59,60]. Construction of direct Z-scheme heterojunctions can help to overcome this shortcoming. The direct Z-scheme heterojunction (Fig. 2.3b) has the same band alignment as that of type II heterojunction but differs in the charge transfer mechanism. Due to different CB and VB edges between SC I and SC II, photo-induced electrons in a Z-scheme heterojunction are transferred from the CB of SC II to the VB of SC I, which results in oxidation on the surface with higher oxidation potential (SC II surface) and reduction on the surface with higher reduction potential (SC I surface) [60]. Furthermore, the charge migration in direct Z-scheme heterojunctions is based on the electrostatic attraction between electrons and holes, which is easier than that of type II heterojunction [59]. Therefore, combining g-C_3N_4 with metal oxides such as TiO_2, ZnO, and WO_3 through these heterojunction mechanisms can greatly improve the photocatalytic efficiency for various environmental, and energy applications.

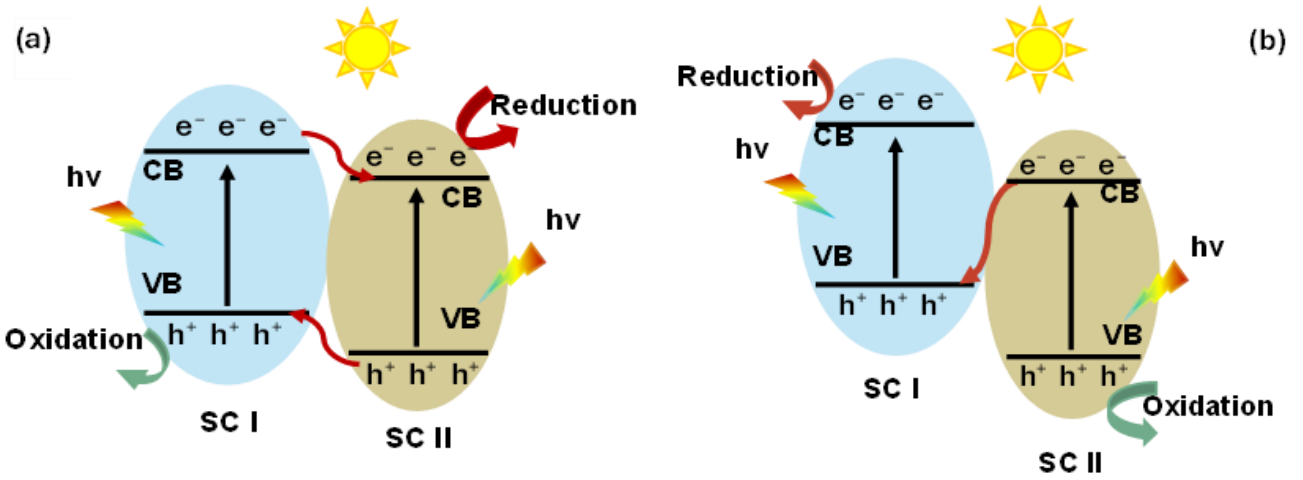

Figure 2.3 Band structure of (a) Type II and (b) direct Z-scheme heterojunction between g-C_3N_4 and metal oxide[61]

2.2.1 Fabrication of g-C_3N_4/metal oxide heterojunctions

The preparation of g-C_3N_4/metal oxide (g-C_3N_4/MO) heterojunctions and the control of their microstructures are crucial for modulating their physicochemical and optical properties, and thus photocatalytic performance. The most used synthetic methods for g-C_3N_4/MO heterojunctions include co-calcination, hydrothermal/solvothermal synthesis, and microwave-assisted method [62].

The hydrothermal/solvothermal synthesis is a method of preparing nanoparticles from high-temperature aqueous solutions or organic solvents in high-pressure autoclaves. Hydrothermal/solvothermal method has been widely applied because of its advantages of simplicity, high reactivity, ease of control, and low cost. Kocí et al. synthesized g-C_3N_4/TiO_2 heterojunction for the photocatalytic decomposition of N_2O via hydrothermal and calcination methods [63]. The g-C_3N_4/TiO_2 heterojunction was fabricated by calcining mixers of TiO_2, prepared by thermal hydrolysis, and g-C_3N_4, derived from commercial melamine, at 450°C for 1 h. The photocatalytic efficiency of the synthesized catalyst is significantly enhanced in comparison to pristine TiO_2 and g-C_3N_4. Kumar et al. prepared a 2D/2D g-C_3N_4/N-ZnO heterojunction through

hydrothermal method. In this study, N-doped ZnO (N-ZnO) was mixed with g-C_3N_4 in water for 48 h, followed by evaporation of water, and a powder composite of g-C_3N_4/N-ZnO nanoplates was prepared after drying at 100 °C for 1h. In another study, solvothermal synthesis of ZnO/g-C_3N_4 hybrid materials has been achieved by dissolving Zinc nitrate in ethanol and then adding prepared g-C_3N_4, and the mixture was heated under a Teflon-lined autoclave at 180°C for 12 hours. This process leads to a proper dispersion of ZnO on the g-C_3N_4, which contributes to the photocatalytic degradation of the organic contaminants.

One-pot calcination (or co-calcination) has also been employed to synthesize various g-C_3N_4/MO heterojunctions. Zhu et al. prepared g-C_3N_4/ZnO through one-pot calcination of mixtures of evaporation-dried dicyandiamide and $Zn(NO_3)_2$. The resulting heterojunction exhibited a notable red shift in the absorption of longer wavelength visible light [64]. Another study reported the fabrication of exfoliated g-C_3N_4/MoO_2 heterojunctions via one-step calcination of bulk g-C_3N_4 and $(NH_4)_2MO_4$ powders at 500°C for 2 hours [65]. The g-C_3N_4/MoO_2 composite exhibited a specific surface area of 96.17 $m^2\ g^{-1}$ and a H_2 evolution rate of 320.8 $\mu mol\ g^{-1}\ h^{-1}$ under visible light, representing a 4.1-fold increase compared to bulk g-C_3N_4. By co-calcination of urea and TiO_2 precursors, the g-C_3N_4/TiO_2 heterojunction with high dispersion and good particle size distribution was obtained[66]. The UV–Vis diffuse reflectance spectra, photoluminescence spectra, and photochemical tests indicated that g-C_3N_4/TiO_2 exhibited significant visible light absorption and efficient transfer of photo-generated carriers, resulting in enhanced photocatalytic activity under sunlight irradiation.

Microwave-assisted synthesis is a promising method for the preparation of nanomaterials with the advantages of fast reaction rate, high reaction selectivity and low energy consumption. Microwave generates direct volumetric heating, and heat is simultaneously produced in the whole system,

which results in fast and selective heating [67]. In recent years, microwave irradiation (MWI) technique has been utilized for the synthesis of various types of carbon materials, metal oxides and metal hydroxides. An in-situ microwave-assisted synthesis approach has been developed by Wang et al. to prepare N-TiO_2/g-C_3N_4 heterojunctions using H_2TiO_3 as the reactant and $NH_3 \cdot H_2O$ as the N-doping source [68]. More specifically, peroxotitanate solution was mixed with the g-C_3N_4 suspension under constant agitation for 3h, the mixer was then exposed to microwave irradiation for 1 h and calcinated at 300−500 °C in a muffle furnace for 2 h. The resulting N-TiO_2/g-C_3N_4 heterojunctions had a porous structure and large surface areas and exhibited significantly improved photocatalytic activity. Highly porous heterojunction of g-C_3N_4 and SnO_2 was prepared by through pyrolysis of urea in tin chloride solution under MWI for 30 minutes [69]. By continuous removing the gaseous products from the synthetic environment, a porous heterojunction with high specific surface area and efficient photogenerated charge separation was obtained. Recently, Vijayakumar and Vadivel constructed a g-C_3N_4/WO_3 heterojunction through one-step MWI technique followed by direct calcination of a combination of WO_3 and g-C_3N_4 at 400 °C for 4 h [46]. A much higher BET surface area (138.0 m^2 g^{-1}) was achieved by the g-C_3N_4/WO_3 heterojunction compared to pure WO_3 nanoparticle (98.0 m^2 g^{-1}).

2.2.2 Applications of g-C_3N_4/metal oxide heterojunctions

Heterojunctions of g-C_3N_4/MO, owing to their appealing optical and physicochemical properties, have been widely utilized as functional materials to address various issues in energy conversion and environmental remediation. g-C_3N_4/MO heterojunctions serve as photocatalysts for hydrogen production through water splitting, CO_2 reduction (or CO_2 hydrogenation), pollutant degradation, and organic compound transformation. g-C_3N_4/MO heterojunctions have been utilized as

supercapacitors in multifunctional devices[70]. The utilization of g-C_3N_4/MO heterojunctions as gas sensors for the detection of toxic or volatile gases is extensively documented [11].

2.2.2.1 Photocatalysis

Hydrogen production has been proposed as a feasible solution to address the significant global energy demands. The solar-driven photocatalytic splitting of water appears a promising technique for producing H_2 in a clean and environmentally sustainable way [71]. Photocatalytic water splitting is a process that converts solar energy into carbon-neutral green H_2 by splitting H_2O into H_2 and O_2 on a semiconductor photocatalyst. For successful photocatalytic water splitting, the CB position of a semiconductor must be below 0 V relative to the normal hydrogen electrode (NHE), and the VB edge must exceed 1.23 V relative to NHE [70]. The band structures of g-C_3N_4/MO heterojunctions fulfill this criterion. Furthermore, the enhanced efficiency of visible-light absorption and charge carrier separation allows g-C_3N_4/MO heterojunctions to achieve a substantially higher H_2 generation rate compared to pristine g-C_3N_4 and/or metal oxides. Rahman et al. constructed a g-C_3N_4/TiO_2 heterojunction with in-situ growth of ultrathin g-C_3N_4 nanosheets (~ 2nm in thickness) on the TiO_2 core. The resulting g-C_3N_4/TiO_2 core-shell heterojunction showed improved H_2 generation performance from 35.43 to 45.25 mol h^{-1} owing to the enhanced charge carrier separation [71]. Fu et al. fabricated an ultrathin 2D/2D g-C_3N_4/WO_3 heterojunction by self-assembly of WO_3 layers and g-C_3N_4 nanosheets [103]. The H_2 production rate was greatly enhanced by the g-C_3N_4/WO_3 heterojunction, which is 1.7 folds higher than that by pure g-C_3N_4 [72]. A SnO_2/g-C_3N_4 heterojunction photocatalyst was prepared via the self-assembly method for the H_2 production from water splitting [73]. An exceptionally high H_2 generation rate (2090 μmol h^{-1} g^{-1}) was achieved by SnO_2/g-C_3N_4 due to the bulk electron mobility of SnO_2 and excellent separation of photogenerated electrons and holes in SnO_2/g-C_3N_4[73].

Considerable efforts have been devoted to photochemical conversion of CO_2, the most important green house gas, into value-added alcohols and fuels (e.g., CO, CH_4, CH_3OH, and HCOOH) using visible-light-responsive g-C_3N_4/MO heterojunctions. Photocatalytic CO_2 reduction typically necessitates elevated energy levels to cleave the C-O bond and facilitate the formation of new C-H bonds . A Z-scheme g-C_3N_4/Ag_3PO_4 heterojunction was prepared for the CO_2 reduction at 80 °C. The photogenerated electrons in the CB of g-C_3N_4 participate in reduction reactions, while the holes in the VB of Ag_3PO_4 are involved in oxidation reactions. The optimized g-C_3N_4/Ag_3PO_4 achieved a CO_2 conversion rate of 57.5 μmol h^{-1}, corresponding to 6.1- and 10.4-fold increases compared to g-C_3N_4 and Ag_3PO_4, respectively[74]. He et al. developed a 2D/2D g-C_3N_4/ZnO heterojunction using a facile impregnation method[75]. A type II heterojunction was established between g-C_3N_4 and ZnO, demonstrating superior photocatalytic CO_2 reduction activity, 4.9 and 6.4 times greater than that of pristine g-C3N4 and ZnO, respectively. The boost in performance was ascribed to improved CO_2 adsorption and the effective separation of photogenerated charge carriers. Visible-light-driven CO_2 photoreduction was carried out on a Z-scheme heterojunction of N-doped TiO_2 and g-C_3N_4, with CO to be the main carbonaceous products. The quantity of CO generated after 12 h was observed to be 3.2 times greater than pure g-C_3N_4 under UV-vis irradiation [76]. Using the in-situ colloidal crystal template method, a direct Z-scheme heterojunction of g-C3N4 nanosheets adorned macroporous WO_3 were constructed by Moutigaud et al. for CO_2 reduction [77]. Owing to the improved separation efficiency of photogenerated electron-hole pairs, the resultant heterojunction exhibited good catalytic activity for CO_2 reduction, with a CO production rate of 48.7 mol $g^{-1}h^{-1}$. Despite significant advancements in the photocatalytic reduction of CO_2 via g-C_3N_4/MO heterojunctions, enhancing reaction selectivity remains to be a challenge.

Semiconductor-based photocatalysis using solar energy has attracted increasing attention as a sustainable technology for catalytic degradation of water pollutants and environmental remediation. Over the past decade, g-C_3N_4/MO heterojunctions have been extensively applied to decompose diverse water contaminants due to their superior oxidation ability and tunable electronic properties. Muñoz-Batista et al. developed g-C_3N_4/TiO_2 heterojunction by impregnation method, resulting in a significant improvement in the photodegradation of toluene under UV and sunlight exposure[78]. Shen et al. demonstrated that a mesoporous g-C_3N_4/TiO_2 heterojunction, synthesized through protonation and in-situ deposition of TiO_2 onto g-C_3N_4, significantly enhanced the degradation efficiency of methyl orange (MO) under visible light irradiation[79]. A Z-scheme g-C_3N_4/ZnO heterojunction was prepared by Vignesh et al. by a sonication-assisted solvent impregnation method [80]. The obtained heterojunction showed excellent performance in photocatalytic degradation of rhodamine B (RhB), capable of completely degrading Rh B (10 mg L^{-1}) within 60 min under the simulated solar light irradiation. Magnetically separable g-C_3N_4/Fe_3O_4 heterojunctions were fabricated by an in-situ growth method of Fe_3O_4 nanoparticles on g-C_3N_4 nanosheets[81]. The heterojunction containing 84.8% of g-C_3N_4 exhibited the highest photocatalytic activity for RhB, being seven times greater than that of pristine g-C_3N_4.

In addition to the commonly used metal oxide semiconductors (such as TiO_2, ZnO, Fe_3O_4, etc.), combination of g-C_3N_4 with other metal oxides such as Bi_2O_3, CeO_2, MoO_3, and WO_3 has also been widely reported. Using the impregnation technique, Shafawi et al. fabricated a novel Bi_2O_3/porous g-C_3N_4 heterojunction for the photodegradation of reactive black 5[82]. The best-performance Bi_2O_3/g-C_3N_4 heterojunctions achieved a degradation of up to 84% of reactive black 5 (10 mg L-1) at pH 5.7 after 120 minutes of UV-vis light exposure, exhibiting degradation rates 1.87 and 1.75 times superior to porous g-C_3N_4 and Bi_2O_3, respectively. Ma et al. prepared a Type

II g-C_3N_4/CeO_2 heterojunction through hydrothermal method for degradation of bisphenol A (BPA) under visible-light irradiation [47]. The best-performance g-C_3N_4/CeO_2 heterojunction dissolved 93.7% of BPA after 80 minutes of visible light irradiation, significantly surpassing the decomposition rates of g-C_3N_4 (65.0%) and CeO_2 (14.4%). A separate study synthesized a series of g-C_3N_4/CeO_2 heterojunctions with varying mass fractions of CeO_2 for the reduction of Cr (VI) and the degradation of 2-chlorophenol (2-CP) from wastewater [48]. The 15% CeO_2 integrated g-g-C_3N_4 heterojunction exhibited exceptional photocatalytic performance due to effective photogenerated charge separation, obtaining a reduction efficiency of 96% for Cr (VI) and a removal efficiency of 93% for 2-CP under visible light irradiation. A g-C_3N_4/MoO_3 heterojunction was prepared with a simple mixing-calcination method for the photodegradation of methylene blue (MB) under visible light [83]. The heterojunction with a g-C_3N_4 mass fraction of 7% had the optimal photocatalytic activity, capable of degrading 93.0% of MB (10 mgL^{-1}) after 3 h visible light irradiation, much higher than that of MoO_3 (43.0%) and g-C_3N_4 (52.0%). A Z-scheme heterojunction comprising g-C_3N_4 and WO_3 was constructed and utilized as a visible-light-responsive photocatalyst for the degradation of sulfamethoxazole (SMX), a widely used antibiotic [84]. Due to enhanced separation of photogenerated electron-hole pairs and redox capacity, the g-C_3N_4/WO_3 heterojunction achieved a degradation of 91.7% of SMX (10 mg L^{-1}) with a catalyst dosage of 1.0 g L^{-1}, which was 2.2 and 2.0 times more than that of WO_3 and g-C_3N_4, respectively.

2.2.2.2 Sensing

The integration of g-C_3N_4 nanosheets with various MOs has facilitated the development of advanced chemiresistive sensors for the detection of hazardous and flammable gases [85]. The fundamental working mechanism of chemiresistive sensors relies on the adsorption and desorption of target gas molecules on the sensor's surface, leading to alterations in the sensor's resistance.

Chemiresistive sensors typically utilize a two-electrode system in which the resistance of the sensing layer within the electrodes is monitored over time during gas exposure[86]. The sensing materials for chemiresistive sensors comprise conducting polymers, carbon nanomaterials, and semiconducting metal oxides. The combination of g-C_3N_4 with MO significantly enhances the sensing selectivity and sensitivity of both g-C_3N_4 and Mos [86]. To date, g-C_3N_4/MO composites have been employed for the detection of poisonous gases, volatile organic compounds (VOCs), and flammable gases, owing to their rapid response and recovery times, good sensing selectivity, and low cost [55]. Cao et al. reported a facile calcination method for the synthesis of g-C_3N_4/SnO_2 sensors[87]. The response value and selectivity of the g-C_3N_4/SnO_2 composite sensor to ethanol surpass those of pristine SnO_2 nanoparticles. A g-C_3N_4/ZnO heterojunction was synthesized using the precipitation calcination process, in which g-C_3N_4nanosheets were affixed to the petals of a ZnO flower-like structure [88]. The composite with 3wt% of g-C_3N_4 demonstrated a significantly enhanced sensing response, expedited response/recovery time, and superior long-term stability relative to the pure ZnO sensor when exposed to 1000 ppm CH4 at 320 °C. The enhanced sensing response resulted from the presence of a porous structure, an extensive surface area, and efficient charge transfer at the g-C_3N_4/ZnO interface [88]. In a separate investigation, Zeng et al. employed α-Fe_2O_3/g-C_3N_4 for the detection of H_2S. Their findings indicated that the heterojunction containing 5.97% α-Fe_2O_3 in g-C_3N_4 exhibited the optimal cataluminescence response[89]. Recently, Akhtar et al. synthesized g-C_3N_4/CuO nanocomposites (with different weight ratios of g-C_3N_4 to CuO) by a hydrothermal method for the detection of diverse VOCs [90]. The composite with 4 w% of g-C_3N_4 exhibited the highest sensing response (143.7 to 1000 ppm for acetone) and selectivity (about 14.37 for 1000 ppm acetone/1000 ppm ammonia). Their findings indicated that

the decorating of CuO nanoparticles on g-C_3N_4 nanosheets augmented the specific surface area of the nanocomposite, hence enhancing the sensing response.

References

[1] A. Mishra, A. Mehta, S. Basu, N.P. Shetti, K.R. Reddy, T.M. Aminabhavi, Graphitic carbon nitride (g–C3N4)–based metal-free photocatalysts for water splitting: A review, Carbon 149 (2019) 693–721. https://doi.org/10.1016/j.carbon.2019.04.104.

[2] P. Suyana, P. Ganguly, B.N. Nair, S.C. Pillai, U.S. Hareesh, Structural and compositional tuning in g-C3N4 based systems for photocatalytic antibiotic degradation, Chem. Eng. J. Adv. 8 (2021) 100148. https://doi.org/10.1016/j.ceja.2021.100148.

[3] J. Wen, J. Xie, X. Chen, X. Li, A review on g-C_3N_4 -based photocatalysts, Appl. Surf. Sci. 391 (2017) 72–123. https://doi.org/10.1016/j.apsusc.2016.07.030.

[4] Y. Wang, L. Liu, T. Ma, Y. Zhang, H. Huang, 2D Graphitic Carbon Nitride for Energy Conversion and Storage, Adv. Funct. Mater. 31 (2021) 2102540. https://doi.org/10.1002/adfm.202102540.

[5] M. Ismael, A review on graphitic carbon nitride (g-C_3N_4) based nanocomposites: Synthesis, categories, and their application in photocatalysis, J. Alloys Compd. 846 (2020) 156446. https://doi.org/10.1016/j.jallcom.2020.156446.

[6] C. Zhang, W. Lv, G. Zhou, Z. Huang, Y. Zhang, R. Lyu, H. Wu, Q. Yun, F. Kang, Q. Yang, Vertically Aligned Lithiophilic CuO Nanosheets on a Cu Collector to Stabilize Lithium Deposition for Lithium Metal Batteries, Adv. Energy Mater. 8 (2018) 1703404. https://doi.org/10.1002/aenm.201703404.

[7] J. Liu, Y. Liu, N. Liu, Y. Han, X. Zhang, H. Huang, Y. Lifshitz, S.-T. Lee, J. Zhong, Z. Kang, Metal-free efficient photocatalyst for stable visible water splitting via a two-electron pathway, Science 347 (2015) 970–974. https://doi.org/10.1126/science.aaa3145.

[8] D.J. Martin, K. Qiu, S.A. Shevlin, A.D. Handoko, X. Chen, Z. Guo, J. Tang, Highly Efficient Photocatalytic H_2 Evolution from Water using Visible Light and Structure-Controlled Graphitic Carbon Nitride, Angew. Chem. Int. Ed. 53 (2014) 9240–9245. https://doi.org/10.1002/anie.201403375.

[9] G. Zhang, M. Liu, T. Heil, S. Zafeiratos, A. Savateev, M. Antonietti, X. Wang, Electron Deficient Monomers that Optimize Nucleation and Enhance the Photocatalytic Redox

Activity of Carbon Nitrides, Angew. Chem. Int. Ed. 58 (2019) 14950–14954. https://doi.org/10.1002/anie.201908322.

[10] L. Shi, T. Wang, H. Zhang, K. Chang, J. Ye, Electrostatic Self-Assembly of Nanosized Carbon Nitride Nanosheet onto a Zirconium Metal–Organic Framework for Enhanced Photocatalytic CO_2 Reduction, Adv. Funct. Mater. 25 (2015) 5360–5367. https://doi.org/10.1002/adfm.201502253.

[11] A. Alaghmandfard, K. Ghandi, A Comprehensive Review of Graphitic Carbon Nitride (g-C_3N_4)–Metal Oxide-Based Nanocomposites: Potential for Photocatalysis and Sensing, Nanomaterials 12 (2022) 294. https://doi.org/10.3390/nano12020294.

[12] Z. Mao, J. Chen, Y. Yang, D. Wang, L. Bie, B.D. Fahlman, Novel g-C_3N_4/CoO Nanocomposites with Significantly Enhanced Visible-Light Photocatalytic Activity for H_2 Evolution, ACS Appl. Mater. Interfaces 9 (2017) 12427–12435. https://doi.org/10.1021/acsami.7b00370.

[13] M. Majdoub, Z. Anfar, A. Amedlous, Emerging Chemical Functionalization of g-C_3N_4 : Covalent/Noncovalent Modifications and Applications, ACS Nano 14 (2020) 12390–12469. https://doi.org/10.1021/acsnano.0c06116.

[14] S. Yin, J. Han, T. Zhou, R. Xu, Recent progress in g-C_3N_4 based low cost photocatalytic system: activity enhancement and emerging applications, Catal. Sci. Technol. 5 (2015) 5048–5061. https://doi.org/10.1039/C5CY00938C.

[15] P. Niu, L. Zhang, G. Liu, H. Cheng, Graphene-Like Carbon Nitride Nanosheets for Improved Photocatalytic Activities, Adv. Funct. Mater. 22 (2012) 4763–4770. https://doi.org/10.1002/adfm.201200922.

[16] H. Xu, J. Yan, X. She, L. Xu, J. Xia, Y. Xu, Y. Song, L. Huang, H. Li, Graphene-analogue carbon nitride: novel exfoliation synthesis and its application in photocatalysis and photoelectrochemical selective detection of trace amount of Cu^{2+}, Nanoscale 6 (2014) 1406–1415. https://doi.org/10.1039/C3NR04759H.

[17] Y. Zhang, T. Mori, L. Niu, J. Ye, Non-covalent doping of graphitic carbon nitride polymer with graphene: controlled electronic structure and enhanced optoelectronic conversion, Energy Environ. Sci. 4 (2011) 4517. https://doi.org/10.1039/c1ee01400e.

[18] J. Xu, L. Zhang, R. Shi, Y. Zhu, Chemical exfoliation of graphitic carbon nitride for efficient heterogeneous photocatalysis, J. Mater. Chem. A 1 (2013) 14766. https://doi.org/10.1039/c3ta13188b.

[19] Y. Zhang, Q. Zhang, Q. Shi, Z. Cai, Z. Yang, Acid-treated g-C_3N_4 with improved photocatalytic performance in the reduction of aqueous Cr (VI) under visible-light, Sep. Purif. Technol. 142 (2015) 251–257. https://doi.org/10.1016/j.seppur.2014.12.041.

[20] S. Challagulla, S. Payra, C. Chakraborty, S. Roy, Determination of band edges and their influences on photocatalytic reduction of nitrobenzene by bulk and exfoliated g-C_3N_4, Phys. Chem. Chem. Phys. 21 (2019) 3174–3183. https://doi.org/10.1039/C8CP06855K.

[21] S. Sun, J. Li, J. Cui, X. Gou, Q. Yang, Y. Jiang, S. Liang, Z. Yang, Simultaneously engineering K-doping and exfoliation into graphitic carbon nitride (g-C_3N_4) for enhanced photocatalytic hydrogen production, Int. J. Hydrog. Energy 44 (2019) 778–787. https://doi.org/10.1016/j.ijhydene.2018.11.019.

[22] A. Balakrishnan, M. Chinthala, Comprehensive review on advanced reusability of g-C_3N_4 based photocatalysts for the removal of organic pollutants, Chemosphere 297 (2022) 134190. https://doi.org/10.1016/j.chemosphere.2022.134190.

[23] R. Li, Y. Ren, P. Zhao, J. Wang, J. Liu, Y. Zhang, Graphitic carbon nitride (g-C_3N_4) nanosheets functionalized composite membrane with self-cleaning and antibacterial performance, J. Hazard. Mater. 365 (2019) 606–614. https://doi.org/10.1016/j.jhazmat.2018.11.033.

[24] S. Wang, g-C_3N_4 nanosheets as “on-off-on” selective fluorescence biosensor to detect ascorbic acid via redox reaction, J. Alloys Compd. 770 (2019) 952–958. https://doi.org/10.1016/j.jallcom.2018.08.182.

[25] Y. Huang, Y. Wang, Y. Bi, J. Jin, M.F. Ehsan, M. Fu, T. He, Preparation of 2D hydroxyl-rich carbon nitride nanosheets for photocatalytic reduction of CO_2, RSC Adv. 5 (2015) 33254–33261. https://doi.org/10.1039/C5RA04227E.

[26] Q. Lin, L. Li, S. Liang, M. Liu, J. Bi, L. Wu, Efficient synthesis of monolayer carbon nitride 2D nanosheet with tunable concentration and enhanced visible-light photocatalytic

activities, Appl. Catal. B Environ. 163 (2015) 135–142. https://doi.org/10.1016/j.apcatb.2014.07.053.

[27] H. Jiang, Y. Li, D. Wang, X. Hong, B. Liang, Recent Advances in Heteroatom Doped Graphitic Carbon Nitride (g-C_3N_4) and g-C_3N_4/Metal Oxide Composite Photocatalysts, Curr. Org. Chem. 24 (2020) 673–693. https://doi.org/10.2174/1385272824666200309151648.

[28] Y. Li, S. Wu, L. Huang, J. Wang, H. Xu, H. Li, Synthesis of carbon-doped g-C_3N_4 composites with enhanced visible-light photocatalytic activity, Mater. Lett. 137 (2014) 281–284. https://doi.org/10.1016/j.matlet.2014.08.142.

[29] N. Bao, X. Hu, Q. Zhang, X. Miao, X. Jie, S. Zhou, Synthesis of porous carbon-doped g-C_3N_4 nanosheets with enhanced visible-light photocatalytic activity, Appl. Surf. Sci. 403 (2017) 682–690. https://doi.org/10.1016/j.apsusc.2017.01.256.

[30] S. Thaweesak, S. Wang, M. Lyu, M. Xiao, P. Peerakiatkhajohn, L. Wang, Boron-doped graphitic carbon nitride nanosheets for enhanced visible light photocatalytic water splitting, Dalton Trans. 46 (2017) 10714–10720. https://doi.org/10.1039/C7DT00933J.

[31] Y.-P. Zhu, T.-Z. Ren, Z.-Y. Yuan, Mesoporous Phosphorus-Doped g-C_3N_4 Nanostructured Flowers with Superior Photocatalytic Hydrogen Evolution Performance, ACS Appl. Mater. Interfaces 7 (2015) 16850–16856. https://doi.org/10.1021/acsami.5b04947.

[32] W. Tang, Y. Tian, B. Chen, Y. Xu, B. Li, X. Jing, J. Zhang, S. Xu, Supramolecular Copolymerization Strategy for Realizing the Broadband White Light Luminescence Based on N-Deficient Porous Graphitic Carbon Nitride (g-C_3N_4), ACS Appl. Mater. Interfaces 12 (2020) 6396–6406. https://doi.org/10.1021/acsami.9b19338.

[33] C.T. Seto, G.M. Whitesides, Self-assembly based on the cyanuric acid-melamine lattice, J. Am. Chem. Soc. 112 (1990) 6409–6411. https://doi.org/10.1021/ja00173a046.

[34] A. Ranganathan, V.R. Pedireddi, C.N.R. Rao, Hydrothermal Synthesis of Organic Channel Structures: 1:1 Hydrogen-Bonded Adducts of Melamine with Cyanuric and Trithiocyanuric Acids, J. Am. Chem. Soc. 121 (1999) 1752–1753. https://doi.org/10.1021/ja983928o.

[35] Y. Jun, J. Park, S.U. Lee, A. Thomas, W.H. Hong, G.D. Stucky, Three-Dimensional Macroscopic Assemblies of Low-Dimensional Carbon Nitrides for Enhanced Hydrogen

Evolution, Angew. Chem. Int. Ed. 52 (2013) 11083–11087. https://doi.org/10.1002/anie.201304034.

[36] J. Zhang, G. Zhang, X. Chen, S. Lin, L. Möhlmann, G. Dołęga, G. Lipner, M. Antonietti, S. Blechert, X. Wang, Co-Monomer Control of Carbon Nitride Semiconductors to Optimize Hydrogen Evolution with Visible Light, Angew. Chem. Int. Ed. 51 (2012) 3183–3187. https://doi.org/10.1002/anie.201106656.

[37] J. Zhang, X. Chen, K. Takanabe, K. Maeda, K. Domen, J.D. Epping, X. Fu, M. Antonietti, X. Wang, Synthesis of a Carbon Nitride Structure for Visible-Light Catalysis by Copolymerization, Angew. Chem. Int. Ed. 49 (2010) 441–444. https://doi.org/10.1002/anie.200903886.

[38] J. Wang, S. Wang, A critical review on graphitic carbon nitride (g-C_3N_4)-based materials: Preparation, modification and environmental application, Coord. Chem. Rev. 453 (2022) 214338. https://doi.org/10.1016/j.ccr.2021.214338.

[39] J. Xiong, J. Di, J. Xia, W. Zhu, H. Li, Surface Defect Engineering in 2D Nanomaterials for Photocatalysis, Adv. Funct. Mater. 28 (2018) 1801983. https://doi.org/10.1002/adfm.201801983.

[40] O. Iqbal, H. Ali, N. Li, A.I. Al-Sulami, K. F Alshammari, H.S.M. Abd-Rabboh, Y. Al-Hadeethi, I.U. Din, A.I. Alharthi, R. Altamimi, A. Zada, Z. Wang, A. Hayat, M. Zahid Ansari, A review on the synthesis, properties, and characterizations of graphitic carbon nitride (g-C_3N_4) for energy conversion and storage applications, Mater. Today Phys. 34 (2023) 101080. https://doi.org/10.1016/j.mtphys.2023.101080.

[41] S. Li, G. Dong, R. Hailili, L. Yang, Y. Li, F. Wang, Y. Zeng, C. Wang, Effective photocatalytic H_2O_2 production under visible light irradiation at g-C_3N_4 modulated by carbon vacancies, Appl. Catal. B Environ. 190 (2016) 26–35. https://doi.org/10.1016/j.apcatb.2016.03.004.

[42] H. Yu, R. Shi, Y. Zhao, T. Bian, Y. Zhao, C. Zhou, G.I.N. Waterhouse, L. Wu, C. Tung, T. Zhang, Alkali-Assisted Synthesis of Nitrogen Deficient Graphitic Carbon Nitride with Tunable Band Structures for Efficient Visible-Light-Driven Hydrogen Evolution, Adv. Mater. 29 (2017) 1605148. https://doi.org/10.1002/adma.201605148.

[43] G. Dong, D.L. Jacobs, L. Zang, C. Wang, Carbon vacancy regulated photoreduction of NO to N_2 over ultrathin g-C_3N_4 nanosheets, Appl. Catal. B Environ. 218 (2017) 515–524. https://doi.org/10.1016/j.apcatb.2017.07.010.

[44] Y. Wang, L. Liu, T. Ma, Y. Zhang, H. Huang, 2D Graphitic Carbon Nitride for Energy Conversion and Storage, Adv. Funct. Mater. 31 (2021) 2102540. https://doi.org/10.1002/adfm.202102540.

[45] P. Dhiman, G. Rana, A. Kumar, G. Sharma, D.-V.N. Vo, Mu. Naushad, ZnO-based heterostructures as photocatalysts for hydrogen generation and depollution: a review, Environ. Chem. Lett. 20 (2022) 1047–1081. https://doi.org/10.1007/s10311-021-01361-1.

[46] R. Ma, S. Zhang, L. Li, P. Gu, T. Wen, A. Khan, S. Li, B. Li, S. Wang, X. Wang, Enhanced Visible-Light-Induced Photoactivity of Type-II CeO_2 /g-C_3N_4 Nanosheet toward Organic Pollutants Degradation, ACS Sustain. Chem. Eng. 7 (2019) 9699–9708. https://doi.org/10.1021/acssuschemeng.9b01477.

[47] L. Jiang, X. Yuan, G. Zeng, J. Liang, Z. Wu, H. Yu, D. Mo, H. Wang, Z. Xiao, C. Zhou, Nitrogen self-doped g-C_3N_4 nanosheets with tunable band structures for enhanced photocatalytic tetracycline degradation, J. Colloid Interface Sci. 536 (2019) 17–29. https://doi.org/10.1016/j.jcis.2018.10.033.

[48] X. Wang, K. Maeda, A. Thomas, K. Takanabe, G. Xin, J.M. Carlsson, K. Domen, M. Antonietti, A metal-free polymeric photocatalyst for hydrogen production from water under visible light, Nat. Mater. 8 (2009) 76–80. https://doi.org/10.1038/nmat2317.

[49] Q. Han, B. Wang, J. Gao, Z. Cheng, Y. Zhao, Z. Zhang, L. Qu, Atomically Thin Mesoporous Nanomesh of Graphitic C_3N_4 for High-Efficiency Photocatalytic Hydrogen Evolution, ACS Nano 10 (2016) 2745–2751. https://doi.org/10.1021/acsnano.5b07831.

[50] P. Niu, Y. Yang, J.C. Yu, G. Liu, H.-M. Cheng, Switching the selectivity of the photoreduction reaction of carbon dioxide by controlling the band structure of a g-C_3N_4 photocatalyst, Chem. Commun. 50 (2014) 10837. https://doi.org/10.1039/C4CC03060E.

[51] X. Yang, J. Peng, L. Zhao, H. Zhang, J. Li, P. Yu, Y. Fan, J. Wang, H. Liu, S. Dou, Insights on advanced g-C_3N_4 in energy storage: Applications, challenges, and future, Carbon Energy 6 (2024) e490. https://doi.org/10.1002/cey2.490.

[52] M. Wu, Q. Wang, Q. Sun, P. Jena, Functionalized Graphitic Carbon Nitride for Efficient Energy Storage, J. Phys. Chem. C 117 (2013) 6055–6059. https://doi.org/10.1021/jp311972f.

[53] A.B. Jorge, F. Corà, A. Sella, P.F. McMillan, D.J.L. Brett, Electrochemical properties of graphitic carbon nitrides, Int. J. Nanotechnol. 11 (2014) 737. https://doi.org/10.1504/IJNT.2014.063784.

[54] M. Hankel, D. Ye, L. Wang, D.J. Searles, Lithium and Sodium Storage on Graphitic Carbon Nitride, J. Phys. Chem. C 119 (2015) 21921–21927. https://doi.org/10.1021/acs.jpcc.5b07572.

[55] J. Chen, Z. Mao, L. Zhang, D. Wang, R. Xu, L. Bie, B.D. Fahlman, Nitrogen-Deficient Graphitic Carbon Nitride with Enhanced Performance for Lithium Ion Battery Anodes, ACS Nano 11 (2017) 12650–12657. https://doi.org/10.1021/acsnano.7b07116.

[56] J. Liu, Y. Zhang, L. Zhang, F. Xie, A. Vasileff, S. Qiao, Graphitic Carbon Nitride (g-C_3N_4)-Derived N-Rich Graphene with Tuneable Interlayer Distance as a High-Rate Anode for Sodium-Ion Batteries, Adv. Mater. 31 (2019) 1901261. https://doi.org/10.1002/adma.201901261.

[57] S. Wang, J. Zhang, B. Li, H. Sun, S. Wang, Engineered Graphitic Carbon Nitride-Based Photocatalysts for Visible-Light-Driven Water Splitting: A Review, Energy Fuels 35 (2021) 6504–6526. https://doi.org/10.1021/acs.energyfuels.1c00503.

[58] D. Huang, X. Yan, M. Yan, G. Zeng, C. Zhou, J. Wan, M. Cheng, W. Xue, Graphitic Carbon Nitride-Based Heterojunction Photoactive Nanocomposites: Applications and Mechanism Insight, ACS Appl. Mater. Interfaces 10 (2018) 21035–21055. https://doi.org/10.1021/acsami.8b03620.

[59] W.-J. Ong, L.-L. Tan, Y.H. Ng, S.-T. Yong, S.-P. Chai, Graphitic Carbon Nitride (g-C_3N_4)-Based Photocatalysts for Artificial Photosynthesis and Environmental Remediation: Are We a Step Closer To Achieving Sustainability?, Chem. Rev. 116 (2016) 7159–7329. https://doi.org/10.1021/acs.chemrev.6b00075.

[60] J. Fu, J. Yu, C. Jiang, B. Cheng, g-C_3N_4-Based Heterostructured Photocatalysts, Adv. Energy Mater. 8 (2018) 1701503. https://doi.org/10.1002/aenm.201701503.

[61] Z. Chen, S. Zhang, Y. Liu, N.S. Alharbi, S.O. Rabah, S. Wang, X. Wang, Synthesis and fabrication of g-C_3N_4-based materials and their application in elimination of pollutants, Sci. Total Environ. 731 (2020) 139054. https://doi.org/10.1016/j.scitotenv.2020.139054.

[62] X. Zhang, X. Yuan, L. Jiang, J. Zhang, H. Yu, H. Wang, G. Zeng, Powerful combination of 2D g-C_3N_4 and 2D nanomaterials for photocatalysis: Recent advances, Chem. Eng. J. 390 (2020) 124475. https://doi.org/10.1016/j.cej.2020.124475.

[63] K. Kočí, M. Reli, I. Troppová, M. Šihor, J. Kupková, P. Kustrowski, P. Praus, Photocatalytic decomposition of N_2O over TiO_2/g-C_3N_4 photocatalysts heterojunction, Appl. Surf. Sci. 396 (2017) 1685–1695. https://doi.org/10.1016/j.apsusc.2016.11.242.

[64] D. Chen, K. Wang, T. Ren, H. Ding, Y. Zhu, Synthesis and characterization of the ZnO/mpg-C_3N_4 heterojunction photocatalyst with enhanced visible light photoactivity, Dalton Trans 43 (2014) 13105–13114. https://doi.org/10.1039/C4DT01347F.

[65] Y. Chen, A. Li, X. Fu, Z. Peng, One-Step Calcination to Gain Exfoliated g-C_3N_4/MoO_2 Composites for High-Performance Photocatalytic Hydrogen Evolution, Molecules 27 (2022) 7178. https://doi.org/10.3390/molecules27217178.

[66] S. Li, W. Zhao, D. Xiong, Y. Ye, J. Ma, Y. Gu, g-C_3N_4/TiO_2 uniformly distributed microspheres: preparation for enhanced photocatalytic performance by co-calcination, J. Mater. Sci. Mater. Electron. 34 (2023) 47. https://doi.org/10.1007/s10854-022-09391-3.

[67] N. Devi, S. Sahoo, R. Kumar, R.K. Singh, A review of the microwave-assisted synthesis of carbon nanomaterials, metal oxides/hydroxides and their composites for energy storage applications, Nanoscale 13 (2021) 11679–11711. https://doi.org/10.1039/D1NR01134K.

[68] X. Wang, W. Yang, F. Li, Y. Xue, R. Liu, Y. Hao, In Situ Microwave-Assisted Synthesis of Porous N-TiO_2/g-C_3N_4 Heterojunctions with Enhanced Visible-Light Photocatalytic Properties, Ind. Eng. Chem. Res. 52 (2013) 17140–17150. https://doi.org/10.1021/ie402820v.

[69] A. Seza, F. Soleimani, N. Naseri, M. Soltaninejad, S.M. Montazeri, S.K. Sadrnezhaad, M.R. Mohammadi, H.A. Moghadam, M. Forouzandeh, M.H. Amin, Novel microwave-assisted synthesis of porous g-C_3N_4/SnO_2 nanocomposite for solar water-splitting, Appl. Surf. Sci. 440 (2018) 153–161. https://doi.org/10.1016/j.apsusc.2018.01.133.

[70] L. Bai, H. Huang, S. Yu, D. Zhang, H. Huang, Y. Zhang, Role of transition metal oxides in g-C_3N_4-based heterojunctions for photocatalysis and supercapacitors, J. Energy Chem. 64 (2022) 214–235. https://doi.org/10.1016/j.jechem.2021.04.057.

[71] X. Zhang, S.P. Jiang, Layered g-C_3N_4/TiO_2 nanocomposites for efficient photocatalytic water splitting and CO2 reduction: a review, Mater. Today Energy 23 (2022) 100904. https://doi.org/10.1016/j.mtener.2021.100904.

[72] J. Fu, Q. Xu, J. Low, C. Jiang, J. Yu, Ultrathin 2D/2D WO_3/g-C_3N_4 step-scheme H_2-production photocatalyst, Appl. Catal. B Environ. 243 (2019) 556–565. https://doi.org/10.1016/j.apcatb.2018.11.011.

[73] J. Wu, Y. Zhang, J. Zhou, K. Wang, Y.-Z. Zheng, X. Tao, Uniformly assembling n-type metal oxide nanostructures (TiO_2 nanoparticles and SnO_2 nanowires) onto P doped g-C_3N_4 nanosheets for efficient photocatalytic water splitting, Appl. Catal. B Environ. 278 (2020) 119301. https://doi.org/10.1016/j.apcatb.2020.119301.

[74] Y. He, L. Zhang, B. Teng, M. Fan, New Application of Z-Scheme Ag_3PO_4/g-C_3N_4 Composite in Converting CO_2 to Fuel, Environ. Sci. Technol. 49 (2015) 649–656. https://doi.org/10.1021/es5046309.

[75] Y. He, Y. Wang, L. Zhang, B. Teng, M. Fan, High-efficiency conversion of CO_2 to fuel over ZnO/g-C_3N_4 photocatalyst, Appl. Catal. B Environ. 168–169 (2015) 1–8. https://doi.org/10.1016/j.apcatb.2014.12.017.

[76] W. Wang, M. Chen, D. Huang, G. Zeng, C. Zhang, C. Lai, C. Zhou, Y. Yang, M. Cheng, L. Hu, W. Xiong, Z. Li, Z. Wang, An overview on nitride and nitrogen-doped photocatalysts for energy and environmental applications, Compos. Part B Eng. 172 (2019) 704–723. https://doi.org/10.1016/j.compositesb.2019.05.097.

[77] H. Montigaud, B. Tanguy, G. Demazeau, I. Alves, M. Birot, J. Dunogues, Solvothermal Synthesis of the Graphitic Form of C_3N_4 as Macroscopic Sample, Mater. Sci. Forum 325–326 (2000) 31–36. https://doi.org/10.4028/www.scientific.net/MSF.325-326.31.

[78] Z. Huang, Q. Sun, K. Lv, Z. Zhang, M. Li, B. Li, Effect of contact interface between TiO_2 and g-C_3N_4 on the photoreactivity of g-C_3N_4/TiO_2 photocatalyst: (0 0 1) vs (1 0 1) facets of

TiO_2, Appl. Catal. B Environ. 164 (2015) 420–427. https://doi.org/10.1016/j.apcatb.2014.09.043.

[79] R. Hao, G. Wang, H. Tang, L. Sun, C. Xu, D. Han, Template-free preparation of macro/mesoporous g-C_3N_4/TiO_2 heterojunction photocatalysts with enhanced visible light photocatalytic activity, Appl. Catal. B Environ. 187 (2016) 47–58. https://doi.org/10.1016/j.apcatb.2016.01.026.

[80] K. Vignesh, S. Kang, B.S. Kwak, M. Kang, Meso-porous ZnO nano-triangles @ graphitic-C_3N_4 nano-foils: Fabrication and Recyclable photocatalytic activity, Sep. Purif. Technol. 147 (2015) 257–265. https://doi.org/10.1016/j.seppur.2015.04.043.

[81] S. Kumar, S. T, B. Kumar, A. Baruah, V. Shanker, Synthesis of Magnetically Separable and Recyclable g-C_3N_4–Fe_3O_4 Hybrid Nanocomposites with Enhanced Photocatalytic Performance under Visible-Light Irradiation, J. Phys. Chem. C 117 (2013) 26135–26143. https://doi.org/10.1021/jp409651g.

[82] A.N. Shafawi, R.A. Mahmud, K. Ahmed Ali, L.K. Putri, N.I. Md Rosli, A.R. Mohamed, Bi_2O_3 particles decorated on porous g-C_3N_4 sheets: Enhanced photocatalytic activity through a direct Z-scheme mechanism for degradation of Reactive Black 5 under UV–vis light, J. Photochem. Photobiol. Chem. 389 (2020) 112289. https://doi.org/10.1016/j.jphotochem.2019.112289.

[83] L. Huang, H. Xu, R. Zhang, X. Cheng, J. Xia, Y. Xu, H. Li, Synthesis and characterization of g-C_3N_4/MoO_3 photocatalyst with improved visible-light photoactivity, Appl. Surf. Sci. 283 (2013) 25–32. https://doi.org/10.1016/j.apsusc.2013.05.106.

[84] W. Zhu, F. Sun, R. Goei, Y. Zhou, Construction of WO_3–g-C_3N_4 composites as efficient photocatalysts for pharmaceutical degradation under visible light, Catal. Sci. Technol. 7 (2017) 2591–2600. https://doi.org/10.1039/C7CY00529F.

[85] N. Kumar, M. Kumari, M. Ismael, M. Tahir, R.K. Sharma, K. Kumari, J.R. Koduru, P. Singh, Graphitic carbon nitride (g–C_3N_4)–assisted materials for the detection and remediation of hazardous gases and VOCs, Environ. Res. 231 (2023) 116149. https://doi.org/10.1016/j.envres.2023.116149.

[86] V.S. Bhati, V. Takhar, R. Raliya, M. Kumar, R. Banerjee, Recent advances in g-C_3N_4 based gas sensors for the detection of toxic and flammable gases: a review, Nano Express 3 (2022) 014003. https://doi.org/10.1088/2632-959X/ac477b.

[87] J. Cao, C. Qin, Y. Wang, B. Zhang, Y. Gong, H. Zhang, G. Sun, H. Bala, Z. Zhang, Calcination Method Synthesis of SnO_2/g-C_3N_4 Composites for a High-Performance Ethanol Gas Sensing Application, Nanomaterials 7 (2017) 98. https://doi.org/10.3390/nano7050098.

[88] X. Li, Y. Li, G. Sun, N. Luo, B. Zhang, Z. Zhang, Synthesis of a Flower-Like g-C_3N_4/ZnO Hierarchical Structure with Improved CH4 Sensing Properties, Nanomaterials 9 (2019) 724. https://doi.org/10.3390/nano9050724.

[89] B. Zeng, L. Zhang, X. Wan, H. Song, Y. Lv, Fabrication of α-Fe_2O_3/g-C_3N_4 composites for cataluminescence sensing of H_2S, Sens. Actuators B Chem. 211 (2015) 370–376. https://doi.org/10.1016/j.snb.2015.01.094.

[90] A. Akhtar, C. Jiao, X. Chu, S. Liang, Y. Dong, L. He, Acetone sensing properties of the g–C_3N_4–CuO nanocomposites prepared by hydrothermal method, Mater. Chem. Phys. 265 (2021) 124375. https://doi.org/10.1016/j.matchemphys.2021.124375.

Chapter 3. Visible Light Photocatalytic Degradation of Nitenpyram using Graphitic Carbon Nitride Nanosheets

3.1 Introduction

Neonicotinoids are a class of synthetic and neurotoxic insecticides that have been widely spread in nearly 120 counties worldwide as a result of their extensive use in agroforestry, aquaculture, crop protection, and pest management[1–3]. Seven neonicotinoids are available in the market, which are divided into three main groups: five-membered ring structure, six-member ring structure, and non-cyclic compounds[4]. Owing to their long half-life in soil and high solubility in water, neonicotinoids have the potential to accumulate in soil and percolate into groundwater and surface water[5,6]. The documented neonicotinoid content in some rivers in Australia is 118ng/L[2], whereas specific water resources in Iowa, USA, and Ontario, Canada, have been found to contain neonicotinoids at concentrations of 57 and 280ng/L, respectively[3]. The presence of neonicotinoids in the environment may directly harm non-targeted organisms such as honeybees or infiltrate food chains, endangering human health through trophic transfer[7–10]. It has been studied that long-term exposure to neonicotinoids will cause neurological disorders in children and Alzheimer's in aged people[11]. Hence, it is imperative to devise economical approaches to alleviate the contamination from the persistence and accumulation of neonicotinoids.

Nitenpyram (NTP), a second generation of neonicotinoid, has been extensively used in agriculture because of its relatively low mammalian toxicity and no apparent long-term cumulative effects. NTP affects the neuronal nicotinic acetylcholine receptors (nAChRs) of the nervous system in insects[12]. It is registered in more than 110 countries and regions and has been employed on more than 130 staple crops. With its extensive application and high water solubility (590 gL^{-1}), NTP is

one of the most frequently detected neonicotinoids in groundwater and surface water[13–15]. Therefore, removing NTP from the contaminated water is a major environmental issue. In recent years, photocatalytic degradation of NTP has proved to be the most appropriate method because of its environmental friendliness and efficiency [14-15]. Compared with physical methods (e.g., adsorption, membrane filtration, etc.), biological and/or electrochemical degradation methods, solar-driven photocatalytic degradation of NTP shows high degradation efficiency and consistent sustainability advantages. Therefore, it is crucial to prioritize the advancement of cost-effective photocatalysts that exhibit high absorption efficiency of visible light.

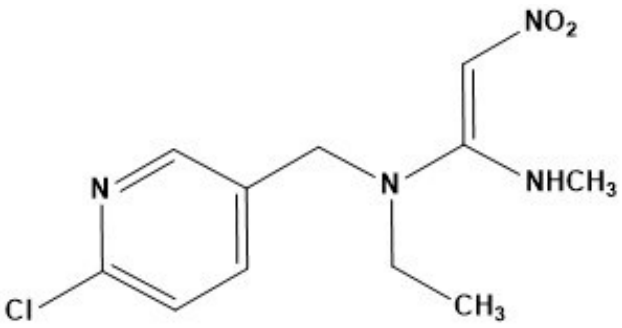

Figure 3.1 Structure of Nitenpyram

Despite recent significant technological advances, a couple of major challenges remain in the photocatalytic degradation of NTP or other organic pollutants: (i) the low visible-light harvesting efficiency, (ii) the fast recombination of photogenerated electrons and holes, and (iii) the potential of secondary pollution due to the use of toxic metal-based semiconductors. The discovery of graphitic carbon nitride (g-C_3N_4) as a metal-free conjugated polymer semiconductor has stimulated intensive research in sustainable photocatalytic degradation of water contaminants[16]. Bulk g-C_3N_4 (three-dimensional) can be readily obtained by pyrolysis of many N-rich precursors, such as melamine[17], urea[18], thiourea, and cyanamide. However, the photocatalytic efficiency of bulk g-C_3N_4 is quite low because of its small specific surface area, marginal visible light absorption,

and low electric conductivity [18]. Exfoliation of bulk g-C_3N_4 has been intensively employed to increase the specific surface area and decrease the recombination of photogenerated charges caused by the reduced diffusion path lengths.

In this chapter, a facile thermal exfoliation method was implemented to prepare two-dimensional (2D) g-C_3N_4 nanosheets for the photocatalytic degradation of NTP under visible-light irradiation. The composition, morphology, crystalline structure, and specific surface area of the g-C_3N_4 nanosheets have been characterized through XPS, TEM, XRD, and BET surface area analyzer. The photocatalytic performance of g-C_3N_4 nanosheets in degrading NTP was investigated, and the impact of several operating parameters on the degradation efficiency was analyzed.

3.2 Materials and Methods

3.2.1 Materials

Melamine (99%), ACS-grade hydrochloric acid, sodium hydroxide, HPLC-grade acetonitrile, and water were acquired from Fisher Scientific. Nitenpyram (≥98%) was purchased from Sigma-Aldrich. All these chemicals were used as received, without any additional purification. All the aqueous solutions used in the photocatalytic reactions were prepared with ultrapure water generated from a laboratory MilliQ water system.

3.2.2 Synthesis of g-C_3N_4 nanosheets

Melamine is used to synthesize g-C_3N_4 nanosheets by a two-step calcination process [19]. Firstly, 5.0 g of melamine was put in a crucible with a cover (to control polymerization) and heated at 520°C for 4 hours at a ramp rate of 2.5°C/min in a muffled furnace to make bulk g-C_3N_4. The obtained yellow product was then milled into fine powder using a mortar. In the second step, 1.0 g of bulk g-C_3N_4 yellow powder was placed in a crucible without the cover (to allow gas escape

and refine the structure) and heated again at 520°C for 4 hours at a ramp rate of 2.5°C/min in a muffled furnace. After cooling to room temperature, the g-C_3N_4 nanosheets were obtained.

3.2.3 Characterization

High-resolution transmission electron microscopy (TEM) was performed on a Thermo Scientific Talos F200X G2. X-ray diffraction (XRD) was used to analyze the structure of the g-C_3N_4 nanosheets. The Fourier transform infrared (FTIR), from 400 to 4000 cm^{-1}, was used to determine the molecular structure. X-ray photoelectron spectroscopy (XPS) was used to determine the elemental composition of the prepared g-C_3N_4 nanosheets. The UV-Vis diffuse reflectance spectra (UV-DRS) of g-C_3N_4 nanosheets were measured using a UV-3900 UV-Vis-Nir spectrophotometer. (BET) surface area was measured on an N_2 adsorption-desorption assay on a Micro active for Tristar II.

3.2.4 Degradation of NTP under visible light

The reaction for the degradation of NTP under visible light (300W Xenon lamp with a 420-nm cut off filter) was carried out via a photocatalytic batch jacketed reactor at a temperature of 30°C. Reaction temperature was controlled using a refrigerated/heating circulator (FP50-HL, Julabo, USA). NTP degradation was carried out using 50.0 ml of NTP water solution with an initial NTP concentration of 10 mg L^{-1} and a catalyst dosage of 1.0 gL^{-1}. g-C_3N_4 nanosheets and NTP solution were stirred in the dark for 1 hour to achieve adsorption equilibrium. After the first hour, the Xenon lamp was turned on to speed up the reaction, and 1.0 ml of the suspension was extracted and filtered using a 0.22μm filter at each sampling point. The samples were analyzed using high-performance liquid chromatography (HPLC) system.

3.2.5 HPLC Detection Condition:

To determine the concentration of NTP, an Agilent HPLC DAD detector was used, the chromatographic separation was determined using a C18 column, and a mixture of Water and Acetonitrile (80:20) was used as an isocratic mobile phase, and the flowrate was 0.6 ml min^{-1}. The detection wavelength was 270 nm, and the column temperature was maintained at 30°C[19].

3.3 Results and Discussion

3.3.1 Powder XRD

XRD is used to determine the prepared nanosheets' structure and crystallinity. The XRD patterns of g-C_3N_4 feature two pronounced diffraction peaks at 13.08 and 27.72° as illustrated in Fig. 3.2(a) The peak at 13.08° resembles the (100) crystal plane of g-C_3N_4, recognized as the interlayer repetitive component of tri-s-triazine. The most substantial peak at 27.72° fits the (002) crystal plane attributed as an interplanar stacking ring of conjugated aromatic rings[19,20]. Fig. 3.2(b) also compares the XRD patterns of g-C_3N_4 before and after photocatalytic reactions. It is observed that the XRD pattern of g-C_3N_4 after the reaction is almost identical to that before the photocatalytic reaction, as there is no significant peak shift.

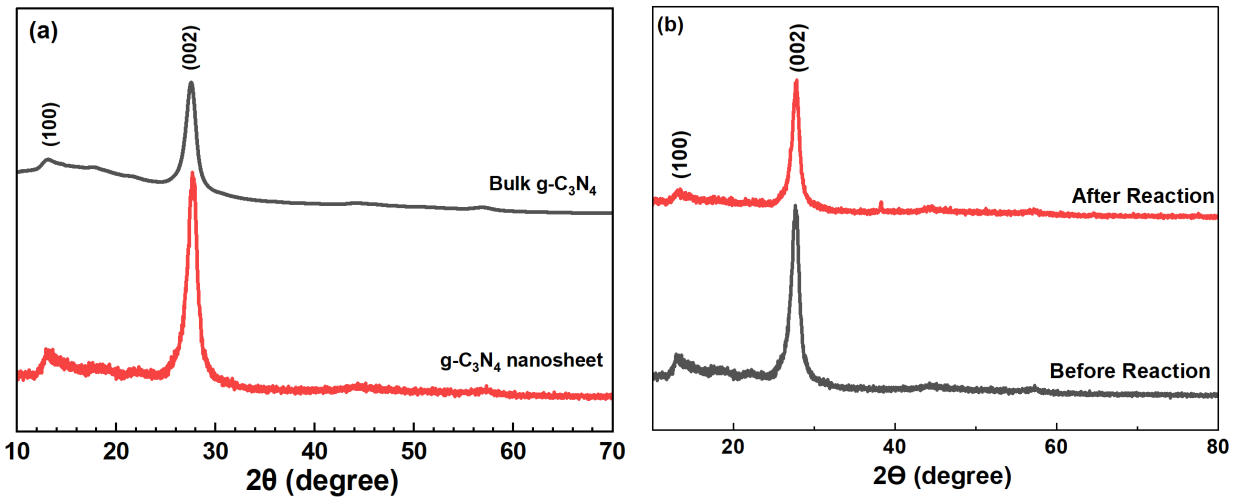

Figure 3.2 XRD of bulk g-C_3N_4 and g-C_3N_4 nanosheets(a) g-C_3N_4 nanosheets before and after the reaction(b)

3.3.2 FT-IR

FTIR was used to characterize the molecular structure of the catalysts. The FTIR spectra of the Bulk g-C_3N_4 and g-C_3N_4 nanosheets[21] can be seen in Fig. 3.3(a), and the FTIR spectra of nanosheets before and after the reaction are shown in Fig. 3.3(b). Very similarly, there are no noticeable peak shifts in the IR spectra of g-C_3N_4 before and after the reaction. The peak in wavelength number 810cm^{-1} is connected to the bending vibration of heptazine rings, and the peaks between 1200-1600cm^{-1} refer to the distinctive stretching mode of CN in heterocycles.[19] The peak between 3000-3300cm^{-1} corresponds to the amino group's N-H or O-H bond stretching vibration[22].

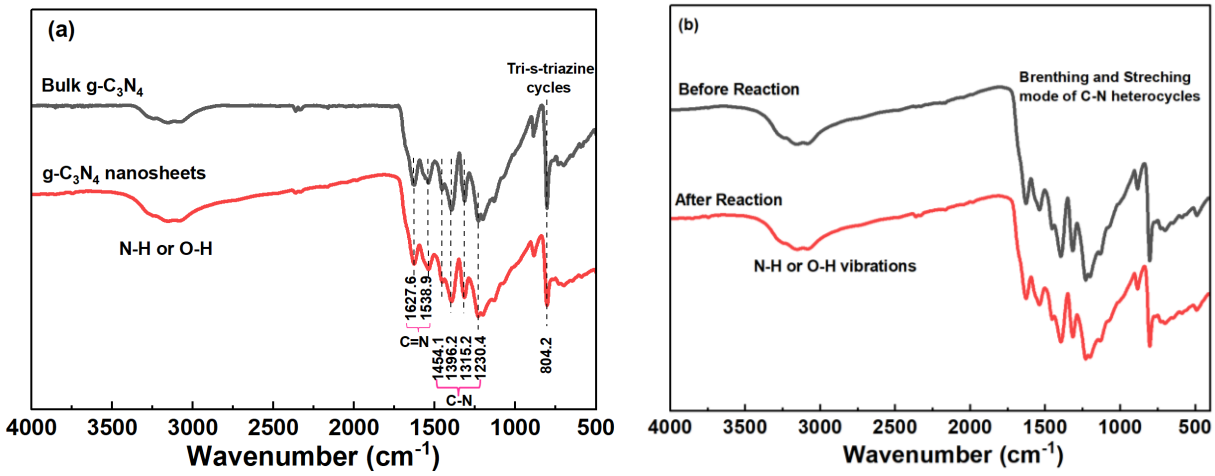

Figure 3.3 FTIR spectra, bulk g-C_3N_4 and g-C_3N_4 nanosheets(a) g-C_3N_4 nanosheets before and after the reaction(b)

3.3.3 XPS

The elemental composition of the catalyst was studied using XPS, as it can be seen in Figure 3.4 (a) that the catalyst mainly consists of C and N. The C 1s spectra can be detached into two peaks at a value approxiamtely 284.8 eV and 288.1 eV, corresponding to the signal of the standard reference carbon and the sp^2-hybridized carbon bonded to N inside the triazine rings. In the N 1s spectra, the peak around 398.5 eV was deconvoluted at around 399.4 eV, 401.01 eV and 404.6 eV[21]. The prominent peaks at 398.5 and 399.4 eV could be allocated to the sp^2-bonded N atoms within the triazine rings and the tertiary connecting N atom (N-(C)3). In addition, the peak of about 401.01 eV could be attributed to the amino functional groups containing hydrogen (C-N-H), and 404.6 eV is the charging effect. In the O 1s spectrum, there is only one peak at 532.1 eV due to the small quantity of water[21].

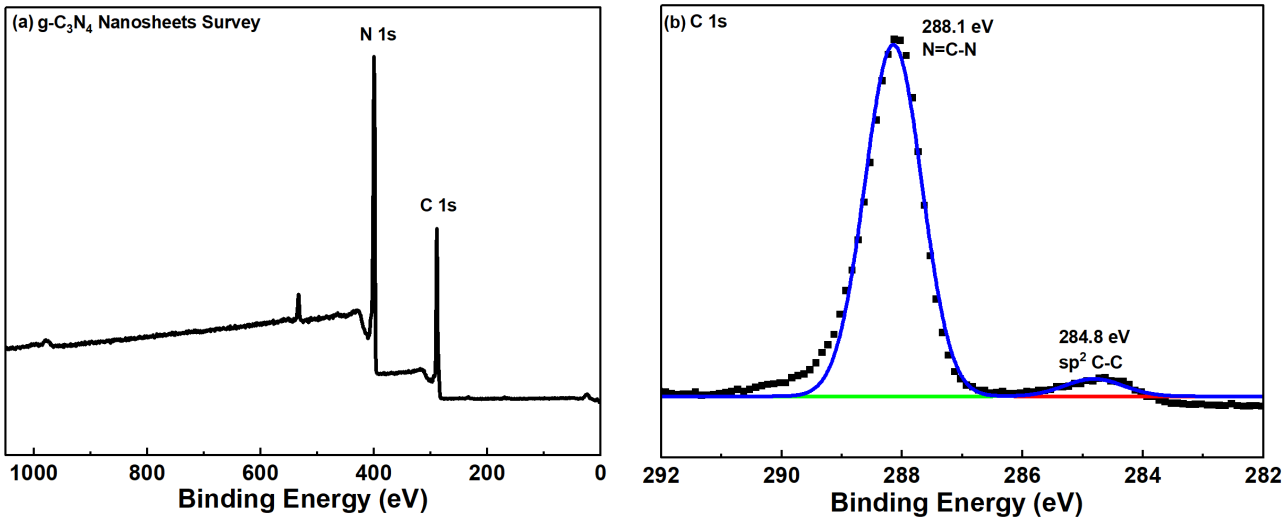

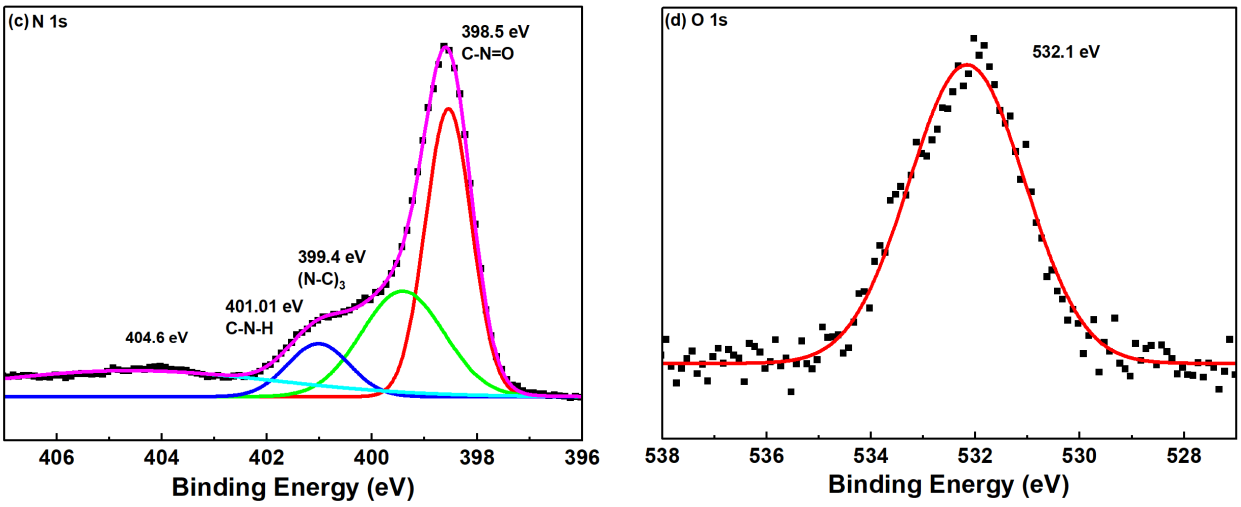

Figure 3.4 XPS survey scan of g-C_3N_4 (a) and high-resolution spectrum for C 1s (b), N 1s (c), and O 1s (d)

3.3.4 UV-DRS

The optical properties of the nanosheets were analyzed using UV diffuse reflectance spectra. According to the literature, the band gap of g-C_3N_4 is 2.7 eV, suitable for absorption in visible regions. With the reflectance spectra, we can find the band gap energy (E_g) of the prepared g-C_3N_4 nanosheets using equation (3-1) and Tauc plot[23].

$$(\alpha hv)^{1/n} = A(hv-Eg) \qquad (3\text{-}1)$$

Where h is the planks constant, v is radiation frequency, α is the absorption coefficient, n is the transition state of the semiconductor, and A is the proportionality constant. According to the theory of P.Kubelka and F. Munk, the reflectance spectra can be transformed into absorbance by using equation (3-2)[23]

$$F(R\infty) = K/S = \frac{(1-R\infty)2}{2R\infty} \qquad (3\text{-}2)$$

Where $R\infty = \frac{R\ sample}{R\ standard}$ is the reflectance of an infinitely thick specimen, while K is absorption and S is the scattering coefficient. Putting $F(R\infty)$ instead of α in equation 3-1

$$(F(R\infty).h\nu)^{1/n} = B(h\nu - Eg) \quad (3\text{-}3)$$

Where n = ½ is for direct, two is for indirect transition, and B is the proportionality constant that depends on material properties and type of material. The value of n for g-C_3N_4 is two indirect transitions[24]. The value of E_g of the prepared g-C_3N_4 nanosheets is 2.66eV.

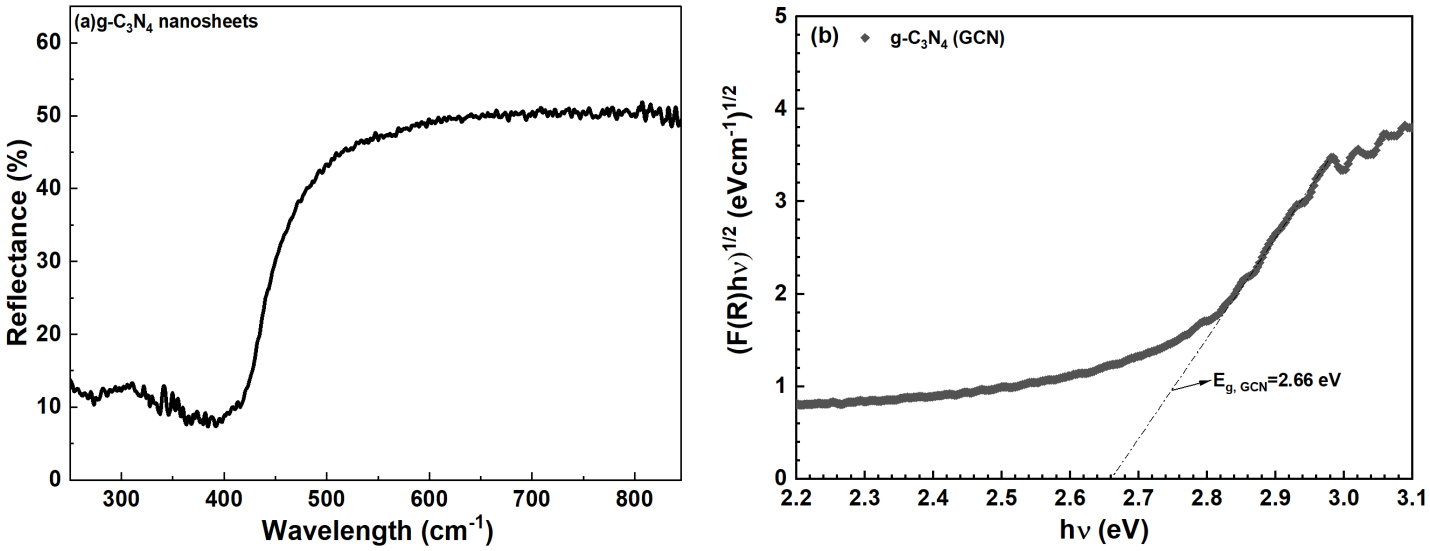

Figure 3.5UV DRS (a) Reflectance spectra (b) band gap energy of g-C_3N_4 nanosheets

3.3.5 BET Analysis

The nitrogen adsorption and desorption isotherms of the prepared bulk g-C_3N_4 and nanosheets are shown in Fig 3.6. The N_2 isotherms show strong absorption at relative pressure above 0.8, indicating meso or micropores. The pore size of the bulk and nanosheets is 5.23 and 0.978 nm, respectively, and the surface area for the bulk is 9.51 and 25.81m^2/g for the nanosheets. The BET analysis indicates an increase in the surface area of the nanosheets, increasing their overall photocatalytic performance and redox ability.

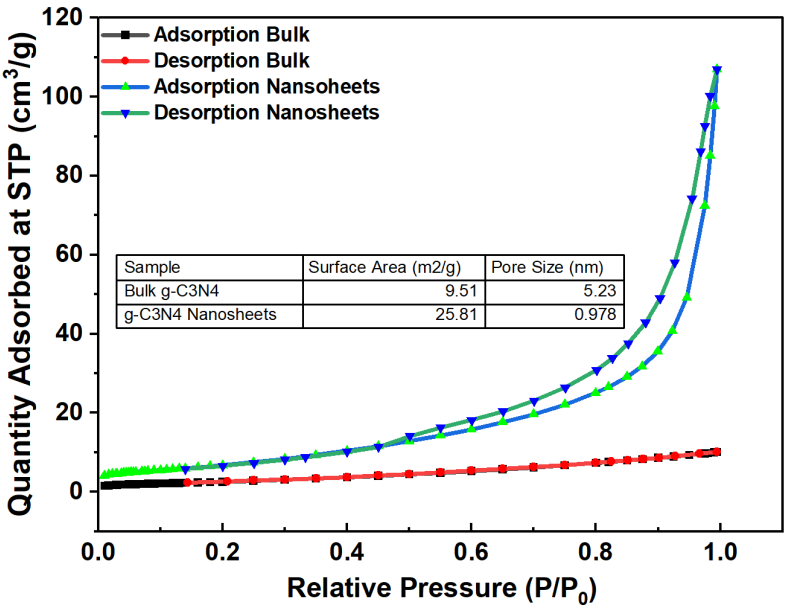

Figure 3.6 N_2 adsorption and desorption isotherms

3.3.6 TEM

To study the morphology of the prepared g-C_3N_4 nanosheets the transmission electron microscopy (TEM) was used, and the results are shown in figure 3.7. As it can be seen in the figure that, the prepared nanosheets have a wrinkled surface with some pores, indicating that the exfoliation increases the surface area of the nanosheets making it suitable for pollutant removal under visible light.

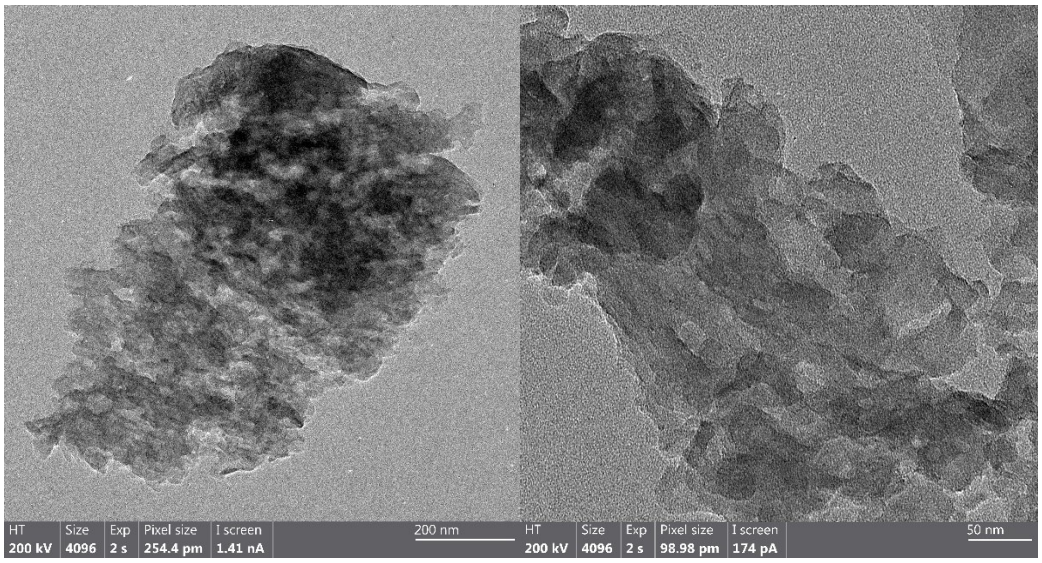

Figure 3.7 TEM images of g-C_3N_4 nanosheets

3.3.7 Photocatalytic study of g-C_3N_4 nanosheets

The photocatalytic ability of the prepared g-C_3N_4 nanosheets was studied under visible light for the degradation of NTP. Fig. 3.8(a) demonstrates the variation in the concentration of NTP with the passage of time in the presence of g-C_3N_4 nanosheets and bulk g-C_3N_4. At first, the reactor was kept in the dark for 1 hour to achieve equilibrium; the degradation of NTP for both bulk and nanosheets was similar in the dark, which is around 32%. The change occurred when the light was turned on for 3 hours to speed up the reaction. So, after 3 hours, 99% of the NTP was degraded in the presence of g-C_3N_4 nanosheets and 79% in the presence of bulk g-C_3N_4. So, g-C_3N_4 nanosheets perform well under visible light and can degrade 99% of NTP (initial concentration 10ppm) in 4 hours. The photocatalytic performance increased because of the modification in the structure of nanosheets. This change in structure increases its surface area and provides more active sites for the photocatalytic reaction, increasing its overall photocatalytic efficiency compared to bulk g-C_3N_4. As shown in Figure 3.8(c), the reaction was carried out three times. The average error was ±0.39, showing that the experiment is valid and repeatable. The reaction rates for the bulk and

nanosheets are shown in Figure 3.8(d), which are 0.00658 min^{-1} and 0.0191 min^{-1}. The rates were determined by using equation (3-4)

$$ln\frac{Ct}{C0} = -kt \qquad (3\text{-}4)$$

Where k is reaction rate constant

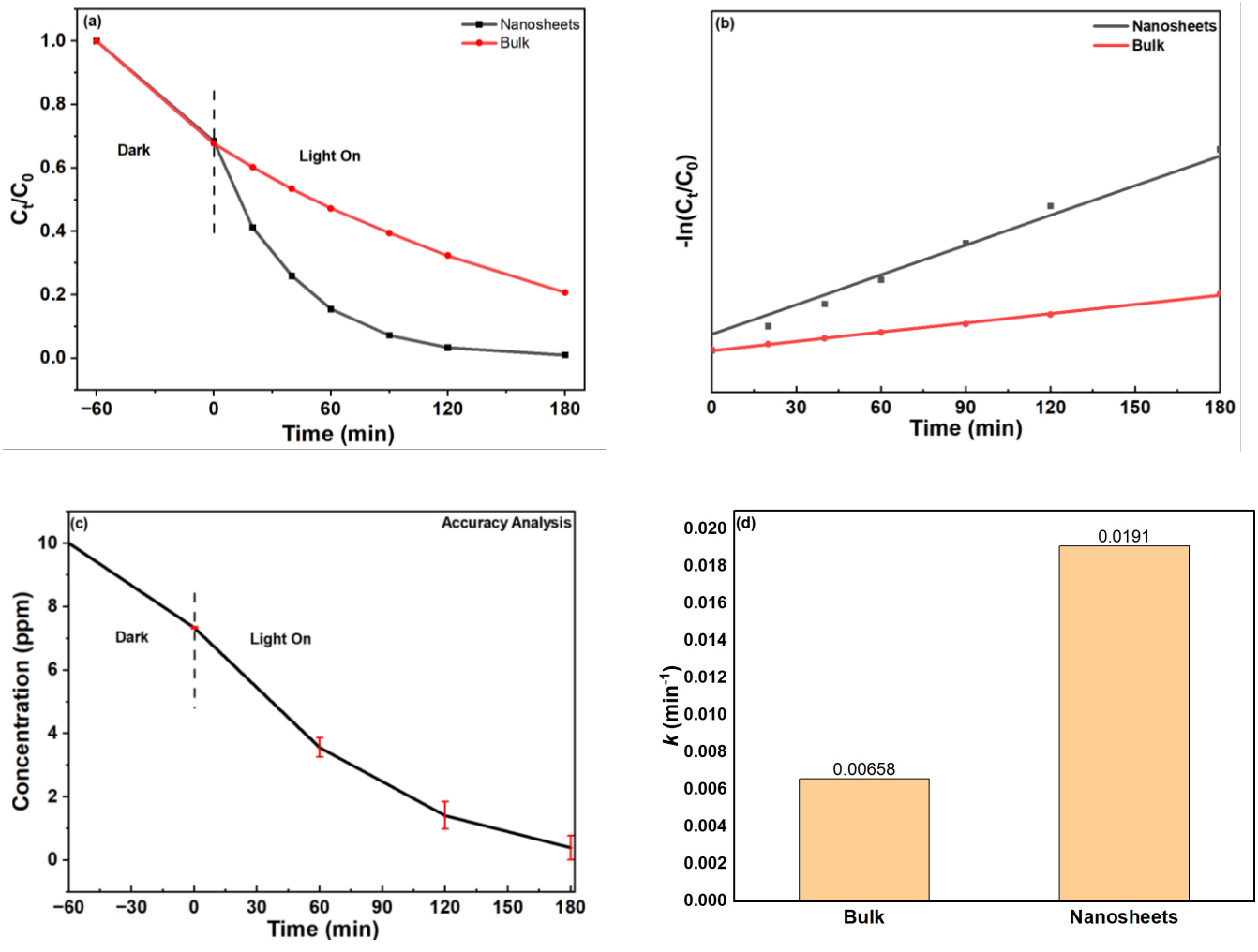

Figure 3.8 Photocatalytic degradation of NTP under visible light (a) first-order reaction kinetics of NTP degradation (b) Accuracy analysis of NTP degradation using g-C_3N_4 nanosheets(c) reaction rate constant of bulk and nanosheets(d)

3.3.8 Effect of pH

pH is the most essential factor that we must study because pH can alter the surface charge and affect the reaction between photocatalysts and NTP. Photocatalytic degradation of nitenpyram was carried out at different pH (2.5, 6.0, 9.0, 11.0) values to study the influence of pH. The pH values were adjusted using HCL and NaOH solution. The natural pH value of 10ppm NTP in 50ml water is 6.0.

Fig. 3.9(a) illustrates the photocatalytic degradation efficiency of NTP under different pH values. Results in Fig 3.9 (a) demonstrate that g-C_3N_4 can degrade NTP more efficiently under basic conditions, achieving degradation efficiencies of 89.2% at pH 2.5, 80.8% at pH 6.0, 99.0% at pH 9.0, and 89.6% at pH 11.0. The degradation efficiency is the highest under pH 9. It is known that the concentration of hydroxyl groups (OH^-) in the reaction system increases when the solution pH goes up, leading to the generation of a higher quantity of hydroxyl free radicals (·OH). The hydroxyl group (·OH) directly contributes to the degradation of NTP, resulting in enhanced photodegradation of NTP at higher pH levels. Nonetheless, excessive concentration of hydroxyl radical at pH 11 results in scavenging of photogenerated sites that lowers the NTP degradation.

The reaction kinetics were studied using the first-order kinetic equation (3-4), and the reaction rate constant is shown in Figure 3.9(b), which indicates that the reaction rate is low in acidic conditions and high in base conditions. The reaction rate appeared to be highest at pH 9, but at pH 11, it starts decreasing again this is because excessive generation of hydroxyl radical although hydroxyl radical is favourable for degradation but excessive concentration of hydroxyl radical will result in scavenging of photogenerated sites reducing the generation of (·OH) radical.

$$ln\frac{Ct}{C0} = -kt \qquad (3\text{-}4)$$

Where k is the reaction rate constant.

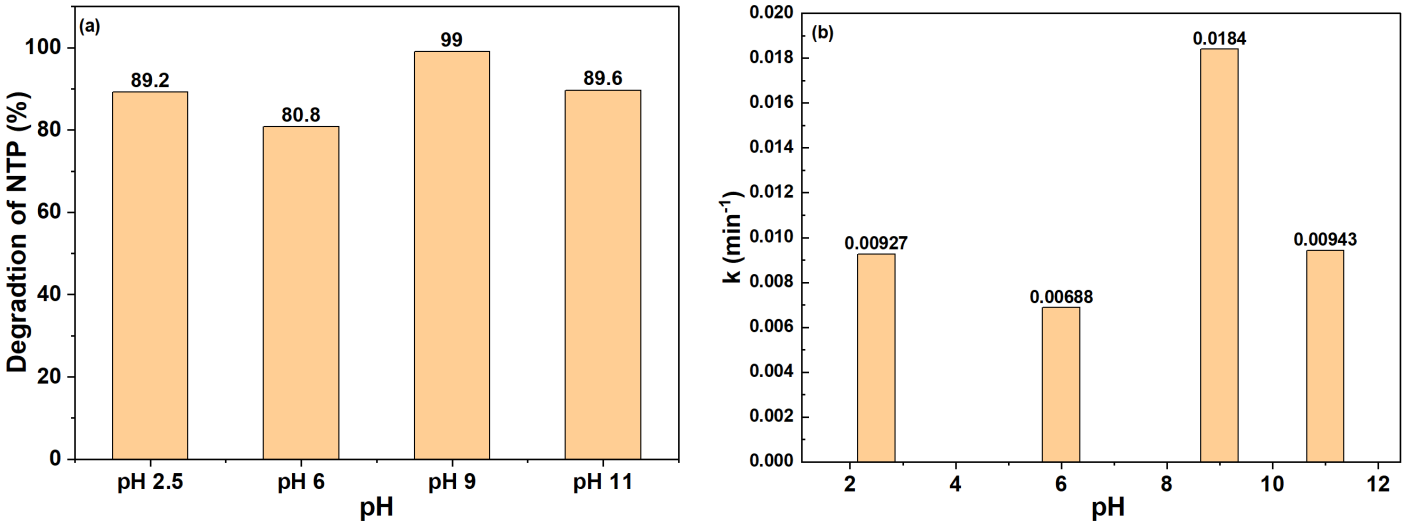

Figure 3.9 Effect of pH on NTP degradation(a), and NTP degradation rates under different pH(b)

3.3.9 Effect of Temperature

The influence of temperature on the photocatalytic performance of g-C_3N_4 nanosheets was also studied, and the results can be seen in Fig. 3.10. With a catalyst dosage of 1g/L, NTP solution at pH 9, the reaction was run at three different temperatures (30°C, 40°C, 50°C). As shown in Fig. 3.10, the degradation efficiency increases with the increase in temperature. This is because of the increase in the diffusion rate of the reaction. With the increase in temperature, the diffusion rate also increases. However, with the temperature rise, the energy cost also increases, so the temperature was set at 30°C, the optimal temperature with minimum cost.

The influence of temperature on the reaction kinetics is studied using the first-order kinetic equation (3-4), and the results are shown in Figure 3.10(c), which indicates that the reaction rate increases with the increase in temperature.

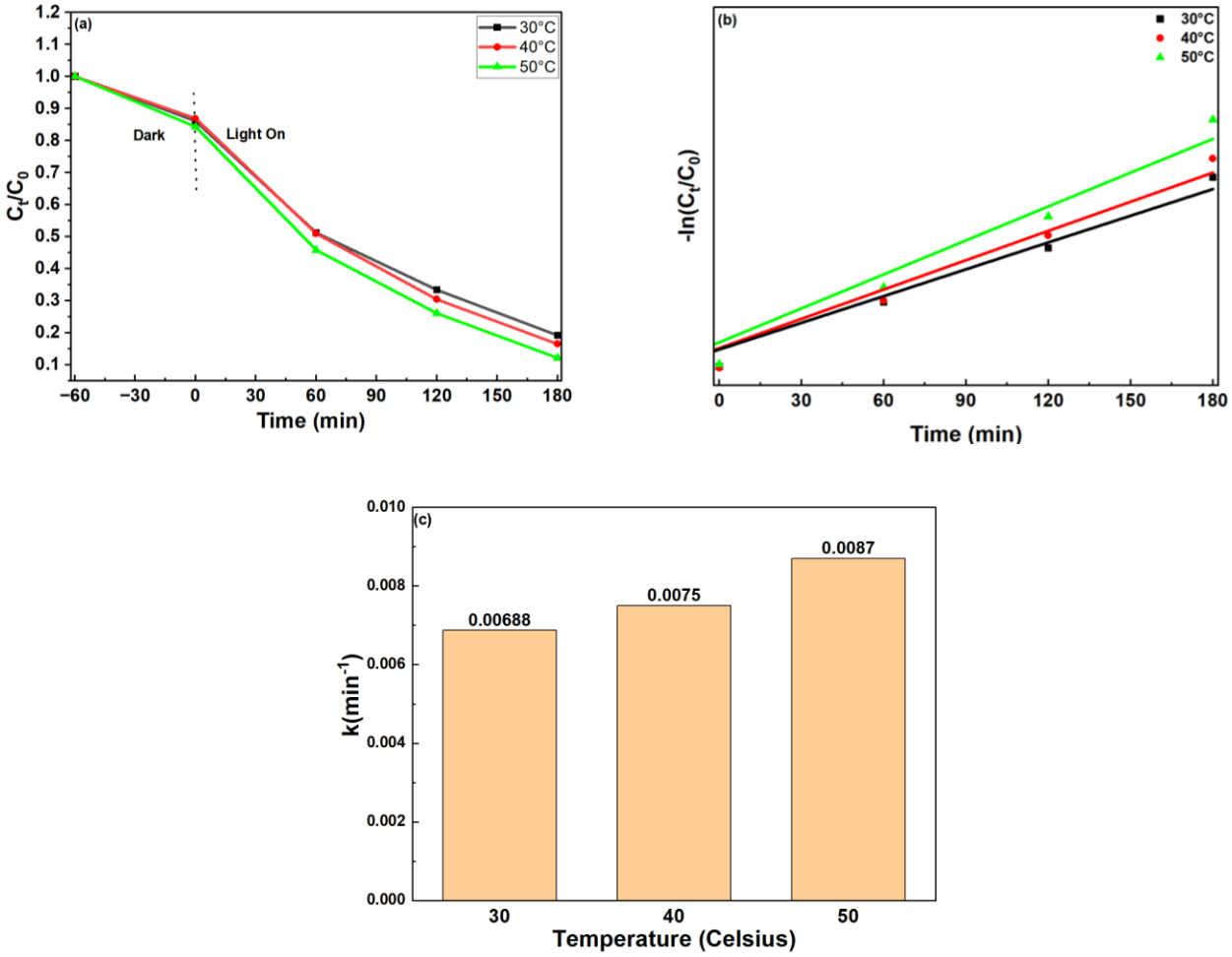

Figure 3.10 Effect of temperature on NTP degradation(a), first-order reaction kinetics of NTP at different temperatures(b), and rate constants of NTP degradation at different temperatures(c)

3.3.10 Degradation Pathways of NTP

The photocatalytic reaction was to degrade nitenpyram using g-C_3N_4 nanosheets under visible light. The reaction time was 4 hours, the catalyst dosage was 1g/L, pH 9, the reaction temperature was 30°C, and the reaction volume was 100 ml. 1 ml of samples was taken out at each sampling time, and the samples were analyzed using mass spectroscopy. At first, before the start of the reaction, it shows a prominent peak with m/z values of 271.09, which is like the molecular weight of nitenpyram. When the reaction started, the peak for m/z value 271.09 started decreasing, and two new peaks started coming out around retention time 6 and 13 minutes with an m/z value 100

and 212, respectively, which indicates that the nitenpyram was degraded into its metabolites with m/z value of 212, and 100. From Figure 3.11, nitenpyram can undergo different degradation pathways, the figure shows a product with an m/z value of 210, indicating $[C_{10}H_{13}ClN_3]^+$. This is because of the oxidation of C9/C11 olefins, a nitenpyram metabolite called CPMF. CPMF is further degraded into CPF, which shows an m/z value of 104[25,26]. CPF is less toxic as compared to NTP because it lacks the ability to directly effect nicotinic receptors of mammals.

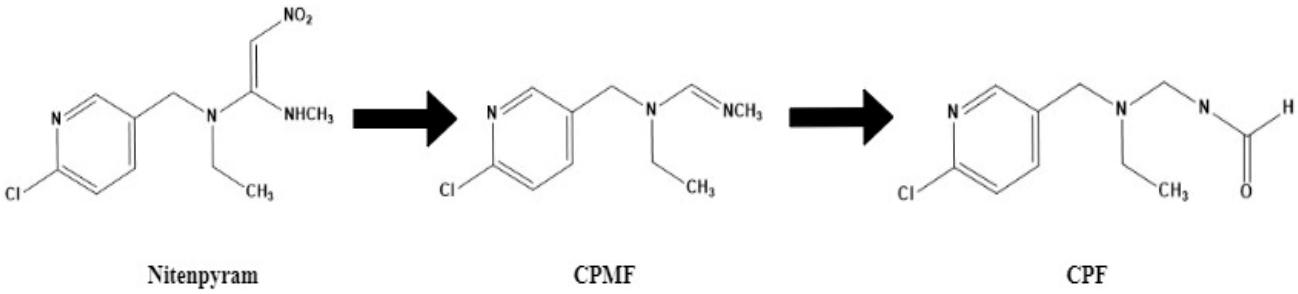

Figure 3.11 Degradation of nitenpyram into its metabolites

3.4 Conclusion

In this study, modified g-C_3N_4 was used to degrade nitenpyram from water. The prepared catalyst was characterized using XRD, FTIR, XPS, UV-DRS, BET and TEM. The catalyst shows a narrower band gap and increased surface area, providing more active sites for the reaction and enhancing its photocatalytic ability to degrade nitenpyram. The effect of pH and temperature was studied, showing that pH 9 and temperature 30°C are the optimized conditions for degrading NTP. The experimental results show that the prepared exfoliated nanosheets give 99% degradation of NTP with an initial concentration of 10 mgL^{-1}, pH 9, temperature 30°C, and catalyst dosage of 1g/L, whereas bulk g-C_3N_4 gives us only 79% degradation efficiency. These results indicate that the exfoliated nanosheets are better at degrading the pollutant as compared to the bulk one due to its increased surface area and narrower band gap. Further analysis using HPLC MS indicates the successful degradation of NTP into its metabolites, CPMF and CPF.

References

[1] V.P. Kalyabina, E.N. Esimbekova, K.V. Kopylova, V.A. Kratasyuk, Pesticides: formulants, distribution pathways and effects on human health – a review, Toxicol. Rep. 8 (2021) 1179–1192. https://doi.org/10.1016/j.toxrep.2021.06.004.

[2] K. Yin, Y. Deng, C. Liu, Q. He, Y. Wei, S. Chen, T. Liu, S. Luo, Kinetics, pathways and toxicity evaluation of neonicotinoid insecticides degradation via UV/chlorine process, Chem. Eng. J. 346 (2018) 298–306. https://doi.org/10.1016/j.cej.2018.03.168.

[3] S.A. Todey, A.M. Fallon, W.A. Arnold, Neonicotinoid insecticide hydrolysis and photolysis: Rates and residual toxicity, Environ. Toxicol. Chem. 37 (2018) 2797–2809. https://doi.org/10.1002/etc.4256.

[4] P. Jeschke, R. Nauen, M. Schindler, A. Elbert, Overview of the Status and Global Strategy for Neonicotinoids, J. Agric. Food Chem. 59 (2011) 2897–2908. https://doi.org/10.1021/jf101303g.

[5] M.L. Hladik, A.R. Main, D. Goulson, Environmental Risks and Challenges Associated with Neonicotinoid Insecticides, Environ. Sci. Technol. 52 (2018) 3329–3335. https://doi.org/10.1021/acs.est.7b06388.

[6] T. Blacquière, G. Smagghe, C.A.M. Van Gestel, V. Mommaerts, Neonicotinoids in bees: a review on concentrations, side-effects and risk assessment, Ecotoxicology 21 (2012) 973–992. https://doi.org/10.1007/s10646-012-0863-x.

[7] S.C. Wood, I.V. Kozii, R.V. Koziy, T. Epp, E. Simko, Comparative chronic toxicity of three neonicotinoids on New Zealand packaged honey bees, PLOS ONE 13 (2018) e0190517. https://doi.org/10.1371/journal.pone.0190517.

[8] J.E. Cresswell, N. Desneux, D. vanEngelsdorp, Dietary traces of neonicotinoid pesticides as a cause of population declines in honey bees: an evaluation by Hill's epidemiological criteria, Pest Manag. Sci. 68 (2012) 819–827. https://doi.org/10.1002/ps.3290.

[9] J.C.O. Rumkee, M.A. Becher, P. Thorbek, J.L. Osborne, Modeling Effects of Honeybee Behaviors on the Distribution of Pesticide in Nectar within a Hive and Resultant in-Hive

Exposure, Environ. Sci. Technol. 51 (2017) 6908–6917. https://doi.org/10.1021/acs.est.6b04206.

[10] L. Yang, Y.-L. Zhao, C.-Y. Zhao, H.-H. Li, M.-J. Wang, S.L. Morris-Natschke, K. Qian, K.-H. Lee, Y.-Q. Liu, Design, synthesis, crystal structure, bioactivity, and molecular docking studies of novel sulfonylamidine-derived neonicotinoid analogs, Med. Chem. Res. 23 (2014) 5043–5057. https://doi.org/10.1007/s00044-014-1046-5.

[11] M. Tang, Y. Ao, C. Wang, P. Wang, Facile synthesis of dual Z-scheme g-C_3N_4/Ag_3PO_4/AgI composite photocatalysts with enhanced performance for the degradation of a typical neonicotinoid pesticide, Appl. Catal. B Environ. 268 (2020) 118395. https://doi.org/10.1016/j.apcatb.2019.118395.

[12] S. Li, W. Wang, X. Zeng, X. Ma, Electro-catalytic degradation mechanism of nitenpyram in synthetic wastewater using Ti-based SnO_2–Sb with rare earth-doped anode, Desalination Water Treat. 54 (2015) 1925–1938. https://doi.org/10.1080/19443994.2014.899514.

[13] S. Zhou, Y. Wang, K. Zhou, D. Ba, Y. Ao, P. Wang, In-situ construction of Z-scheme g-C_3N_4/WO_3 composite with enhanced visible-light responsive performance for nitenpyram degradation, Chin. Chem. Lett. 32 (2021) 2179–2182. https://doi.org/10.1016/j.cclet.2020.12.002.

[14] C. Sun, J. Jin, J. Zhu, H. Wang, D. Yang, J. Xing, Discovery of bis-aromatic ring neonicotinoid analogues fixed as cis-configuration: Synthesis, insecticidal activities, and molecular docking studies, Bioorg. Med. Chem. Lett. 20 (2010) 3301–3305. https://doi.org/10.1016/j.bmcl.2010.04.050.

[15] A. Elbert, M. Haas, B. Springer, W. Thielert, R. Nauen, Applied aspects of neonicotinoid uses in crop protection, Pest Manag. Sci. 64 (2008) 1099–1105. https://doi.org/10.1002/ps.1616.

[16] J.E. Casida, Neonicotinoids and Other Insect Nicotinic Receptor Competitive Modulators: Progress and Prospects, Annu. Rev. Entomol. 63 (2018) 125–144. https://doi.org/10.1146/annurev-ento-020117-043042.

[17] A. Alaghmandfard, K. Ghandi, A Comprehensive Review of Graphitic Carbon Nitride (g-C_3N_4)–Metal Oxide-Based Nanocomposites: Potential for Photocatalysis and Sensing, Nanomaterials 12 (2022) 294. https://doi.org/10.3390/nano12020294.

[18] J. Pei, H. Li, S. Zhuang, D. Zhang, D. Yu, Recent Advances in g-C3N4 Photocatalysts: A Review of Reaction Parameters, Structure Design and Exfoliation Methods, Catalysts 13 (2023) 1402. https://doi.org/10.3390/catal13111402.

[19] Y. Wang, Y. Deng, D. Gong, L. Yang, L. Li, Z. Zhou, S. Xiong, R. Tang, J. Zheng, Visible light excited graphitic carbon nitride for efficient degradation of thiamethoxam: Removal efficiency, factors effect and reaction mechanism study, J. Environ. Chem. Eng. 9 (2021) 105739. https://doi.org/10.1016/j.jece.2021.105739.

[20] J. Ran, T.Y. Ma, G. Gao, X.-W. Du, S.Z. Qiao, Porous P-doped graphitic carbon nitride nanosheets for synergistically enhanced visible-light photocatalytic H $_2$ production, Energy Environ. Sci. 8 (2015) 3708–3717. https://doi.org/10.1039/C5EE02650D.

[21] X. Yuan, C. Zhou, Y. Jin, Q. Jing, Y. Yang, X. Shen, Q. Tang, Y. Mu, A.-K. Du, Facile synthesis of 3D porous thermally exfoliated g-C_3N_4 nanosheet with enhanced photocatalytic degradation of organic dye, J. Colloid Interface Sci. 468 (2016) 211–219. https://doi.org/10.1016/j.jcis.2016.01.048.

[22] L. Huang, H. Xu, Y. Li, H. Li, X. Cheng, J. Xia, Y. Xu, G. Cai, Visible-light-induced WO_3/g-C_3N_4 composites with enhanced photocatalytic activity, Dalton Trans. 42 (2013) 8606. https://doi.org/10.1039/c3dt00115f.

[23] P. Makuła, M. Pacia, W. Macyk, How To Correctly Determine the Band Gap Energy of Modified Semiconductor Photocatalysts Based on UV–Vis Spectra, J. Phys. Chem. Lett. 9 (2018) 6814–6817. https://doi.org/10.1021/acs.jpclett.8b02892.

[24] S. Chen, Y. Hu, S. Meng, X. Fu, Study on the separation mechanisms of photogenerated electrons and holes for composite photocatalysts g-C_3N_4-WO_3, Appl. Catal. B Environ. 150–151 (2014) 564–573. https://doi.org/10.1016/j.apcatb.2013.12.053.

[25] M. Noestheden, S. Roberts, C. Hao, Nitenpyram degradation in finished drinking water, Rapid Commun. Mass Spectrom. 30 (2016) 1653–1661. https://doi.org/10.1002/rcm.7581.

[26] Md.T.B. Salam, K. Ito, R. Kataoka, Biodegradation of nitenpyram (neonicotinoid insecticide) by endophytic bacterium, *Bacillus thuringiensis* strain NIT-2, isolated from neonicotinoid-treated plant samples, J. Pestic. Sci. 49 (2024) 94–103. https://doi.org/10.1584/jpestics.D24-002.

Chapter 4. Simultaneous Photocatalytic Degradation of Nitenpyram and Reduction of Cr (VI) using g-C_3N_4/WO_3 under Visible Light Irradiation

4.1 Introduction

The integration of a photoinduced reductive half-reaction with a corresponding oxidative half-reaction for dual-functional photocatalysis has garnered increasing interest [1]. Typically, dual-functional photocatalysis serves to accomplish two objectives, such as concurrent H2 production and the oxidation of organic pollutants, or the reduction of heavy metals alongside the degradation of organic pollutants [1,2]. Solar-driven dual-functional photocatalysis necessitates a photocatalyst capable of concurrently facilitating both types of reactions; thus, a dual-functional photocatalyst must exhibit narrow band gaps, effective charge-carrier separation, and higher positive valence band and negative conduction band potentials [3,4]. Such requirements can not be met by single-phase/component photocatalysts. Constructing multiphase or multicomponent heterojunctions is essential for dual-functional photocatalysis.

Heterojunctions combining graphitic carbon nitride (g-C_3N_4) with metal oxides such as TiO_2, ZnO, Bi_2O_3, and WO_3 have garnered significant interest as dual-functional photocatalysts [5-7]. A range of g-C_3N_4/metal oxide (g-C_3N_4/MO) heterojunctions has been fabricated for the simultaneous generation of hydrogen (H_2) and the oxidation (degradation) of organic pollutants. Photocatalytic water splitting is characterized by two distinct half reactions: the reduction of protons (H^+) to form hydrogen (H_2) and the oxidation of water to yield oxygen (O_2). In contrast to the half-reaction of water oxidation, the oxidative transformation of organic water contaminants typically requires less energy. This characteristic enhances the efficiency of coupling oxidative organic transformation with reductive H_2 generation. A Z-scheme CeO_2/g-C_3N_4 heterojunction was recently developed

for the concurrent photocatalytic evolution of H_2 and degradation of bisphenol A (BPA) under visible-light irradiation [8]. The heterojunction exhibited superior photocatalytic performance compared to CeO_2 and g-C_3N_4 nanosheets, achieving an H_2 production rate of 1240.9 μmol g^{-1} h^{-1}, approximately 5.2 times greater than that of pure CeO_2 under identical reaction conditions. Meanwhile, the g-C_3N_4/CeO_2 heterojunction demonstrated the ability to oxidize 94.1% of BPA (c_0=10.0 mg L^{-1}) within 2.5 hours of visible light exposure, achieving efficiencies 4.2 and 6.8 times greater than those of pure CeO_2 and g-C_3N_4, respectively. The enhanced photocatalytic activity of the heterojunction was ascribed to the increased adsorption of organic pollutants and the efficient separation of photogenerated carriers at the interface of CeO_2 and g-C_3N_4. In another study, a novel $W_{18}O_{49}$/C@g-C_3N_4 S-scheme heterojunction was prepared through electrospinning and vapor deposition methods for enhanced photocatalytic H_2 evolution and degradation of rhodamine B (RhB) [9]. The efficiencies of synchronous H_2 evolution and RhB degradation over $W_{18}O_{49}$/C@g-C_3N_4 nanofibers were approximately 5.60 and 3.51 times higher than those of $W_{18}O_{49}$/C, and 2.45 and 22.55 times higher than those of C@g-C_3N_4 nanofibers, respectively.

The photocatalytic reduction of CO_2 into hydrocarbon fuels (CH_3OH, C_2H_5OH, and CH_4) represents a compelling technological advancement that addresses both the challenges of global warming and the demand for energy supply in a cohesive manner. Given the pronounced reduction capability of g-C_3N_4, g-C_3N_4/MO heterojunctions have been utilized for the dual function of photocatalytic reduction of CO_2 in conjunction with the degradation of organic pollutants. A heterojunction comprising Cu/Cu_2O decorated g-C_3N_4 was engineered for the concurrent reduction of CO_2 and the oxidative coupling of benzylamines [10].

Following 16 hours of exposure to visible light, the optimized Cu/Cu_2O@g-C_3N_4 heterojunction demonstrated the capability to synthesize N-benzylidene benzylamine through the oxidation of

benzylamine and to produce methanol from the reduction of CO_2, achieving rates of 5451 μmol g^{-1} and 437 μmol g^{-1}, respectively. A heterojunction comprising a mixed metal oxide and g-C_3N_4, specifically, $CdMoO_4$/g-C_3N_4, was constructed for the simultaneous photocatalytic degradation of RhB and reduction of CO_2 [11]. The formation of a heterojunction structure between $CdMoO_4$ and g-C_3N_4 markedly improved the separation of electron–hole pairs and increased photocatalytic activity. The $CdMoO_4$/g-C_3N_4 heterojunction demonstrated a degradation rate of RhB that is 6.5 times greater than that of pure g-C_3N_4 when exposed to visible light irradiation. The composite exhibited a CO_2 conversion rate of 25.8 mold $h^{-1}g^{-1}$, representing a 4.8-fold increase compared to the pristine g-C_3N_4.

The utilization of g-C_3N_4/MO heterojunctions for the concurrent photocatalytic degradation of a pollutant combination has also been reported [6,12,13]. The simultaneous detoxification of a mixture of organic contaminants and heavy metal ions has emerged as a critical concern due to their simultaneous presence in industrial effluent. Chromium (Cr) frequently coexists with 2,4-dichlorophenol (2,4-DCP), 2,4-dichlorophenoxyacetic acid (2,4-D), and antibiotics. To concurrently eliminate them, the oxidation of 2,4-D and the reduction of Cr (VI) were performed using a Z-scheme Co_9O_8/g-C_3N_4 heterojunction [13]. The concurrent consumptions of electrons by Cr (VI) and holes by 2,4-D inhibited charge carrier recombination, significantly enhancing photocatalytic performance relative to a single pollutant system. Jiang et al. developed a solar-driven g-C_3N_4/TiO_2 heterojunction to facilitate the simultaneous photocatalytic reduction of U (VI) and oxidation of As (III) [14]. Experimental results demonstrated the formation of a Type II heterojunction between g-C_3N_4 and TiO_2, achieving conversion rates of 82.66% for U (VI) reduction and 41.18% for As (III) oxidation, with initial concentrations of both metal ions set at 20 mg L^{-1}. Two factors contributed to the achievement of a relatively lower conversion rate of As

(III). Initially, the oxidation of As (III) occurred on the valence band (VB) of g-C_3N_4, which possesses a lower oxidation capability compared to other semiconductors. Secondly, the reduction of U(VI) and the oxidation of As (III) both utilized photogenerated electrons, leading to competition between these two photocatalytic processes.

Despite considerable studies on dual-functional photocatalysis targeted at eliminating a variety of water pollutants, the optimal structural design of g-C_3N_4/MO heterojunctions to inhibit the recombination of photogenerated e^-/h^+ and to prevent the misalignment of band energy between g-C_3N_4 and the MO remains a significant challenge. Increased research endeavors need to be directed towards elucidating the structure-function relationship of g-C_3N_4/metal oxide heterojunctions to improve the photocatalytic activity and stability of the binary photocatalyst. Moreover, it is crucial to optimize the operating conditions (such as temperature, solution pH, reactant concentration, catalyst dosage, etc.) to achieve elevated conversion rates for both half-reactions, given that the optimal conditions for reduction reactions generally differ from those required for oxidation reactions

In this study, we aim to design and fabricate novel g-C_3N_4/WO_3 heterojunction for the simultaneous photocatalytic reduction of Cr (VI) and oxidation of NTP. WO_3 is selected because of its high oxidation ability and positive valance band position which will give us a well balanced band structure for dual photocatalysis. The research investigation will be mainly focused on optimizing the properties (favorable bandgap and band edge positions, prolonged carrier lifetime, short carrier pathway to the surface, etc.) and photocatalytic activity of the heterojunction. The photocatalytic activity of the heterojunctions will be assessed and optimized based on their performance and efficiency in the conversion of Cr (VI) and NTP.

4.2 Materials and Methods

4.2.1 Materials

Melamine (99%), sodium tungstate dihydrate (99%), sodium dichromate dihydrate ($Na_2Cr_2O_7 \cdot 2H_2O$, 99.5%), isopropanol (99.9%), triethanolamine (99%), and ACS grade sulfuric acid, phosphoric acid, oxalic acid, and sodium hydroxide were purchased from Fisher Scientific. ACS grade diphenyl carbazide (DPC), nitenpyram (≥98%), and *p*-benzoquinone (≥98%) were obtained from Sigma-Alderich. All these chemicals were used as received, without further purification. HPLC-grade acetonitrile and water were purchased from Fisher Scientific.

4.2.2 Synthesis of the g-C_3N_4/WO_3 heterojunction

Melamine was used as a precursor for the synthesis of g-C_3N_4 by a two-step calcination procedure [15-17]. Initially, 5.0 g of melamine was placed in a covered crucible and heated to 520 ℃ for 4 h at a ramp rate of 2.5 ℃ min^{-1} in a muffled furnace. The substance was cooled to room temperature and ground into powder using a mortar. In the second phase, the powder was placed in an uncovered crucible and heated at 520 ℃ for 4 h with a ramp rate of 2.5 ℃ min^{-1} in a muffle furnace. The light-yellow g-C_3N_4 nanosheets were then acquired.

WO_3 was synthesized via a hydrothermal process [18]. 5.0 g of sodium tungstate was solubilized in 100.0 mL of water. 12.0 M HCl was introduced during stirring, resulting in a yellow solution. Subsequently, 1.0 g of oxalic acid was added follows by constant agitation for 1 h. The solution was transferred to an autoclave and subjected to an oven temperature of 150 ℃ for a duration of 10 h. After cooling, the product was rinsed with deionized water. The product was ultimately placed in a crucible, calcined for 4 h at 320 ℃, and thereafter crushed into powder.

The g-C_3N_4/WO_3 heterojunction was prepared by dispersing g-C_3N_4 and WO_3 in deionized water at a mass ratio of 5:1. The mixture was ultrasonicated for 20 minutes, to evenly distribute the nanoparticles, dried overnight at 60°C, and finally ground into a powder.

4.2.3 Characterization

The g-C_3N_4/WO_3 heterojunction was characterized using X-ray photoelectron spectroscopy (XPS, PHI 5000 VPIII, ULVAC-PHI, Japan) and Fourier transform infrared (FTIR, Tensor II, Bruker, Germany) spectroscopy throughout a spectrum of 400 to 4000 cm^{-1}. Powder X-ray diffraction (XRD) was employed to assess the crystallinity of the synthesized photocatalyst. An ultraviolet diffuse reflectance spectrophotometer (UV-DRS) was employed to ascertain the reflectance spectrum and the UV-visible absorption of the synthesized photocatalyst. The valence-band position of the g-C_3N_4/WO_3 heterojunction was assessed by valence-band XPS.

4.2.4 Dual-functional photocatalytic degradation of NTP and reduction of Cr (VI)

The photocatalytic efficacy of the g-C_3N_4/WO_3 heterojunction was examined by experimental studies in a jacketed batch reactor of 150 ml under visible light (300W Xenon lamp with a 420-nm cutoff filter) at a constant temperature. The temperature of photocatalytic reaction was controlled by a circulating water system (FP50-HL, Julabo, USA). The reaction involved the mixing of 50.0 mg of g-C_3N_4/WO_3 with 50.0 mL of Cr (VI)-NTP binary solution containing 20.0 mgL^{-1} Cr (VI) and 20.0 mg L^{-1} NTP. The initial pH of the binary solutions was adjusted to 3.0 with 1.0 M H_2SO_4 and NaOH solutions. The mixture was stirred in darkness for 1 h to reach adsorption equilibrium, after which the reaction was initiated by activating the light source. At each sampling time, 1.0 ml of the sample was withdrawn and filtered through a 0.22 µm syringe filter for subsequent analysis. To verify the repeatability of the dual-functional photocatalytic processes, three repeated experimental trials were conducted with an initial concentration of both

pollutants set at 20.0 mg L^{-1}, a pH of 3.0, and a catalyst dosage of 1.0 g L^{-1}. The mean experimental error was within ±5.0%, indicating excellent experimental repeatability.

Three scavengers were employed in binary degradation to ascertain the active radical species. Triethanolamine (TEOA), benzoquinone (BQ), and isopropyl alcohol (IPA) were utilized as scavengers to capture holes (h^+), superoxide radical ($O_2^{\bullet-}$) and hydroxyl radical (•OH), respectively. During experiments, a specific type of radical scavenger was introduced to the reaction suspension, while all other conditions were maintained consistently (pH=3, *T*= 30 ºC, photocatalyst dosage at 1.0 g L^{-1}).

4.3.5 Concentration determination of NTP and Cr (VI)

The concentration of NTP was determined using an Agilent HPLC-MS system with a DAD detector at a wavelength of 270 nm. The C18 column was used with a mobile phase of water and acetonitrile at a 80:20 (v/v) ratio. The flow rate was fixed at 0.6ml/L, and the column temperature was kept at 30°C.

The concentration of Cr (VI) was determined via a diphenylcarbazide (DPC) colorimetric method. The detailed steps are as follows: 2.0 ml of distilled water was added to 0.5 ml of the sample. Then, 50 µL H_2SO_4 and 50 µL of H_3PO_4 were added to the mixture and mixed entirely. Subsequently, 200 µL of freshly made DPC solution was added to the mixture and allowed to sit for full-color development. The Cr (VI) concentration was found by measuring the UV-vis absorbance at a wavelength of 540 nm with water as a reference.

4.3 Results and Discussions

4.3.1 Characterization results

The elemental composition of the g-C_3N_4/WO_3 heterojunction has been determined using XPS. Fig. 4.1a reveals the survey scan of the composite which mainly includes C, N, O, and W. The high-resolution C 1s XPS spectrum depicted in Fig. 4.1b can be deconvoluted into three peaks at 284.6, 287.9, and 289.4 eV, which correspond to C-C (reference carbon), N=C-N within the triazine ring, and the O-C=O functional group [19, 20]. Fig. 4.1c illustrates the high-resolution XPS spectrum of N 1s together with the deconvoluted peaks. The peaks at 398.3, 399.9 and 404.0 eV correspond to sp^2-bonded nitrogen (C=N-C) atoms, benzenoid amine (-NH-), and C-N bonds, respectively [21]. Two characteristic peaks at 35.2 and 37.3 eV of XPS spectrum of W 4f (Fig. 4.1d) represent the $W4f_{7/2}$ and $w4f_{5/2}$ doublet of the highest oxidized states of tungsten ions in monoclinic WO_3 [22]. The XPS spectrum of O 1s as seen from Fig. 4.1e has been deconvoluted into two major peaks at 529.8 eV and 531.6 eV, which are ascribed to O^{2-} ions in WO_3 and organic C=O bond, respectively [22].

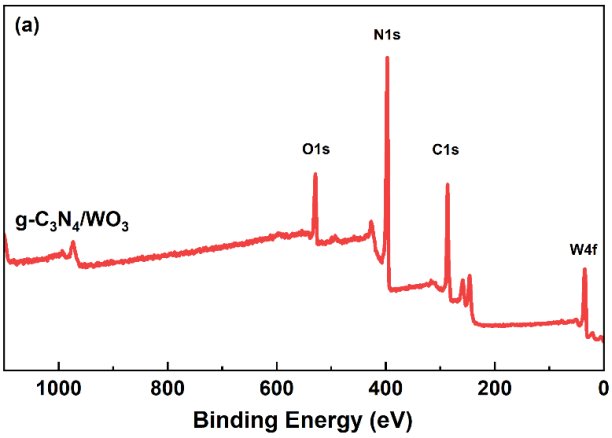
(a)
N1s
O1s
C1s
W4f
g-C3N4/WO3
1000
800
600
400
200
0
Binding Energy (eV)

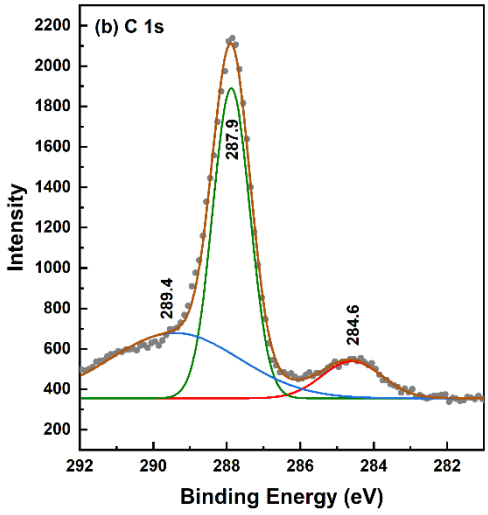
(b) C 1s
287.9
289.4
284.6
Intensity
Binding Energy (eV)

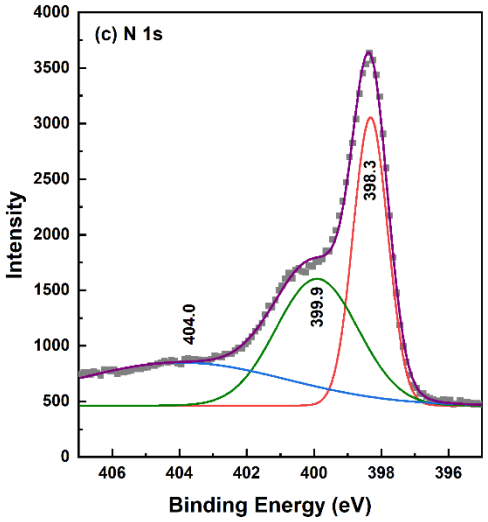
(c) N 1s
398.3
399.9
404.0
Intensity
Binding Energy (eV)

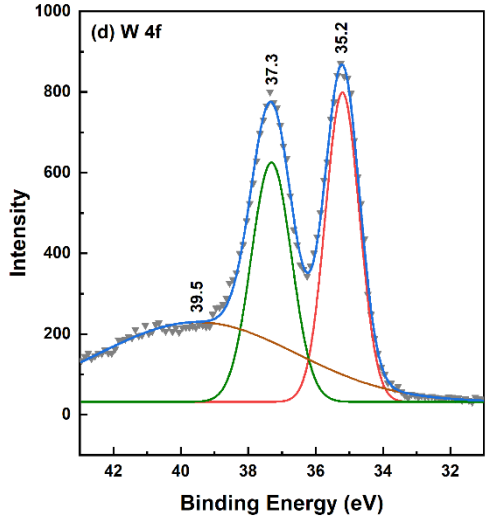
(d) W 4f
37.3
35.2
39.5
Intensity
Binding Energy (eV)

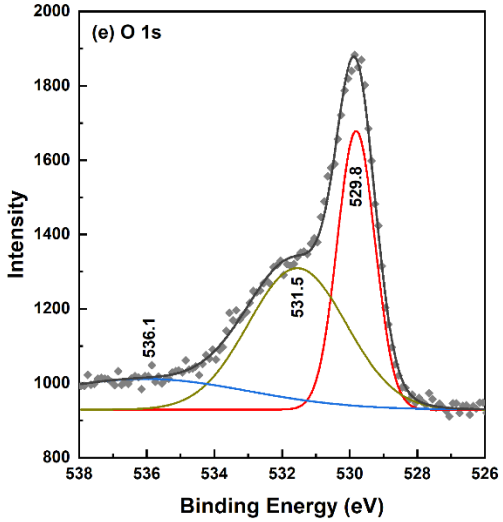
(e) O 1s
529.8
531.5
536.1
Intensity
Binding Energy (eV)

Figure 4.1 XPS Survey (a), C 1s (b), N 1s (c), W4f (d), and O 1s (e) of the g-C_3N_4/WO_3 heterojunction

The FT-IR spectrum of g-C_3N_4/WO_3, in conjunction with that of g-C_3N_4 nanosheets and WO_3, is presented in Fig. 4.2. The IR spectrum of WO_3 exhibits a large absorption band within the wavelength range of 500-950 cm^{-1}, associated with the stretching modes of W-O-W and O-W-O [19]. The peak at 802.2 cm^{-1} for g-C_3N_4 is ascribed to the bending vibration of heptazine rings, the peaks located at 1234.2 and 1317.1 cm^{-1} resulted from the vibration mode of C–N bond [23]. The bands of 1396.2, and 1539.9 cm^{-1} correspond to the vibration of C=N bond in aromatic heterocycles, peak at 1627.6 cm^{-1} is attributed to the stretching vibration of C=O bond [23]. The broad peak between 3000-3300 cm^{-1} indicates the N-H or O-H bond stretching vibration from the uncondensed amino group [22]. Figure 4.2 illustrates that the IR absorption peaks of the g-C_3N_4/WO_3 heterojunction correspond to those of pure WO_3 and g-C_3N_4. The composite's peak intensity is enhanced at a wavelength of 802.2 cm^{-1} due to the convergence of absorption peaks from g-C_3N_4 and WO_3. The peak intensity within the wavelength range of 500-950 cm^{-1} is diminished due to the low concentration of WO_3 in the composite.

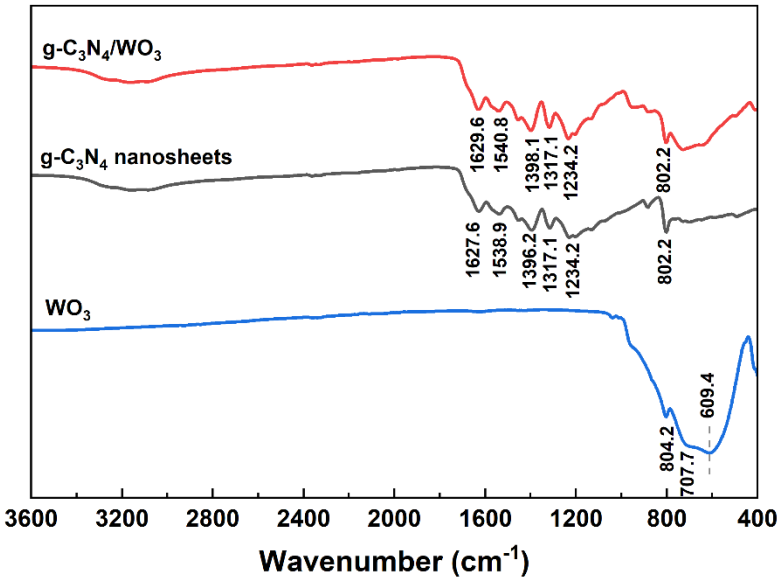

Figure 4.2 FTIR spectra of g-C_3N_4 nanosheet, WO_3 and g-C_3N_4/WO_3 heterojunction

The crystal structure and orientation of g-C_3N_4 nanosheets, WO_3, and the g-C_3N_4/WO_3 heterojunction have been analyzed via powder XRD. Fig. 4.3 illustrates the XRD patterns of g-C_3N_4, WO_3, and the g-C_3N_4/WO_3 heterojunction. Two distinctive diffraction peaks at 13.08 and 27.72°, corresponding to the (100) and (002) crystal planes of g-C_3N_4 nanosheets, are observed. The former is attributed to the interlayer repeating unit of tri-s-triazine, while the latter is assigned to an interplanar stacking ring of the conjugated aromatic ring [24]. Pure WO_3 exhibits diffraction peaks at 2θ values of 23.3, 23.7, 24.5, 28.9, 34.32, 47.2, 48.3, 50.5, 51.2, and 56°, corresponding to the (002), (200), (020), (112), (220), (020), (040), (140), (112), and (114) planes of its monoclinic crystal structure [22]. In the XRD pattern of the g-C_3N_4/WO_3 heterojunction, all distinguishable peaks correspond to the monoclinic WO_3 phase and the exfoliation of g-C_3N_4.

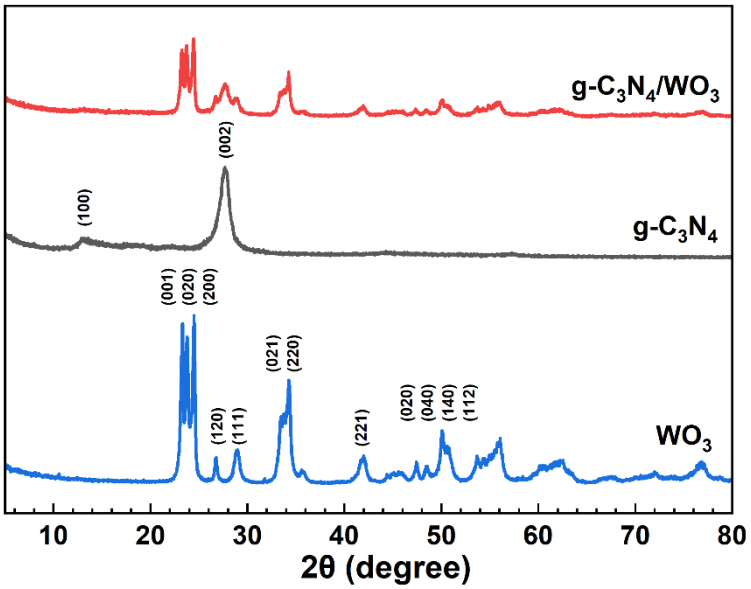

Figure 4.3 Powder XRD patterns of g-C_3N_4 nanosheet, WO_3 and g-C_3N_4/WO_3 heterojunction

4.3.2 Optical properties of the g-C_3N_4/WO_3 heterojunction

Optical absorptions of pure g-C_3N_4 nanosheets, WO_3, and the g-C_3N_4/WO_3 heterojunction have been analyzed using UV-vis diffuse reflectance spectra. As seen in Fig. 4.4a, all samples demonstrated absorption in the visible light region. The absorption edges of g-C_3N_4 and WO_3 are 480 nm and 473 nm, respectively, whereas the absorption edge of the g-C_3N_4/WO_3 heterojunction is approximately 476 nm. The g-C_3N_4 spectrum displays a faint absorption tail that extends nearly to 550 nm, attributable to defects within the g-C_3N_4 structure, as documented in other studies [25]. A comparable absorption tail is also evident in the spectra of the g-C_3N_4/WO_3 heterojunction, which further corroborates the establishment of a robust bond at the interface of g-C_3N_4 and WO_3.

The bandgap energy (E_g) of the three photocatalysts can be determined from the Tauc plot employing the methodology outlined in Chapter 3. Figure 4.4b illustrates that the band gap of the g-C_3N_4/WO_3 heterojunction is situated between that of pure g-C_3N_4 and WO_3. This outcome illustrates the formation of tightly chemically bonded interfaces between g-C_3N_4 and WO_3.

The positions of the valence bands (VB) for g-C_3N_4 nanosheets, and WO_3 have been determined through the analysis of the XPS valence band spectra, as illustrated in Fig. 4.5. The VB edge potentials (E_{VB}) of g-C_3N_4 and WO_3 are measured to be 1.9 eV (NHE) and 2.44 eV (NHE), respectively. The conduction band (CB) potentials of g-C_3N_4 (-0.76 eV *vs*. NHE) and WO_3 (-0.12 eV *vs*. NHE) are calculated correspondingly.

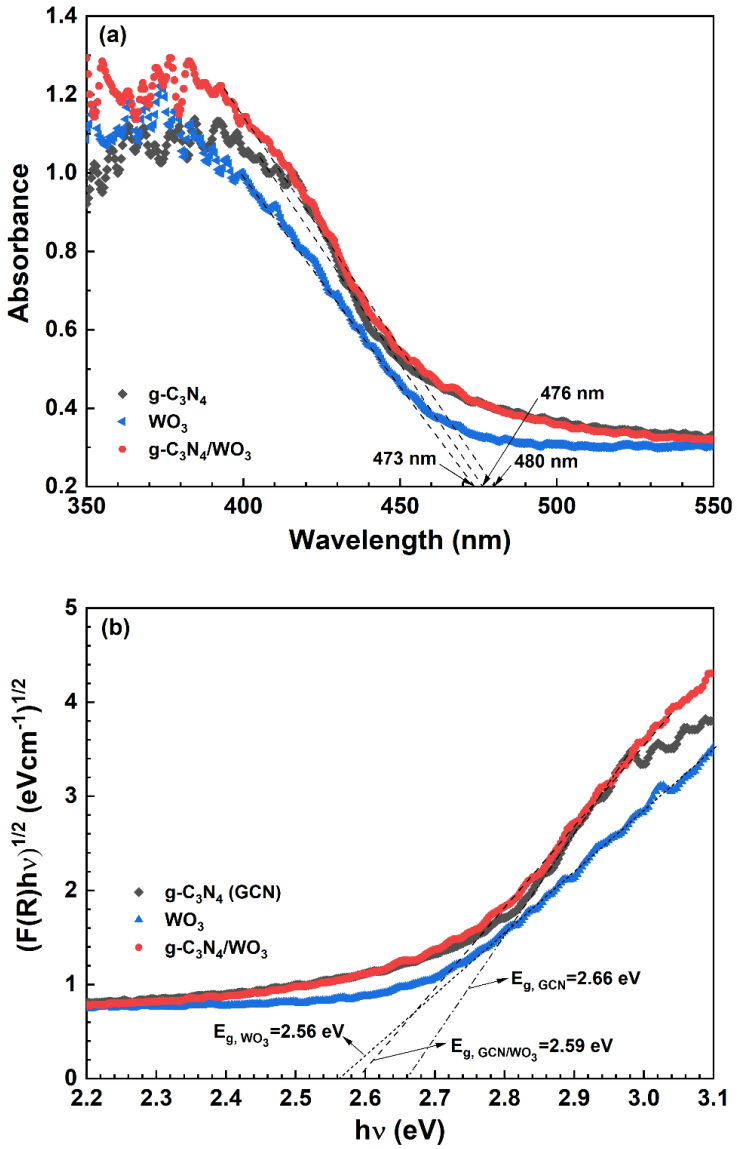

Figure 4.4 UV-Vis absorbance (a) and bandgap (b) of g-C_3N_4 nanosheets, WO_3 and g-C_3N_4/WO_3 heterojunction

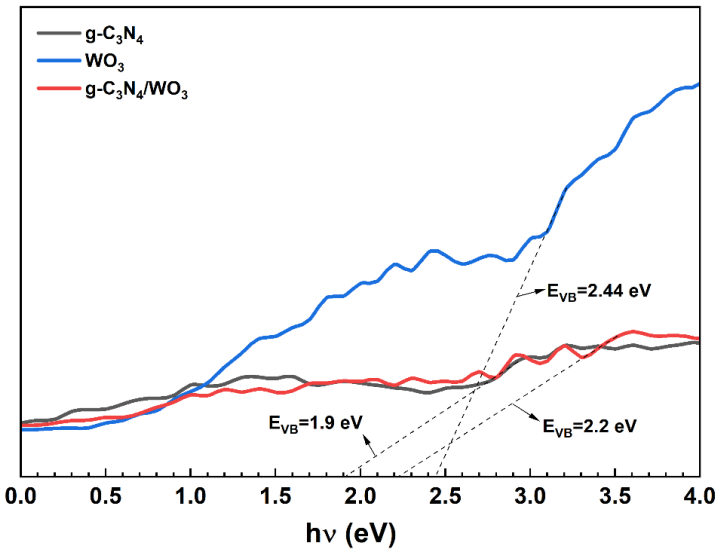

Figure 4.5 Valance band spectra of g-C_3N4, WO_3, and g-C_3N_4 /WO_3 heterojunction

4.3.3 Photocatalytic performance of the g-C_3N_4/WO_3 heterojunction

The photocatalytic performance of the g-C_3N_4/WO_3 heterojunction has been investigated for the concurrent photocatalytic reduction of Cr (VI) and degradation of NTP under visible light. Figs. 4.6a & d illustrate the temporal variation in the concentrations of NTP and Cr (VI) when subjected to three distinct photocatalysts (g-C_3N_4, WO_3 and the g-C_3N_4/WO_3 heterojunction) under identical reaction conditions. For NTP degradation, approximately 10.5%, 15.0%, and 8.2% of NTP was adsorbed or oxidized by C_3N_4, WO_3 and the g-C_3N_4/WO_3, respectively, after 1 hour in darkness. In contrast, 29.8%, 35.7%, and 33.4% of Cr (VI) was adsorbed or reduced by C_3N_4, WO_3 and the g-C_3N_4/WO_3, respectively, after the same duration in darkness. Following a 3-hour exposure to visible light, degradation rates of 76.2%, 67.8%, and 91.6% for NTP were observed, alongside reduction efficiencies of 71.3%, 76.7%, and 88.7% for Cr (VI) over g-C_3N_4, WO_3 and the g-C_3N_4/WO_3, respectively. The g-C_3N_4/WO_3 heterojunction exhibits a substantial improvement in photocatalytic activity compared to g-C_3N_4 and WO_3.

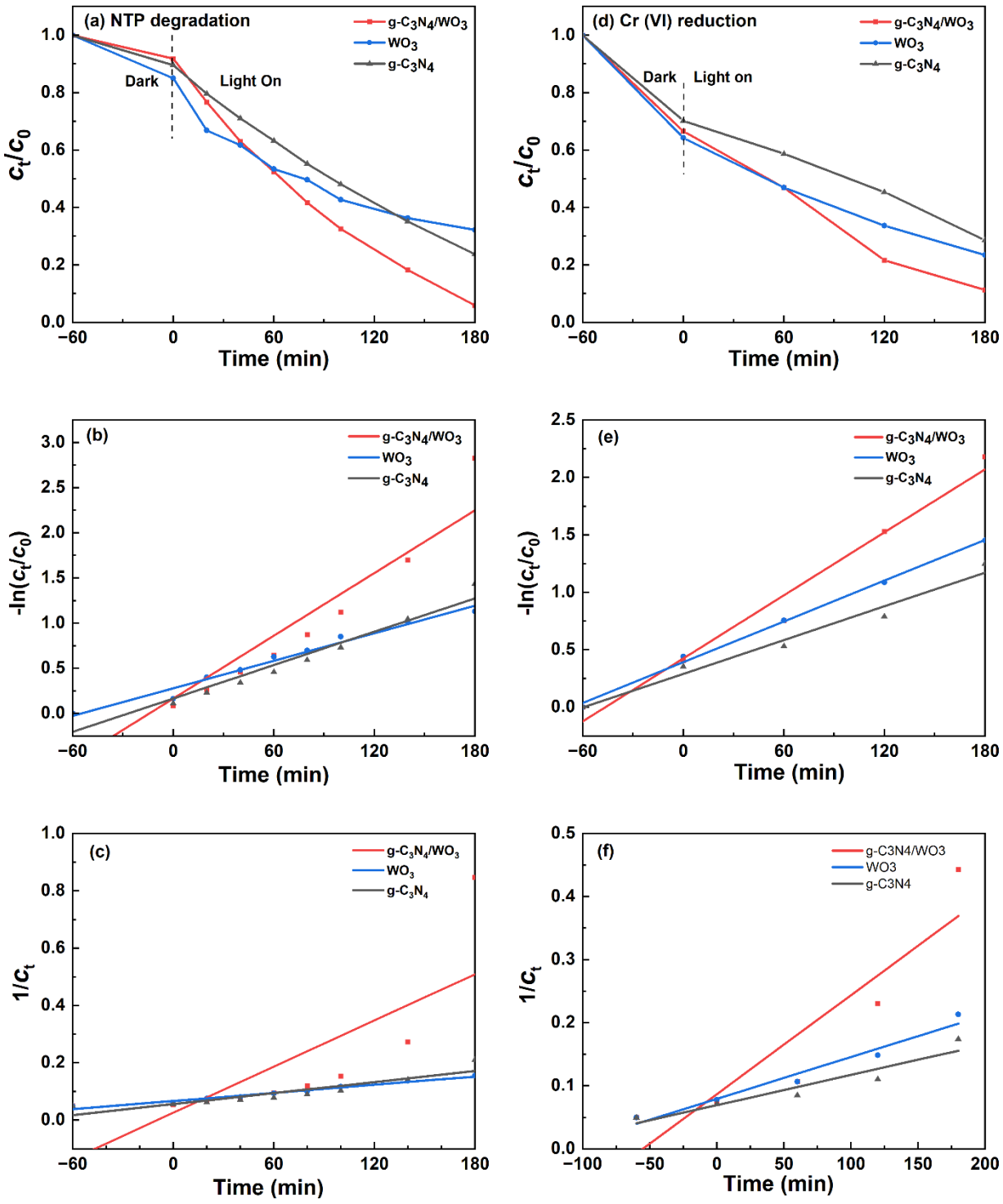

Figure 4.6 NTP degradation (a) and Cr (VI) reduction (d) over g-C_3N_4/WO_3 with the first- and second-order reaction kinetics of NTP degradation (b, c) and Cr (VI) reduction (e, f)

The reaction kinetics for Cr (VI) reduction and NTP degradation has been analyzed using the first- and second-order kinetic equations (Eq. (4–1) & Eq. (4–2)). Table 4.1 summarizes the derived reaction rate constants along with their corresponding R-square values. The findings presented in Figs. 4.6b, c, e, f and Table 4.1 indicate that the first-order rate equation more accurately describes the experimental kinetic data compared to the second-order rate equation.

$$\ln\left(c_t/c_0\right) = -k_1 t \tag{4–1}$$

$$1/c_t - 1/c_0 = k_2 t \tag{4–2}$$

where k_1 is the apparent first-order rate constant, k_2 is the second-order rate constant, and t is the time.

Table 4.1 Reaction rate constants for NTP degradation and Cr (VI) reduction over different photocatalysts under visible light irradiation.

Photocatalysts	**Reactions**	**1st order**		**2nd order**	
		k_1 (min^{-1})	**R^2**	**k_2 (L mg^{-1} min^{-1})**	**R^2**
g-C_3N_4/WO_3	NTP degradation	1.14×10^{-2}	0.876	2.68×10^{-3}	0.592
	Cr (VI) reduction	9.20×10^{-3}	0.976	1.57×10^{-3}	0.844
g-C_3N_4	NTP degradation	6.16×10^{-3}	0.946	6.41×10^{-4}	0.833
	Cr (VI) reduction	4.89×10^{-3}	0.977	4.80×10^{-4}	0.903
WO_3	NTP degradation	5.09×10^{-3}	0.977	4.74×10^{-4}	0.971
	Cr (VI) reduction	5.91×10^{-3}	0.996	6.62×10^{-4}	0.963

Note: the reaction conditions are as follows: the initial concentration of NTP and Cr (VI) are 20.0 mg L^{-1}, catalyst dosage is 1.0 g L^{-1}, T=30 °C, and pH 3.0.

4.3.3.1 Effect of pH on Cr (VI) reduction and NTP degradation

The pH of the solution significantly affects both the decrease of Cr (VI) and the degradation of NTP. To examine the effect of pH on the photocatalytic efficacy of g-C_3N_4/WO_3 heterojunction, simultaneous Cr (VI) reduction and NTP degradation were conducted at varying pH levels (3.0, 5.0, and 9.0), maintaining all other reaction parameters constant.

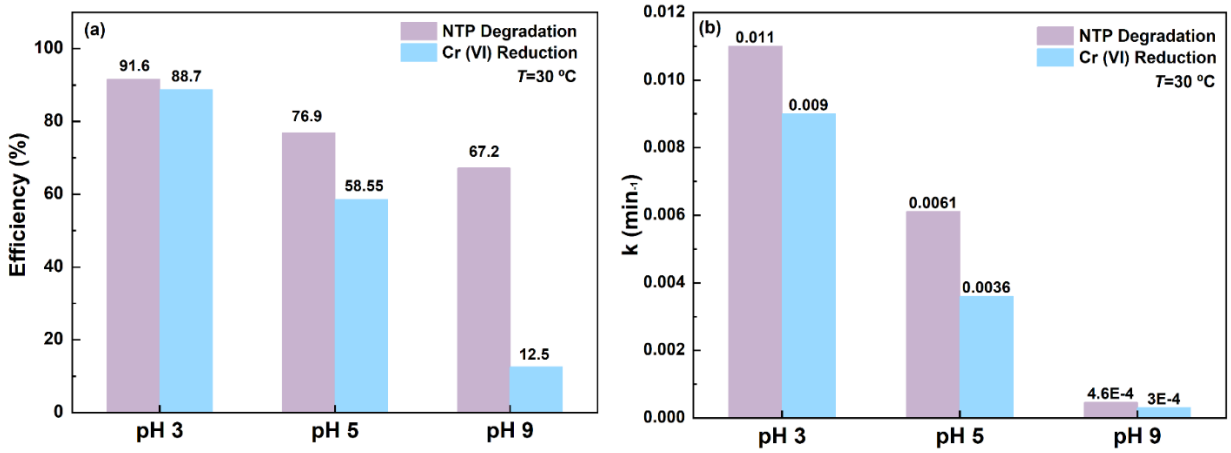

Figure 4.7Effect of pH on NTP degradation and Cr (VI) reduction efficiency (a) and the first-order rate constants (b)

Figure 4.7a illustrates that the g-C_3N_4/WO_3 heterojunction demonstrates superior efficacy for both pollutants under acidic circumstances. As pH increases, the degradation rate of NTP declines from 91.6% at pH 3.0 to 76.9% at pH 5.0 and 67.2% at pH 9.0. Similarly, the reduction efficiency of Cr (VI) reduces from 88.7% at pH 3.0 to 58.6% at pH 5.0 and 12.5% at pH 9.0. Lower pH facilitates the generation of additional protons (H^+) and hydroxide (OH^-), which are crucial for the reduction of Cr (VI) and the production of hydroxyl radicals (•OH) for NTP degradation, respectively. The first-order rate constants for Cr (VI) reduction and NTP degradation across different pH values are illustrated in Fig. 4.7b, and the findings are completely consistent with those shown in Fig. 4.7a.

4.3.3.2 Effect of temperature on Cr (VI) reduction and NTP degradation

The influence of temperature on Cr (VI) reduction and NTP degradation over g-C_3N_4/WO_3 has been experimentally examined at different temperatures (20, 30, and 40°C) at pH 3.0 under visible light irradiation. Figure 4.8a illustrates the efficiencies of Cr (VI) reduction and NTP degradation across various temperature conditions. The findings presented in Fig. 4.8a suggest that the efficiency of NTP degradation is enhanced at elevated temperatures. Nonetheless, the reduction of Cr (VI) exhibited no significant dependence on temperature.

Figure 4.8b illustrates the first-order reaction rate constants for Cr (VI) reduction and NTP degradation. The degradation of organic pollutants is a complex process including oxidative degradation, the production of reactive oxygen species, and adsorption onto catalysts, all of which necessitate activation energy and are impacted by temperature variations. Conversely, the reduction of Cr (VI) is an electrochemical process primarily influenced by the quantity of electrons produced, with lesser dependence on temperature.

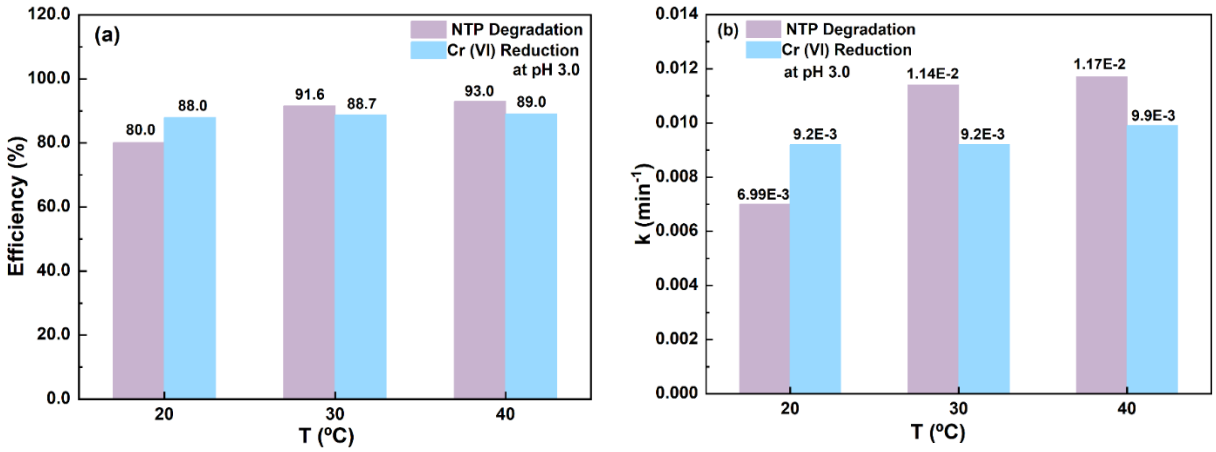

Figure 4.8 Effect of temperature on NTP degradation and Cr (VI) reduction

4.3.3.3 Radical trapping experiment

It is established that free hydroxyl (•OH) and superoxide ($O_2^{\bullet-}$) radicals, along with the photogenerated electrons and holes (e^-/h^+), are involved in the photocatalytic redox reaction. A free radical trapping experiment has been conducted to explore the primary reactive species involved in photocatalytic reactions. In this study, three distinct scavengers were employed: benzoquinone (BQ) served as a scavenger for $O_2^{\bullet-}$, triethanolamine (TEOA) to mitigate the presence of holes (h^+), and isopropanol (IPA) to prevent the formation of •OH. Fig. 4.9 illustrates the effects of these three scavengers on the reduction of Cr (VI) and the degradation of NTP. The NTP degradation experiences a notable reduction in efficiency, decreasing from 91.6% to 84.5%, 59.6%, and 22.7% upon the introduction of IPA, BQ, and TEOA into the reaction system. Surprisingly, the efficiency of Cr (VI) reduction remains largely unaffected by the addition of IPA and BQ, while a significant decrease in Cr (VI) reduction efficiency is observed when holes are consumed by TEOA. The findings presented in Fig. 4.9 indicate that holes are pivotal in the reduction of Cr (VI) as well as in the degradation of NTP.

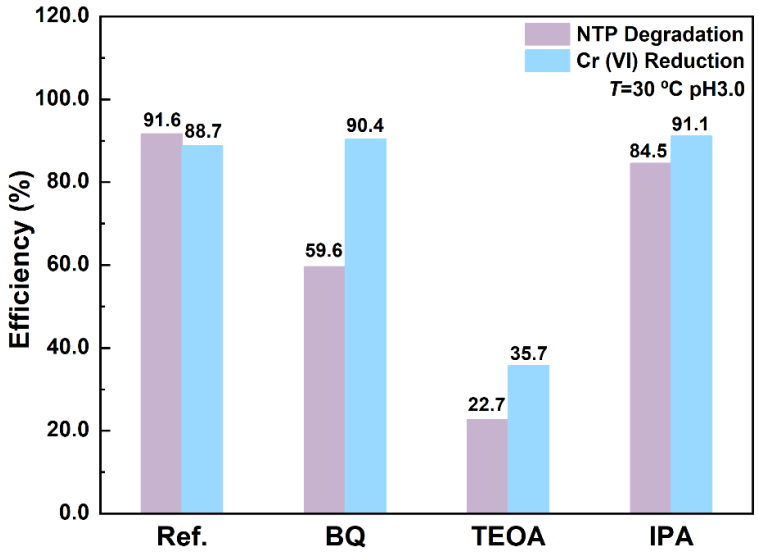

Figure 4.9Free radical trapping experiment

The results of radical trapping experiments indicate that the following reactions are involved in the concurrent photocatalytic reduction of Cr (VI) and degradation of NTP.

$$g-C_3N_4/WO_3 + h\nu \rightarrow e^-_{CB} + h^+_{VB} \quad (4–3)$$

$$2H_2O + 4h^+ \rightarrow 4H^+ + O_2 \quad (4–4)$$

$$OH^- + h^+ \rightarrow {}^{\bullet}OH \quad (4–5)$$

$$O_2 + e^- \rightarrow O_2^{\bullet-} \quad (4–6)$$

$$HCrO_4^- + 3e^- + 7H^+ \rightarrow Cr^{3+} + 4H_2O \quad (4–7)$$

$$Cr_2O_7^{2-} + 6e^- + 14H^+ \rightarrow 2Cr^{3+} + 7H_2O \quad (4–8)$$

$$\left.\begin{matrix} h^+ \\ O_2^{\bullet-} \\ {}^{\bullet}OH \end{matrix}\right\} + NTP \rightarrow \text{oxidization} \quad (4–9)$$

4.3.4 Reaction mechanism for Cr (VI) reduction and NTP degradation

It is widely recognized that the efficiency of photogenerated charge transfer and separation in photocatalysts is the primary determinant of superior photocatalytic performance [26]. Both g-C_3N_4 and WO_3 demonstrate comparable and moderate E_g values, resulting in a high capacity for visible light absorption, an identical light absorption spectrum, and a similar charge carrier generation rate. Upon exposure to visible light, the g-C_3N_4/WO_3 heterojunction simultaneously excites g-C_3N_4 and WO_3, resulting in the production of many charge-carriers (e^-/h^+), which are favorable for redox reactions. Conversely, the distinctive band alignment of g-C_3N_4 and WO_3 facilitates the formation of a Type II heterojunction (Fig. 4.10), enhancing the separation of photogenerated electrons and holes while maintaining robust photo-redox capability. This is the

most important factor that determines the enhanced photocatalytic oxidation activity of g-C_3N_4/WO_3 towards simultaneous photocatalytic Cr (VI) reduction and NTP degradation.

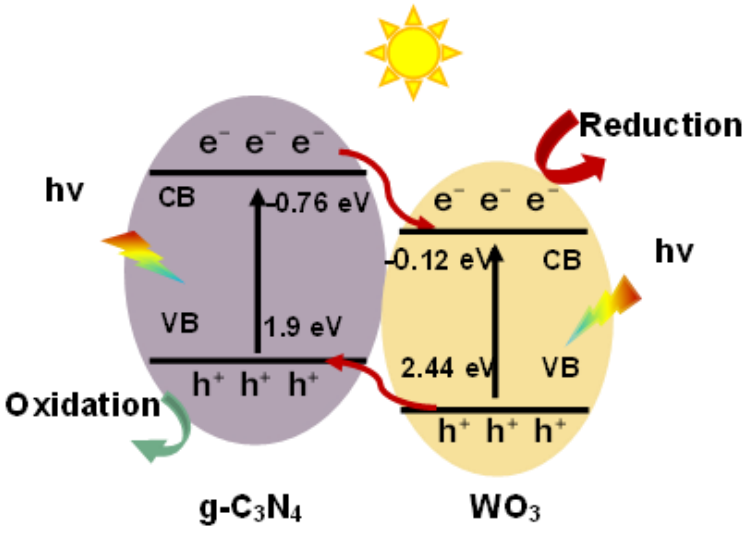

Figure 4.10 Photocatalytic Mechanism of g-C_3N_4/WO_3

4.3.5 Stability and reusability of the g-C_3N_4/WO_3 heterojunction

To evaluate the stability of the synthesized g-C_3N_4/WO_3 heterojunction, XRD and FT-IR measurements were conducted post-photocatalytic reactions, with findings presented in Fig. 4.11 alongside pre-reaction data. The IR spectrum of the photocatalyst exhibits no substantial peak shift after the reaction, indicating the catalyst's excellent chemical stability. Correspondingly, the powder XRD pattern of the -C_3N_4/WO_3 after the photocatalytic reaction exhibits the same characteristic diffraction peaks as the pattern prior to the reaction. Nonetheless, the intensity of the XRD signal of the heterojunction diminishes after reaction, signifying a reduction in the particle size of the photocatalyst. Moreover, the small particle size of the photocatalyst complicates its separation and recovery from the liquid phase, resulting in inadequate reusability of the

synthesized heterojunction. Consequently, it is essential to immobilize the photocatalyst onto a stable solid matrix to create porous particles, thereby enhancing phase separation and reusability.

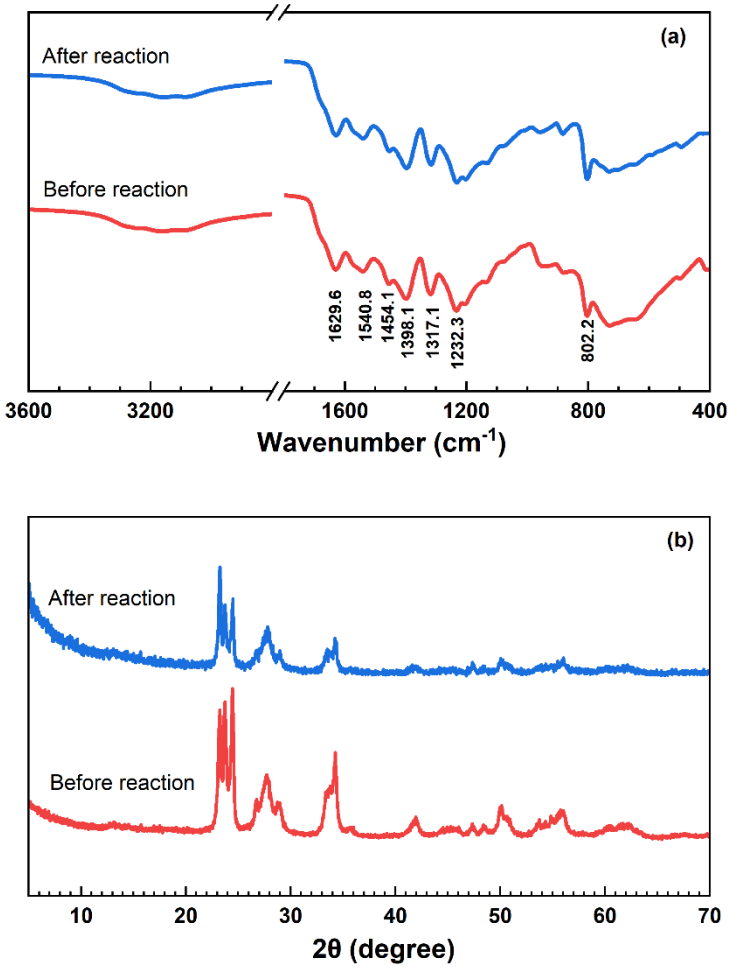

Figure 4.11Comparison of FT-IR spectra (a) and powder XRD patterns (b) of g-C_3N_4/WO_3 before and after photocatalytic reactions

4.4 Conclusion

A facile synthetic method has been employed to fabricate the g-C_3N_4/WO_3 heterojunction for the simultaneous photocatalytic reduction of Cr (VI) and degradation of NTP under visible light irradiation. The findings from XPS, FT-IR, and powder XRD validate the establishment of robust chemically bonded interfaces between g-C_3N_4 and WO_3. The synthesized heterojunction exhibits improved photocatalytic activity, achieving a reduction of 88.7% Cr (VI) and a decomposition of 91.6% of NTP at pH 3.0 and a temperature of 30 °C with the initial concentration of both pollutants being 20.0 mg L^{-1} and a catalyst dosage of 1.0 g L^{-1}. Experimental results demonstrate that low pH enhances both Cr (VI) reduction and NTP degradation, attributed to the production of additional protons (H^+) and hydroxide (OH^-), which are essential for these processes. Furthermore, elevated temperatures enhance the degradation of NTP, while having a negligible impact on the reduction rate of Cr (VI). The radical trapping experiment demonstrates that h^+ is important in both conversions. The band positions of g-C_3N_4 and WO_3, as determined from UV-DRS, indicate the formation of a Type II heterojunction between the two semiconductors. This configuration significantly enhances the separation of photogenerated electrons and holes, thereby improving the reduction efficiency of Cr (VI) and the degradation efficiency of NTP.

References

[1] F. Niu, W. Tu, Y. Zhou, R. Xu, Z. Zou, Killing two birds with one stone: State-of-the-art progress in dual-functional photoredox catalysis for solar fuel conversion and selective organic transformation, EnergyChem 5 (2023) 100112. https://doi.org/10.1016/j.enchem.2023.100112.

[2] Z. Yan, K. Yin, M. Xu, N. Fang, W. Yu, Y. Chu, S. Shu, Photocatalysis for synergistic water remediation and H_2 production: A review, Chem. Eng. J. 472 (2023) 145066. https://doi.org/10.1016/j.cej.2023.145066.

[3] W. Shang, Y. Li, H. Huang, F. Lai, M.B.J. Roeffaers, B. Weng, Synergistic Redox Reaction for Value-Added Organic Transformation via Dual-Functional Photocatalytic Systems, ACS Catal. 11 (2021) 4613–4632. https://doi.org/10.1021/acscatal.0c04815.

[4] S. Kampouri, K.C. Stylianou, Dual-Functional Photocatalysis for Simultaneous Hydrogen Production and Oxidation of Organic Substances, ACS Catal. 9 (2019) 4247–4270. https://doi.org/10.1021/acscatal.9b00332.

[5] A. Akhundi, A. Zaker Moshfegh, A. Habibi-Yangjeh, M. Sillanpää, Simultaneous Dual-Functional Photocatalysis by g-C_3N_4-Based Nanostructures, ACS EST Eng. 2 (2022) 564–585. https://doi.org/10.1021/acsestengg.1c00346.

[6] H. Dou, Y. Qin, F. Pan, D. Long, X. Rao, G.Q. Xu, Y. Zhang, Core–shell g-C_3N_4/Pt/TiO_2 nanowires for simultaneous photocatalytic H $_2$ evolution and RhB degradation under visible light irradiation, Catal. Sci. Technol. 9 (2019) 4898–4908. https://doi.org/10.1039/C9CY01086F.

[7] P. Suyana, P. Ganguly, B.N. Nair, A.P. Mohamed, K.G.K. Warrier, U.S. Hareesh, Co_3O_4–C_3N_4 p–n nano-heterojunctions for the simultaneous degradation of a mixture of pollutants under solar irradiation, Environ. Sci. Nano 4 (2017) 212–221. https://doi.org/10.1039/C6EN00410E.

[8] W. Zhao, T. She, J. Zhang, G. Wang, S. Zhang, W. Wei, G. Yang, L. Zhang, D. Xia, Z. Cheng, H. Huang, D.Y.C. Leung, A novel Z-scheme CeO_2/g-C_3N_4 heterojunction photocatalyst for

degradation of Bisphenol A and hydrogen evolution and insight of the photocatalysis mechanism, J. Mater. Sci. Technol. 85 (2021) 18–29. https://doi.org/10.1016/j.jmst.2020.12.064.

[9] T. Yan, R. Tao, Y. Wang, T. Li, Z. Chu, X. Fan, K. Liu, Highly dispersed g-C_3N_4 on one-dimensional $W_{18}O_{49}$/carbon nanofibers for constructing well-connected S-scheme heterojunctions with synchronous H_2 evolution and pollutant degradation performance, Surf. Interfaces 54 (2024) 105122. https://doi.org/10.1016/j.surfin.2024.105122.

[10] P.K. Prajapati, D. Tripathi, M.K. Poddar, P. Gupta, S.L. Jain, Dual photocatalysis for CO_2 reduction along with the oxidative coupling of benzylamines promoted by Cu/Cu_2O@g-C_3N_4 under visible irradiation, Sustain. Energy Fuels 6 (2022) 2996–3007. https://doi.org/10.1039/D2SE00378C.

[11] L. Zhao, L. Zhang, H. Lin, Q. Nong, M. Cui, Y. Wu, Y. He, Fabrication and characterization of hollow $CdMoO_4$ coupled g-C_3N_4 heterojunction with enhanced photocatalytic activity, J. Hazard. Mater. 299 (2015) 333–342. https://doi.org/10.1016/j.jhazmat.2015.06.036.

[12] J. Gu, H. Chen, F. Jiang, X. Wang, L. Li, All-solid-state Z-scheme Co9S8/graphitic carbon nitride photocatalysts for simultaneous reduction of Cr (VI) and oxidation of 2,4-dichlorophenoxyacetic acid under simulated solar irradiation, Chem. Eng. J. 360 (2019) 1188–1198. https://doi.org/10.1016/j.cej.2018.10.137.

[13] S. Patnaik, K.K. Das, A. Mohanty, K. Parida, Enhanced photo catalytic reduction of Cr (VI) over polymer-sensitized g-C_3N_4/$ZnFe_2O_4$ and its synergism with phenol oxidation under visible light irradiation, Catal. Today 315 (2018) 52–66. https://doi.org/10.1016/j.cattod.2018.04.008.

[14] X.-H. Jiang, Q.-J. Xing, X.-B. Luo, F. Li, J.-P. Zou, S.-S. Liu, X. Li, X.-K. Wang, Simultaneous photoreduction of Uranium(VI) and photooxidation of Arsenic(III) in aqueous solution over g-C_3N_4/TiO_2 heterostructured catalysts under simulated sunlight irradiation, Appl. Catal. B Environ. 228 (2018) 29–38. https://doi.org/10.1016/j.apcatb.2018.01.062.

[15] P. Niu, L. Zhang, G. Liu, H. Cheng, Graphene-Like Carbon Nitride Nanosheets for Improved Photocatalytic Activities, Adv. Funct. Mater. 22 (2012) 4763–4770. https://doi.org/10.1002/adfm.201200922.

[16] Y. Deng, C. Feng, L. Tang, Y. Zhou, Z. Chen, H. Feng, J. Wang, J. Yu, Y. Liu, Ultrathin low dimensional heterostructure composites with superior photocatalytic activity: Insight into the multichannel charge transfer mechanism, Chem. Eng. J. 393 (2020) 124718. https://doi.org/10.1016/j.cej.2020.124718.

[17] Y. Wang, Y. Deng, D. Gong, L. Yang, L. Li, Z. Zhou, S. Xiong, R. Tang, J. Zheng, Visible light excited graphitic carbon nitride for efficient degradation of thiamethoxam: Removal efficiency, factors effect and reaction mechanism study, J. Environ. Chem. Eng. 9 (2021) 105739. https://doi.org/10.1016/j.jece.2021.105739.

[18] X. Wang, Z. Zhu, J. Jiang, R. Li, J. Xiong, Preparation of heterojunction g-C_3N_4/WO_3 photocatalyst for degradation of microplastics in water, Chemosphere 337 (2023) 139206. https://doi.org/10.1016/j.chemosphere.2023.139206.

[19] J. Meng, X. Wang, Y. Liu, M. Ren, X. Zhang, X. Ding, Y. Guo, Y. Yang, Acid-induced molecule self-assembly synthesis of Z-scheme WO_3/g-C_3N_4 heterojunctions for robust photocatalysis against phenolic pollutants, Chem. Eng. J. 403 (2021) 126354. https://doi.org/10.1016/j.cej.2020.126354.

[20] Y.-E. Shin, Y.J. Sa, S. Park, J. Lee, K.-H. Shin, S.H. Joo, H. Ko, An ice-templated, pH-tunable self-assembly route to hierarchically porous graphene nanoscroll networks, Nanoscale 6 (2014) 9734–9741. https://doi.org/10.1039/C4NR01988A.

[21] X.-Y. Sun, F.-J. Zhang, C. Kong, Porous g-C_3N_4/WO_3 photocatalyst prepared by simple calcination for efficient hydrogen generation under visible light, Colloids Surf. Physicochem. Eng. Asp. 594 (2020) 124653. https://doi.org/10.1016/j.colsurfa.2020.124653.

[22] S. Chen, Y. Hu, S. Meng, X. Fu, Study on the separation mechanisms of photogenerated electrons and holes for composite photocatalysts g-C_3N_4-WO_3, Appl. Catal. B Environ. 150–151 (2014) 564–573. https://doi.org/10.1016/j.apcatb.2013.12.053.

[23] H. Yu, F. Hu, H. Xu, B. Song, H. Wang, M. Li, G. Shao, B. Fan, H. Wang, H. Lu, In-situ construction of g-C_3N_4/WO_3 heterojunction composite with significantly enhanced photocatalytic degradation performance, J. Phys. Chem. Solids 187 (2024) 111852. https://doi.org/10.1016/j.jpcs.2023.111852.

[24] M. Sun, Y. Zhou, T. Yu, J. Wang, Synthesis of g-C_3N_4/WO_3-carbon microsphere composites for photocatalytic hydrogen production, Int. J. Hydrog. Energy 47 (2022) 10261–10276. https://doi.org/10.1016/j.ijhydene.2022.01.103.

[25] S.C. Yan, Z.S. Li, Z.G. Zou, Photodegradation Performance of g-C_3N_4 Fabricated by Directly Heating Melamine, Langmuir 25 (2009) 10397–10401. https://doi.org/10.1021/la900923z.

[26] J. Su, G. Li, X. Li, J. Chen, 2D/2D Heterojunctions for Catalysis, Adv. Sci. 6 (2019) 1801702. https://doi.org/10.1002/advs.201801702.

Chapter 5. Conclusion and Recommendations

5.1 Conclusions

In this study, graphitic carbon nitride based photocatalysts were synthesized for the removal of pollutants from the environment. First, g-C_3N_4 was synthesized by calcination of melamine in a muffled furnace; the bulk g-C_3N_4 underwent a second-step calcination process to form g-C_3N_4 nanosheets. The synthesized nanosheets were utilized for the removal of nitenpyram from water. The nanosheets were again utilized to make a heterojunction with WO_3. WO_3 was prepared by a hydrothermal and calcination method. The prepared WO_3 was then dispersed with g-C_3N_4 in distilled water to make a heterojunction. This heterojunction is employed for the dual process to treat nitenpyram and Cr (VI) from the environment simultaneously.

The prepared g-C_3N_4 nanosheets and g-C_3N_4/WO_3 heterojunction were characterized by XRD, FTIR, XPS, UV-DRS and BET. The characterization of g-C_3N_4 nanosheets shows a narrower band gap, and increased surface area as compared to the bulk g-C_3N_4 and a positive valance band position, making it suitable for the degradation of nitenpyram. Also, the characterization of g-C_3N_4/WO_3 indicates the successful synthesis of the type II heterojunction, reduced recombination rate and a well-balanced band structure for simultaneous reduction and oxidation of Cr VI and NTP respectively.

The g-C_3N_4 nanosheets prepared by a two-step calcination process in a muffled furnace at 520℃ with a ramp of 2.5℃ /min for 4 hours were used to degrade NTP from the water. Experimental results show that pH 9 gives us the highest degradation efficiency of 99% after exposure to visible light for 3 hours with an initial concentration of 10 ppm and catalyst dosage of 1.0g/L. The MS

spectrometry shows the reaction mechanism where the NTP is degraded into its metabolites CPMF and CPF.

The prepared heterojunction g-C_3N_4/WO_3 was used to simultaneously degrade NTP and reduce Cr (VI) from water under visible light. The experimental results show that pH 3 gives us the highest efficiency in dual process with 91.6% degradation of NTP and 88.7% reduction of Cr (VI) with an initial concentration of 20 ppm and catalyst dosage of 1.0g/L. The reaction mechanism was also studied for the simultaneous degradation and reduction, which shows that the holes from VB of WO_3 transfer towards VB of g-C_3N_4 nanosheets and electrons from CB of g-C_3N_4 nanosheets transfer towards CB of WO_3, indicating type II heterojunction. The radical trapping experiment was carried out to find the most reactive species in the photocatalytic removal of NTP, which, after experimentation, came out to be h^+.

5.2 Recommendations for future work

In past years, plenty of efforts have been made to make an environmentally friendly and low-cost photocatalyst that can be used to remove pollutants from the environment and other applications. But still, there is room for improvement in the synthesis and utilization of the catalyst.

Some recommendations for future work:

(1) The nanosheets prepared by this method had some impurities, which can be removed by employing purification methods i.e. solvent washing to remove dissolved impurities, acid base treatment and extraction with organic solvents which will remove the impurities and the unreacted precursor without damaging the structure of g-C_3N_4.

(2) The efficiency of the nanosheets can be improved by elemental doping to modify electronic properties or modification in synthesis techniques. Different types of dopants such as sulfur, boron, and phosphorus can be used to enhance g-C_3N_4 photocatalytic ability.

(3) In this study, the g-C_3N_4 was combined with WO_3 to prepare a heterojunction. characterization results of the heterojunction demonstrate that a type II heterojunction was formed. To further increase its photocatalytic ability Z-Scheme heterojunction is preferred for dual process.

(4) The interface between nanosheets and other components is crucial for separating charge, the detailed study of the interfacial interaction and electron transfer dynamics can help us improve the photocatalytic efficiency.

(5) The reuse of the catalyst is still challenging because of its small particle size. The reusability of the catalyst can be enhanced by introducing better separation techniques such as modified magnetic separation, surface functionalization, and electrostatic separation which are favourable for small particles without major loss.

(6) Conduct environmental assessment to check the products of nitenpyram degradation and chromium (VI) reduction are harmless and non-toxic to the environment.

(7) The prepared catalyst performed well in the lab, we should also consider catalyst efficiency in real-world and compare it with other environmental pollutants to extend its application.